Forschungszentrum Karlsruhe
Technik und Umwelt
Wissenschaftliche Berichte
FZKA 6267

The Effect of Vertical Magnetic Field on Liquid Metal Rayleigh-Bénard Convection

U. Burr, L. Barleon, K.-J. Mack, U. Müller

Institut für Angewandte Thermo- und Fluiddynamik
Projekt Kernfusion

Juni 1999

Forschungszentrum Karlsruhe

Technik und Umwelt

Wissenschaftliche Berichte

FZKA 6267

The effect of vertical magnetic field on liquid metal Rayleigh-Bénard convection

U. Burr, L. Barleon, K.-J. Mack, U. Müller

Institut für Angewandte Thermo- und Fluiddynamik
Projekt Kernfusion

Forschungszentrum Karlsruhe GmbH, Karlsruhe
1999

Als Manuskript gedruckt

Forschungszentrum Karlsruhe GmbH
Postfach 3640, 76021 Karlsruhe

Mitglied der Hermann von Helmholtz-Gemeinschaft
Deutscher Forschungszentren (HGF)

ISSN 0947-8620

The effect of vertical magnetic field on liquid metal Rayleigh-Bénard convection

Abstract

Thermal convection of liquid metals is considerably influenced by imposing an external magnetic field. Such magnetoconvective flows control the heat and tritium removal from the breeding material in current fusion blanket designs. A magnetic field may be used to influence the heat transfer controlled solidification in material processing like casting or crystal growth. As the geometries of technical applications are rather complex, a fundamental understanding of the phenomena may only be obtained from simple well defined configurations.

This report presents an experimental study of the influence of a vertical magnetic field on the integral heat transfer and the temporal behavior of liquid metal Rayleigh-Bénard convection. At this specific configuration the horizontal symmetry of the convective flow patterns is not changed by the electromagnetic forces and therefore the magnetic field exerts mainly a damping effect on the convective motions by Joule's dissipation.

The test section is a rectangular box of large aspect ratio 20 : 10 : 1 whereby a parameter range of Rayleigh numbers $0 < Ra < 10^5$ and Chandrasekhar numbers $0 < Q < 14400$ is covered. The Prandtl number of test fluid sodium potassium $Na^{22}K^{78}$ is very small i.e. $\mathrm{Pr} \approx 0.02$ and therefore the nonlinear inertial forces lead to strong time dependent flow.

The integral heat transfer across the layer is characterized by the Nusselt number, calculated from the time averaged temperatures at the upper and the lower boundary. Local, time-dependent temperatures are evaluated from a four-element temperature probe placed in the middle of the liquid metal layer. The non-coplanar arrangement of the thermocouples enables the evaluation of the time-dependent temperature gradient vector which allows to estimate the local isotropy properties of the time dependent flow.

At a constant Rayleigh number and for constant heat flux, the Nusselt numbers are decreasing monotonously with increasing Chandrasekhar numbers. Ranges of enhanced heat transfer caused by the external magnetic field are not observed. Temperature fluctuations are damped significantly by the magnetic field, however, this effect is selective with respect to frequency. Long period fluctuations are stronger damped whereas short period fluctuations are less damped or may even be enhanced. From a practical point of view significant convective heat transport is always coupled with time dependent flow.

From an evaluation of the fluctuating part of the local temperature gradient the horizontal isotropy of the time dependent flow is confirmed; no predominant orientation of convective structures exists. In the vertical direction the isotropy generally decreases with an increasing magnetic field but increases at short time-scales due to the stronger influence of inertial forces in small scale structures.

Der Einfluß eines vertikalen Magnetfeldes auf Flüssigmetall Rayleigh-Bénard Konvektion

Zusammenfassung

Thermische Konvektionsströmungen können durch die Wirkung eines äußeren Magnetfeldes stark beeinflußt werden. Solch magnetokonvektive Strömungen bestimmen die Wärme- und Tritiumabfuhr aus dem Brutmaterial derzeitig betrachteter Fusionsblankets. Die gezielte Beeinflussung des Wärmetransportes und der Strömungsstruktur kann darüberhinaus zur Verbesserung von Materialprozessen wie dem Formguß oder dem Ziehen von Einkristallen eingesetzt werden. Da die Geometrien technischer Anordnungen meist sehr komplex sind, werden die wesentlichen Phänomene in einfachen Geometrien gezielt untersucht.

In diesem Bericht wird ein Experiment vorgestellt, bei dem der Einfluß eines vertikalen Magnetfeldes auf den integralen Wärmedurchgang sowie das zeitliche Verhalten einer Flüssigmetall Rayleigh-Bénard Konvektionsströmung experimentell untersucht wird. Bei dieser Anordnung wird die horizontale Symmetrie der Strömung durch die elektromagnetischen Kräfte nicht verändert und das magnetische Feld bewirkt daher im Wesentlichen eine zusätzliche Dämpfung der Konvektionsbewegungen durch Joulsche Dissipation.

Die Teststrecke ist ein rechtwinkliger Behälter mit großem Seitenverhältnis $20 : 10 : 1$, in dem ein Parameterbereich der Rayleigh-Zahlen $0 < Ra < 10^5$ und der Chandrasekhar-Zahlen $0 < Q < 14400$ untersucht wurde. Die Prandtl-Zahl der als Experimentierflüssigkeit eingesetzten Natrium-Kalium Legierung $Na^{22}K^{78}$ beträgt lediglich $\mathrm{Pr} \approx 0.02$, so daß sich aus den nichtlinearen Trägheitskräften ein stark zeitabhängiger Strömungszustand ergibt.

Der integrale Wärmetransport durch die Flüssigmetallschicht wird anhand der Nusselt-Zahl charakterisiert, die aus den zeitlich gemittelten Temperaturen an der oberen und der unteren Berandung bestimmt wird. Lokale Temperaturschwankungen werden von einer Vier-Element-Temperatursonde, die in Schichtmitte angeordnet ist, erfaßt. Die antiparalelle Anordnung der Thermoelemente ermöglicht die Bestimmung des lokalen, zeitabhängigen Temperaturgradientenvektors. Aus diesem können die lokalen Isotropieeigenschaften der zeitabhängigen Strömung abgeleitet werden.

Bei konstant gehaltener Rayleigh-Zahl sowie bei konstantem Wärmestrom sinken die Nusselt-Zahlen monoton mit der Chandrasekhar Zahl. Bereiche mit erhöhtem Wärmeübergang werden nicht beobachtet. Temperaturfluktuationen werden durch das magnetische Feld ebenfalls stark gedämpft, wobei dieser Vorgang frequenzabhängig ist. Fluktuationen mit großen Zeitskalen werden stärker gedämpft, solche mit kürzeren Zeitskalen dagegen schwächer, gegebenenfalls sogar verstärkt. Signifikanter konvektiver Wärmetransport ist praktisch immer mit einem zeitabhängigen Strömungszustand verbunden.

Anhand der Fluktuationen des Temperaturgradientenvektors, mit dessen Hilfe die horizontale Isotropie der zeitabhängigen Strömungsmuster gezeigt werden kann, wurde keine Vorzugsrichtung der Konvektionsstrukturen festgestellt. In der vertikalen Richtung nimmt die Isotropie mit der Stärke des Magnetfeldes ab und steigt im Bereich kleinerer Zeitskalen an, worin sich die größere Bedeutung der Trägheitskräfte im Bereich kleinerer Skalen zeigt.

Contents

1 Introduction

When a liquid is exposed to a temperature gradient, the thermal expansion causes gradients in the density and from the acceleration of gravity a convective motion determined by buoyant, viscous and inertial forces may set in.

Thermal convection of liquid metals is an important phenomenon that occurs in a wide range of technical applications. In current fusion blanket designs lithium-lead alloy is used mainly as a breeding material whereas the heat deposited in the liquid metal is removed by water cooled tubes inside the liquid (Giancarli, Severy, Baraer, Leroy, Mercier, Proust and Quintric-Bossy (1992)). The externally forced flow required for a continuous circulation and for trithium extraction is very weak and buoyant flow may therefore become dominant.

As the flow of the electrically conducting fluid within the blanket is exposed to the strong magnetic field holding the fusion-plasma, electric currents are induced. The interaction of these currents with the applied magnetic field introduces Lorenz forces to the momentum balance of the flow and a magnetohydrodynamic (MHD) convective flow is established. From the generally damping effect of electromagnetic forces on fluid motion by Joules dissipation the heat transfer from the liquid metal to the cooling tubes is expected to be significantly reduced. Without any knowledge about the magnitude of damping, the thermohydraulic design may be carried out with the conservative approach of stagnant fluid with pure heat conduction. But for the removal of tritium respectively to avoid tritium hot spots at least some marginal velocity is necessary. Thus a clear understanding of the influence of the magnetic field on the convective motion is essential for the technical feasibility of such a blanket design.

An other field of technical applications, where liquid metal convective phenomena are important, is the processing of metallic workpieces like casting or the pulling of large single crystals from a melt. In casting the solidification requires the removal of heat from the melt and a temperature gradient has therefore to be maintained between the cold mould and the melt giving rise to strong convective motion. The same situation holds when large single crystals are pulled from a melt by the Czochralsky-process or zone-melting techniques. There a temperature gradient has to be maintained even for practically infinite time.

As for the design of heat transfer units the suppression of convective motion by magnetic fields is an undesirable effect, for material processing it offers a powerful possibility to control various phenomena like the grain size or segregation during the solidification process. On one hand the convective motion causes an intense mixing of the melt ensuring homogeneous conditions at the liquid-solid interface. On the other hand if the temperature gradient is large, non-linear inertial forces may become dominant and unstable flow phenomena will lead to non-homogeneous physical properties in the solid. Only from the controlled suppression of either all or only unstable convective motions we can take benefit of magnetic fields to improve material processes.

The physical nature of electromagnetic damping is significantly different from viscous dissipation or the effect of flow through a porous body because the Lorentz force has a strong non-isotropic character. In principle any natural convective flow in a cavity may be interpreted as a recirculating vortex like motion between heat source and heat sink. Therefore the effect of magnetic field on convective structures is quite similar to the non-isotropic damping of vortices in MHD turbulence (see Burr (1998) and literature

cited therein). If the magnetic field is applied perpendicular to the plane of motion, the damping effect is only weak whereas if the streamlines have to cross magnetic field lines the damping effect is some orders of magnitudes stronger. Furthermore, if the walls of the cavity are electrically conducting the flow is additionally influenced by the current paths within the wall which may lead to a higher current density and therefore to stronger damping of the fluid motion. But all these arguments are too general and the present state of investigation is far away from predicting the convective motion in the complex geometry of a fusion blanket or in a mould of arbitrary geometry. Therefore investigations of simple, well defined problems are necessary to separate different flow effects and to confirm theoretical and numerical predictions of the phenomena in magnetoconvective flows.

1.1 Phenomenology of Rayleigh-Bénard convection

This report presents an experimental study of Rayleigh-Bénard convection with an imposed vertical magnetic field. In figure 1 the investigated flow problem is sketched.

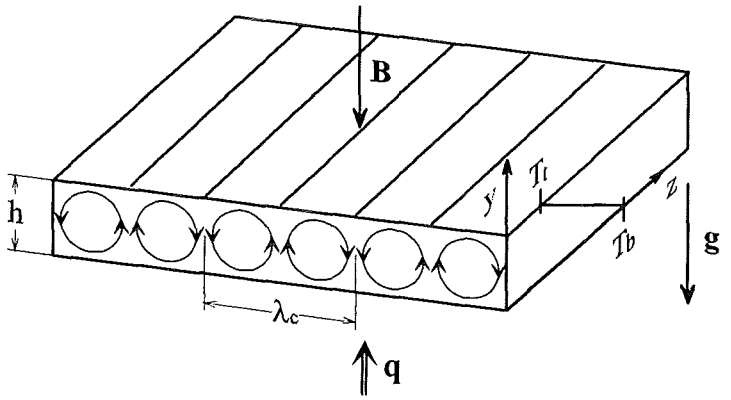

Figure 1: Geometry of Rayleigh-Bénard convection with imposed vertical magnetic field.

An electrically well conducting fluid (liquid metal) is confined between two infinite horizontal walls of distance h. By heating the lower boundary and by cooling the upper wall a temperature gradient is maintained parallel to the acceleration of gravity $\mathbf{g}$. Due to the thermal expansion, the fluid at the bottom is lighter whereas the fluid at the upper wall is heavier. If the temperature gradient and therefore the differences in density exceeds a certain critical value, a convective motion in the form of stationary convective rolls of a distinct critical spacial wave length λ_c sets in. This onset of convection for pure hydrodynamic flow is determined by a single non-dimensional parameter, the Rayleigh number

$$Ra = \frac{\beta g \Delta T h^3}{\nu \kappa}, \tag{1}$$

denoting the ratio of buoyant- to viscous forces. Where $\beta = 1/\rho \cdot d\rho/dT$ is the volumetric thermal expansion coefficient defined as the relative change of the density ρ with temper-

ature T, g the magnitude of the acceleration of gravity, $\Delta T = T_b - T_t$ the temperature difference between the lower and the upper fluid-wall interface, ν the kinematic viscosity and $\kappa = \lambda/\rho c_p$ the thermal diffusivity calculated from the thermal conductivity λ and the specific heat c_p.

The critical Rayleigh number for the onset of convection Ra_c is obtained by a linear stability analysis. If the non-slip condition $\mathbf{v} = \mathbf{0}$ is satisfied at the upper and the lower wall and both bounding surfaces are isothermal the calculations of Pellew and Southwell (1940), and Reid and Harris (1958) have yielded

$$Ra_c = 1707.76 \quad at \quad a_c = 3.117, \tag{2}$$

where a_c is the horizontal wave number at the minimum point of marginal stability curve. The wave length is calculated as $\lambda_c = 2\pi/a_c$ as $\lambda_c \approx 2$, indicating that instability sets in as convective rolls with the same horizontal length scale as the height h of the layer.

If the Rayleigh number is further increased, the flow undergoes a transition from steady three-dimensional flow patterns to time dependent three-dimensional and finally turbulent flow. The limits of these different flow regimes do not only depend on the Rayleigh number. As inertial forces become more important in the momentum balance with higher driving force, the Prandtl number

$$\mathrm{Pr} = \frac{\nu}{\kappa} \tag{3}$$

occurs as an additional relevant parameter that further controls the coupling between the velocity and the temperature field. By definition the Prandtl number is independent of the flow and describes the characteristic physical properties of the investigated fluid. In figure 2, taken from Krishnamurti (1973), the distinct flow regimes of Rayleigh-Bénard convection are mapped as a function of Rayleigh and Prandtl number. At high Prandtl

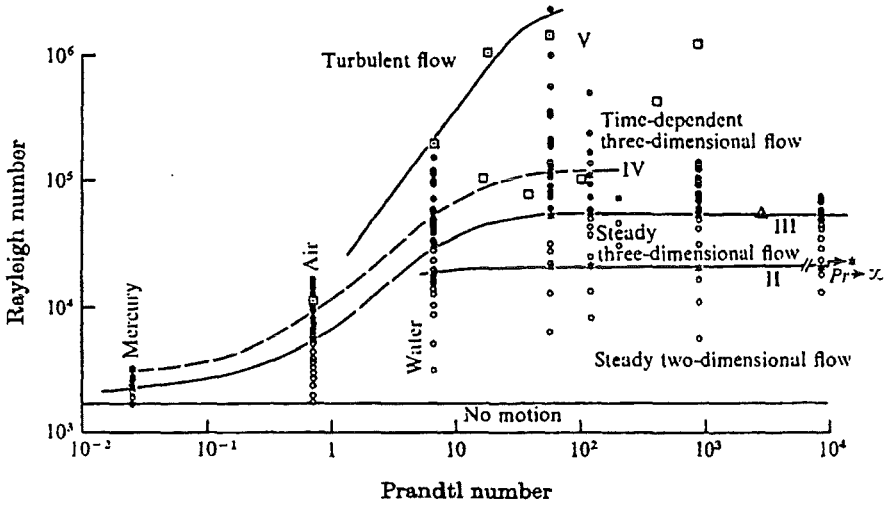

Figure 2: Mapping of Rayleigh-Bénard flow regions as a function of Rayleigh- and Prandtl number (Krishnamurti (1973)).

numbers being typical for oils, the different flow phenomena are observed in a broad

range of the Rayleigh numbers. As the Prandtl number is decreased the range of the flow regimes contracts and in the limit case of very small Prandtl numbers, typical for liquid metals, the transition from laminar to turbulent convection takes place for a very small increase of the Rayleigh number.

The structure of the convective motion at supercritical Rayleigh-numbers has been adressed extensively in the literature (see Clever and Busse (1974), Busse (1978), and Chu and Goldstein (1973)). The regions of steady and time dependent three-dimensional flow are characterized by well organized flow patterns such as Eckhaus-, zig-zag-, cross-roll- or knot- instabilities.

At turbulent convection thermal boundary layers are formed at the upper and the lower boundary. Out of these layers small-scale turbulent vortices are released resulting in large convective heat transport from the bottom to the top. Within the boundary layers heat is transported mainly by heat conduction.

If a permanent temperature difference between the upper and lower boundaries is maintained, a heat flux of magnitude q passes the layer (see figure 1). The effectivity of the convective heat transport is characterized by the non dimensional Nusselt number

$$Nu = \frac{q}{q_0} \tag{4}$$

defined by the ratio of the total heat flux q to the one of pure heat conduction at the same temperature difference. From Fouriers law q_0 is calculated as

$$q_0 = -\lambda \frac{\Delta T}{h}. \tag{5}$$

At subcritical conditions the Nusselt number becomes unity whereas the occurrence of convective heat transport at supercritical conditions is indicated by Nusselt numbers larger than one. In general the Nusselt number depends on both the Rayleigh and the Prandtl number. In figure 3 taken from Kek (1989) the Nusselt numbers obtained in several relevant experiments, performed in liquids of various Prandtl numbers, are plotted as a function of the Rayleigh number. Indicated by the Nusselt numbers, the convective heat transport at constant Rayleigh number is smaller at smaller Prandtl numbers. In addition different characteristics of the increase of the Nusselt number with Rayleigh numbers are observed.

1.2 The effect of a vertical uniform magnetic field

If a magnetic field $\mathbf{B} = (b_x, b_y, b_z)$ is applied on the motion of an electrically conducting fluid, an electric field $\mathbf{E} = \mathbf{v} \times \mathbf{B}$ is induced by the motion of the fluid with the velocity $\mathbf{v} = (u, v, w)$. Electric currents are driven along the gradient of the electric field forming current loops that either close within the fluid or in conducting walls. There are two effects arising with the presence of a current density $\mathbf{j} = (j_x, j_y, j_z)$ in the fluid.

I. According to the direction and the strength of the electric currents as well as the magnetic permeability μ of the fluid, a magnetic field $\nabla \times \mathbf{B} = \mu \cdot \mathbf{j}$ is induced, which is superimposed on the applied one.

II. From the interaction with the magnetic field, the current density causes Lorenz forces $\mathbf{F}_L = \mathbf{j} \times \mathbf{B}$ which act perpendicular to the current density and the magnetic field.

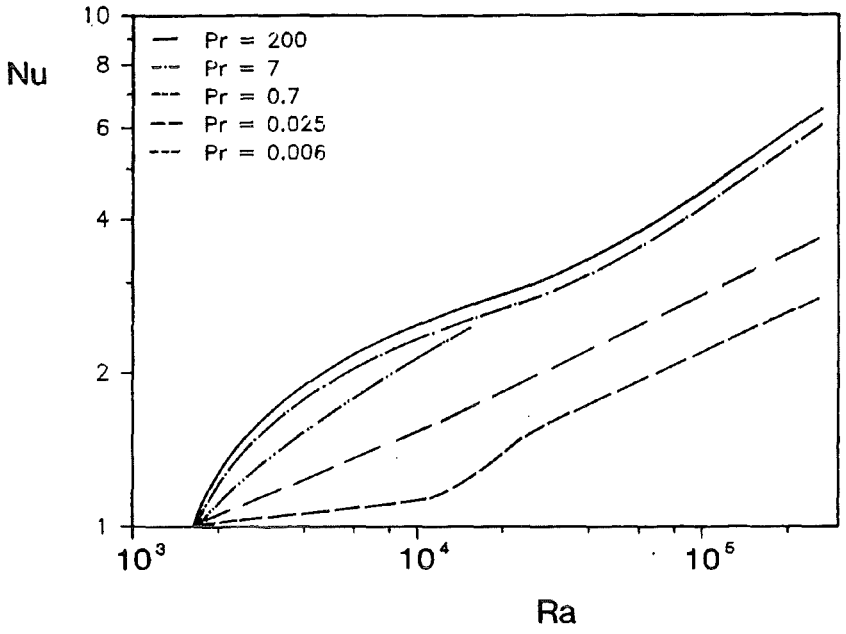

Figure 3: Nusselt numbers as a function of Rayleigh number for liquids of different Prandtl numbers. Kek (1989) compared the results of Rossby (1969) for Pr = 0.025, Pr = 7.0 and Pr = 200, and Threlfall (1975) for Pr = 0.7 with his own at Pr = 0.006.

The application of these principles to a convective roll in Rayleigh-Bénard convection in the case of a vertical magnetic field is sketched in figure 4. Electric currents induced by

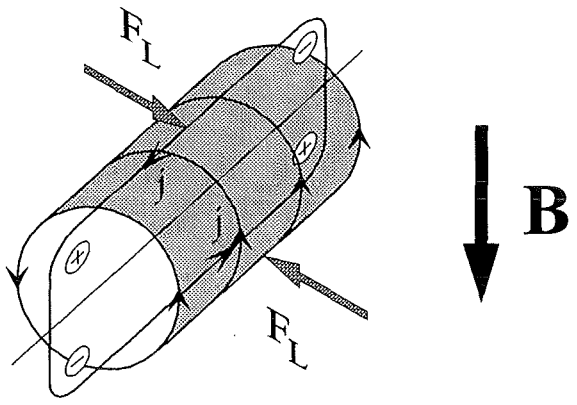

Figure 4: Magnetic damping of a convective roll in Rayleigh-Bénard convection from the impact of a vertical magnetic field.

the horizontal motion immediately close within the convective roll itself and a high current density may occur. The induced Lorenz forces are opposing the horizontal motions of the fluid and therefore are causing strong electromagnetic damping. As horizontal motion can not be avoided in recirculating convective flows, the Lorenz force acts stabilizing on the

fluid and the onset of convection is shifted to higher temperature gradients and occurs at higher Rayleigh number respectively.

The electromagnetic effects are governed by two additional dimensionless parameters. The Chandrasekhar number

$$Q = \frac{B_0 h^2 \sigma}{\rho \nu} \tag{6}$$

denotes the ratio of electromagnetic to viscous forces. B_0 is the magnitude of the applied magnetic field, respectively the magnetic induction, and σ the electrical conductivity. The magnetic Prandtl number

$$Pm = \nu \mu \sigma \tag{7}$$

represents the ratio of viscous momentum transport to diffusive transport of the magnetic field.

Chandrasekhar (1961) performed a linear stability analysis for an infinite layer assuming isothermal boundaries. His results for the onset of convection as a stationary motion, summarized in figure 5, show a tremendous increase of both the critical Rayleigh number and the wave number with the Chandrasekhar number. The decrease in the horizontal

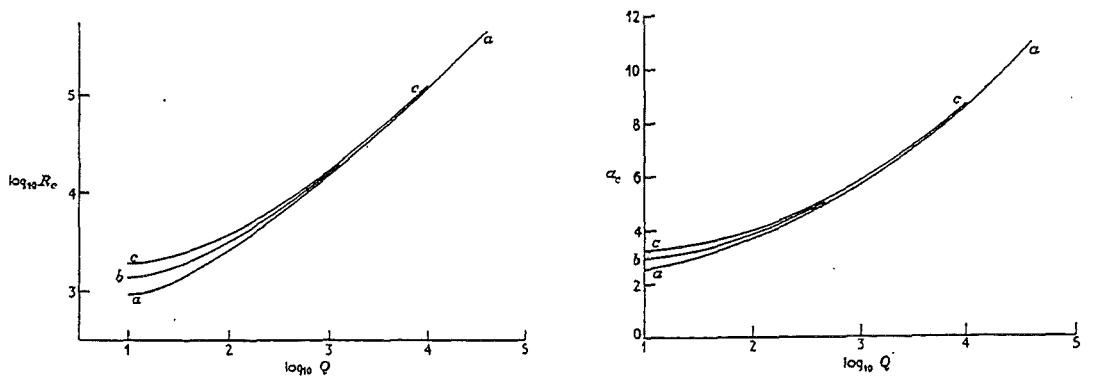

Figure 5: The variation of a) the critical Rayleigh number Ra and b) the critical wave number a_c for the onset of instability as stationary motion as a function of the Chandrasekhar number Q for the three cases (i) both bounding surfaces free (curve labeled aa), (ii) one bounding surfaces free and the other rigid (curve labeled b), and (iii) both bounding surfaces rigid (curve labeled c).

length-scale of the rolls is explained by the lack of Joule's dissipation at vertical motion. The system trys to minimize Joule's dissipation by reducing horizontal motions up to the point where viscous dissipation opposes the benefit.

At high Chandrasekhar numbers viscous forces become less important and the onset of instability is governed by the balance of buoyant and electromagnetic forces only. Neglecting viscous forces the layer gets unstable at

$$Ra_c = \pi^2 Q \tag{8}$$

with a horizontal wave number of

$$a_c = \left(\frac{\pi^4}{2} Q\right)^{\frac{1}{6}}. \tag{9}$$

Because of the coupling between the velocity field and the induced magnetic field the instability may also set in as an oscillating motion. The calculations of Chandrasekhar (1961) yield that this phenomena, called overstability, cannot occur if $Pm < \mathrm{Pr}$. This limit holds for almost every terrestrial condition (liquid metals at moderate temperatures) and we can expect convection always to set in as stationary motion. These analytical predictions for the increase of the critical Rayleigh number as well as the wave number have been experimentally confirmed by Nakagawa (1955), Nakagawa (1956) and Nakagawa (1959).

The effect of a vertical magnetic field on the flow patterns at moderate supercritical Rayleigh numbers was investigated theoretically by Busse and Clever (1982) and Busse and Clever (1996). In general the stability limits of distinct flow regimes are shifted to higher Rayleigh numbers as the Chandrasekhar number is increased. Time dependent convection is stronger influenced by the magnetic field than stationary patterns.

The problem of Rayleigh-Bénard convection with an imposed vertical magnetic field was chosen for a basic study of magnetoconvective flow because it provides a well defined situation even for an experimental setup.

- At a large enough aspect ratio the only characteristic length in the cavity is the height of the layer and the flow in the mayor part of the facility is not influenced by the side walls.
- Convection sets in above a critical value of the driving temperature difference and may therefore be clearly distinguished from pure heat conduction.
- As all electric currents close on the convective flow structures themselves (see figure 4), the problem is not influenced by the electrical conductivity of the vertical walls. The problem of side layers has therefore not to be discussed.
- The vertical magnetic field does not break the horizontal symmetry of the flow i.e. the situation described in figure 4 holds for any orientation of the convective roll in the horizontal plane. No formation of vortex structures alined with the magnetic field is therefore expected.

Although the problem is already discussed in a wide range of literature, there is a lack of experimental data for the heat transfer rates and the flow pattern especially in the range of high Rayleigh- and Chandrasekhar numbers, as they are relevant for technical applications.

2 Experimental setup

2.1 The test facility

The investigation of liquid metal convective flow demands a high standard of the experimental facility because the high thermal conductivity of liquid metals requires a high heat flux to achieve high Rayleigh numbers. In this experiment eutectic sodium-potassium alloy $Na^{22}K^{78}$ was chosen as a test fluid. The temperature dependent thermophysical properties of this liquid metal which is liquid above $T = -11°C$ are calculated from the

	$Na^{22}K^{78}$	H_2O	
ρ	842.4	998	$[kg/m^3]$
β	0.31	$0.18_{15°C}$	$[10^{-3}]$
ν	$0.5766 \cdot 10^{-6}$	$1.00 \cdot 10^{-6}$	$[m^2/s]$
λ	23.56	0.598	$[W/mK]$
c_p	936.84	4179	$[J/kgK]$
σ	$2.4735 \cdot 10^6$	10^{-9}	$[1/\Omega m]$
κ	$2.5853 \cdot 10^{-5}$	$1.4338 \cdot 10^{-7}$	$[m^2/s]$
Pr	0.019	6.97	$[-]$

Table 1: Thermophysical data of eutectic sodium-potassium alloy $Na^{22}K^{78}$ at $120°C$ compared with the ones of water (H_2O) at $20°C$.

polynomes in appendix A.1. In table 1 the thermophysical properties of NaK at $120°C$ are compared with the ones of water (H_2O) at $20°C$ taken from Gieck (1981).

The most significant difference is found in the values of the thermal conductivity λ. Together with the smaller heat c_p this leads to a much higher thermal conductivity κ and finally to a Prandtl-number which is orders of magnitude lower than the one of water.

In order to achieve constant temperatures at the upper and lower boundary, the thermal conductivity of the wall material has to be as high as possible to equalize immediately any temperature disturbance imposed from the convective flow to the wall. But even the high thermal conductivity of copper ($\lambda_{Cu} = 384W/mK$), commonly used for this purpose, is not high enough to equalize temperature differences in the wall over longer horizontal distances. Therefor the heat fluxes at the lower and the upper walls have to be imposed respectively removed as homogeneous as possible. The design of a liquid metal heat transfer test facility has to account especially to this point and so we will outline some special features of the test section, that are not required in case of ordinary high Prandtl number fluids.

In figure 6a cross section of the test facility is shown. A longitudinal cross section and a view from the top can be obtained from figure 7. The dimensions of the liquid metal layer are: height $20mm$, width $200mm$ and length $400mm$ giving an aspect ratio of $1 : 10 : 20$. The lower and the upper walls are made of copper plates of $20mm$ thickness, the side walls of $1.5mm$ stainless steel sheet metal.

The heat flux is supplied to the lower wall by 40 electrically powered heating rods which are soldered with silver brass into their individual groves to assure good thermal contact. At a maximum heating power of $P = 10.8kW$ a uniform heat flux of $q = 1.35 \cdot 10^5 W/m^2$ can be obtained.

The heat is removed from the upper wall by a boiling pool of water. The steam is condensed on 12 longitudinal copper tubes which are cooled by water from an external loop. In order to get a well defined boiling process with constant superheating of the wall, the pool is filled with glass spheres of $5mm$ diameter. The uniform temperature of the boiling liquid is able to equalize immediately any horizontal temperature variations imposed for example from the condenser and thus a homogeneous temperature distribution at the upper copper plate is obtained.

At small heat flux the heat losses at the pool side walls are inhibiting homogeneous boiling and the temperature distribution at the upper copper plate might become inho-

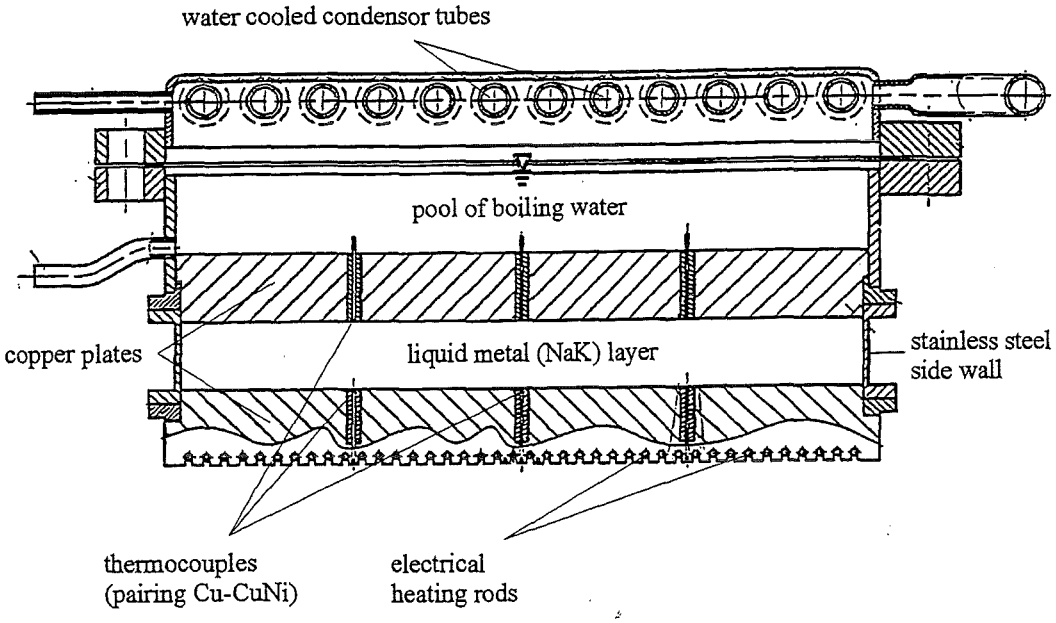

Figure 6: Crossection of the test facility. The liquid metal layer (NaK) is confined between two horizontal copper plates.

mogeneous. To overcome this effect, the steam area above the water line was fitted with an additional electrical heating rod to balance heat losses. It turned out that with a moderate overheating of the boiling pool homogeneous temperatures at the upper walls are obtained.

The experiments are performed in the MEKKA facility of the Institute of Applied Thermo and Fluid Dynamics (IATF) of the Research Center Karlsruhe (FZK). A detailed description of the facility may be taken from Barleon, Mack and Stieglitz (1996), here we focus on major details concerning the experiment. The magnetic field is produced by a normal conducting magnet which provides a homogeneous vertical magnetic field area of $800 \times 483mm$ within a magnetic gap of $168mm$ height. The strength of the magnetic field may be varied from 0 up to 2 $Tesla$. In figure 8 the test section is placed in front of the magnetic gap. In order to perform the experiments the test section is moved on rails into the center of the magnetic gap.

With this experimental setup the range of parameters $0 < Ra < 10^5$ and $0 < Q < 6 \cdot 10^6$ can be covered. As the Rayleigh and the Chandrasekhar number are controlled by the physical parameters temperature difference ΔT and applied magnetic field B_0 they may be arbitrary chosen for a parameter study. But an other situation holds for the Prandtl number which as a physical property depends only on the temperature of the fluid. The boiling water pool at the upper plate fixes the temperature there to the boiling temperature of water ($T \approx 100°C$). Higher temperature differences are achieved only by increasing the temperature of the lower plate and, therefore, the mean temperature of the liquid and with it the Prandtl number can not be held constant when increasing the Rayleigh number. In figure 9 the Prandtl number is plotted as a function of temperature.

In the temperature range $100°C < T < 200°C$ where the experiments are to be performed the Prandtl number decreases in the range $0.021 < \mathrm{Pr} < 0.013$. Thus at

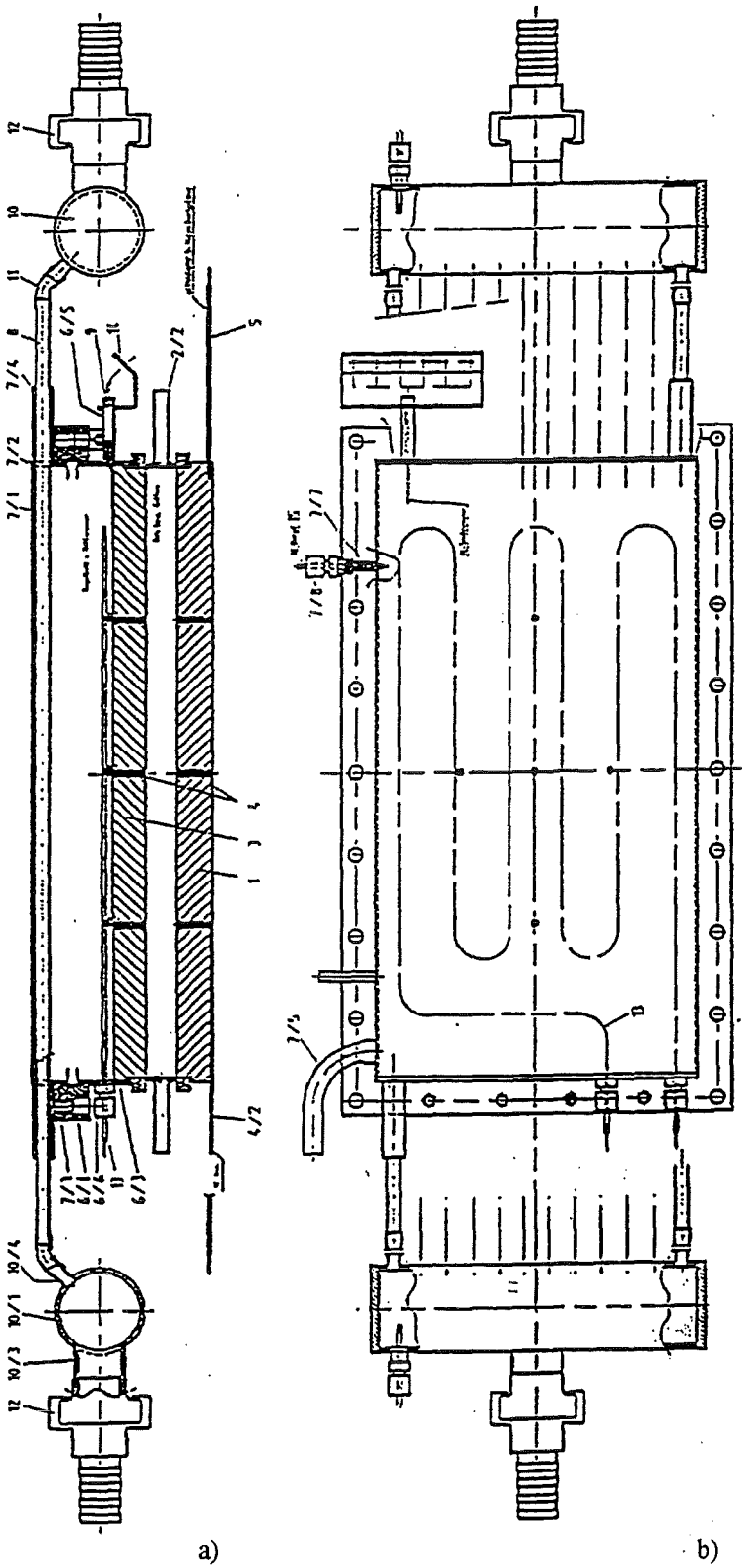

Figure 7: a) longitudinal cross section and b) top view of the test section.

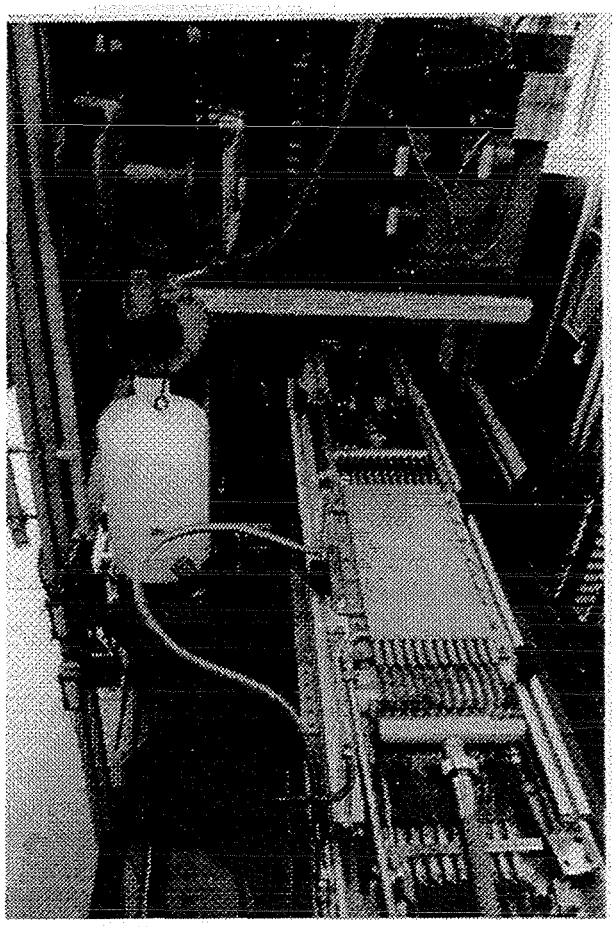

Figure 8: Test section placed in front of the magnetic gap of the normal conducting electromagnet producing a vertical magnetic field. In order to perform the experimements, the test section is moved on rails into the center of the magnetic gap.

higher Rayleigh numbers smaller Prandtl numbers are obtained, and in order enable a comparison with theoretical predictions we will refer in the results also to the value of the Prandtl number.

2.2 Instrumentation

In the experiments the Rayleigh number is controlled by the magnitude of the applied heat flux. The temperatures at the lower and the upper boundary being subject to it are measured by five $Cu - CuNi$ thermocouples in each copper plate. In figure 10 the horizontal positions of the thermocouples are shown. They are counted as an array $T_{i,j}$, where the first index i denotes the horizontal position (i.e. M for the central one and the four winds N, S, E and W) and the second index j is indicating the lower respectively the upper wall by b and t. In order to achieve a perfect thermal contact of the thermocouples to their measuring position, a special fitting technique was developed where the thermocouples are first soldered into copper cylinders which are later pressed leak-tide into the copper plates (see figure 11). The measuring points of the thermocouples are located at a distance of only $e = 1mm$ from the fluid wall interface. An interpolation

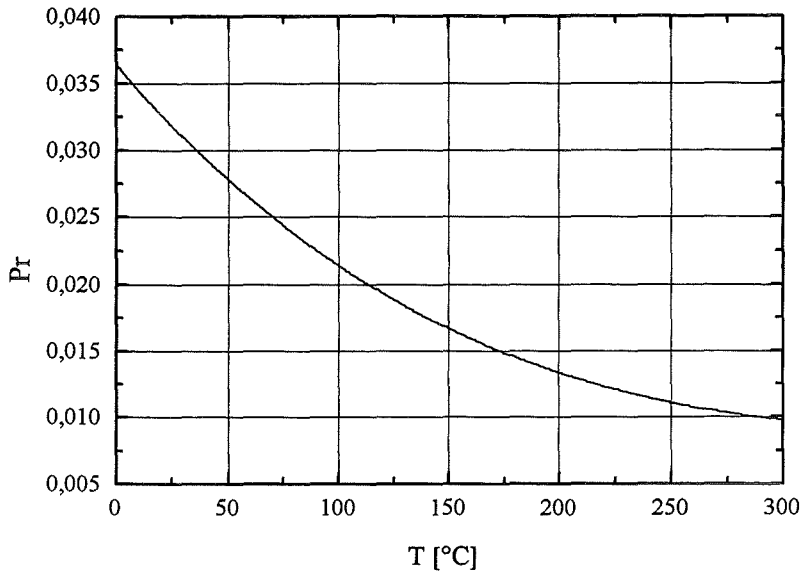

Figure 9: Prandt number of eutectic sodium-potassium alloy $Na^{22}K^{78}$ as a function of temperature.

of the temperature at the fluid wall interface is performed by using Fourier's law (eq. 5) and the thermal conductivity of copper.

In order to investigate local time dependent flow quantities a four-element temperature probe was placed in the fluid, right in the middle between the positions of the thermocouples $T_{S,b}$ and $T_{S,t}$ (see figure 10). In figure 12a the sensing tip of the probe is compared with a match. The probe shaft is made of an isolating ceramic tube with a diameter of $2mm$. Four $Ni - CrNi$ thermocouples of $0.25mm$ diameter are sticking out of the tube into the fluid and are forming the sensing tip. The precise arrangement of the thermocouples and the distances between them are shown in figure 12b. The non-coplanar arrangement of the thermocouples allows to approximate the time dependent temperature gradient ∇T in the fluid by finite differences (see appendix B). As the temperature gradient is a vector it contains information on the spacial structure of the flow and therefore, we can obtain additional information on the spacial structure of the convective flow even from a single point measurement.

2.3 Data acquisition and evaluation

In our further discussion any flow variable $\Phi(t)$ is considered to consist of a temporal mean part $\overline{\Phi}$ denoted by an overbar and a fluctuating part with zero mean value $\Phi'(t)$ denoted by a prime. For a detailed definition of statistic properties see appendix D. From a measurement, a quantity $\Phi(t)$ is not obtained as a continous function. Instead, in a time period τ, discrete values Φ^t are recorded for example at an acquisition frequency f_{aq}, where the upper index t runs from $t = 1$ to the number of recorded points $t = N$ calculated from $N = f_{aq} \cdot \tau$.

The data acquisition is performed by two independent systems. Quantities for which we are only interested in their temporal mean value i.e. the temperatures of the copper plates, the supplied power, and the magnitude of the magnetic field, are acquired at an

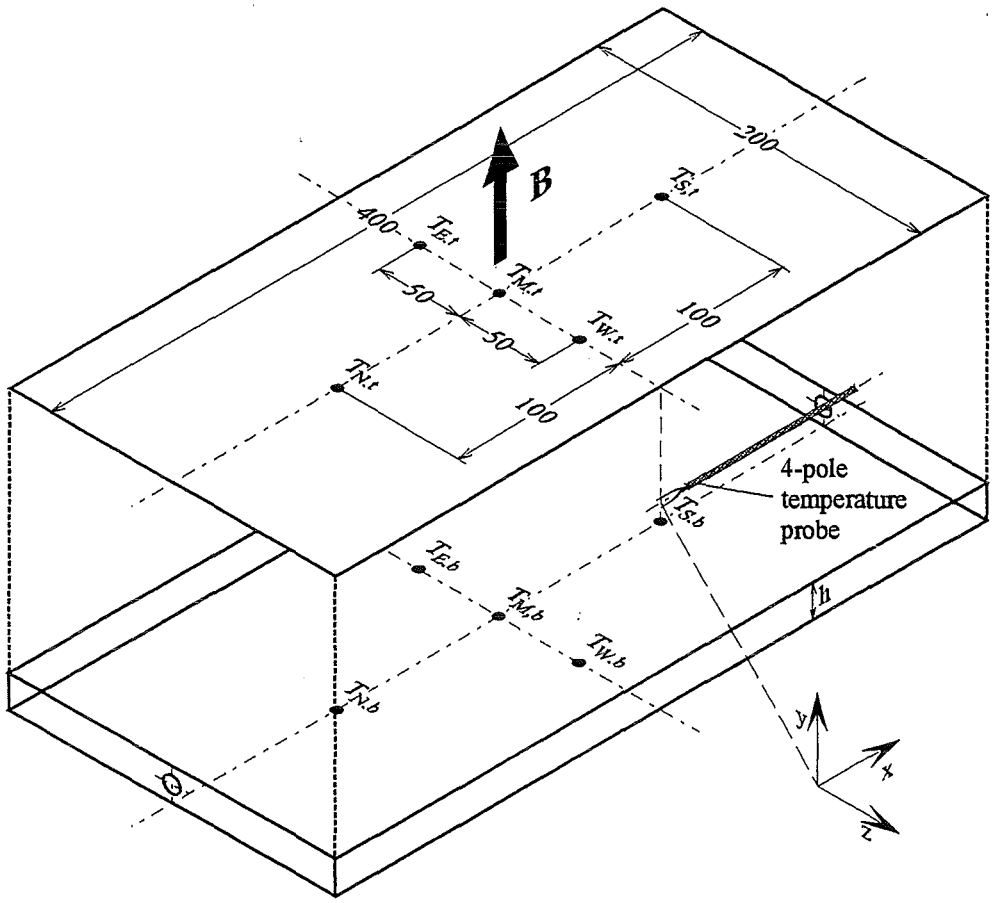

Figure 10: Instrumentation of the heat transfer test facility. Five $Cu - CuNi$ thermocouples are placed at the upper and the lower fluid wall interface to obtain integral heat transfer characteristics. Right in the middle of the fluid layer, between the thermocouples $T_{S,b}$ and $T_{S,t}$, a four-element temperature probe is placed in order to investigate local time-dependent flow quantities. All lengths are given in mm.

acquisition frequency $f_{aq} = 1/30s$ by a data logger. The thermo-voltages U_T obtained from the thermocouples are measured in reference to an ice point ($0°C$) thermocouple reference, and the temperature values in $T[°C]$ are calculated from the standard polynom for $Cu - CuNi$ thermopairing given in appendix C.

The spacial averages of the temperatures at the lower T_b^t and the upper T_t^t fluid-wall interface are determined in each time step from the non-weighted averages of the corresponding five thermocouples as

$$T_b^t = \frac{1}{5}\left(T_{M,b}^t + T_{N,b}^t + T_{S,b}^t + T_{E,b}^t + T_{W,b}^t\right), \tag{10}$$

$$T_t^t = \frac{1}{5}\left(T_{M,t}^t + T_{N,t}^t + T_{S,t}^t + T_{E,t}^t + T_{W,t}^t\right). \tag{11}$$

The temperatures of the copper plates and the non dimensional numbers are calculated for each time step with physical properties based on the mean temperature of the fluid

$$T_m^t = \frac{T_b^t + T_t^t}{2}. \tag{12}$$

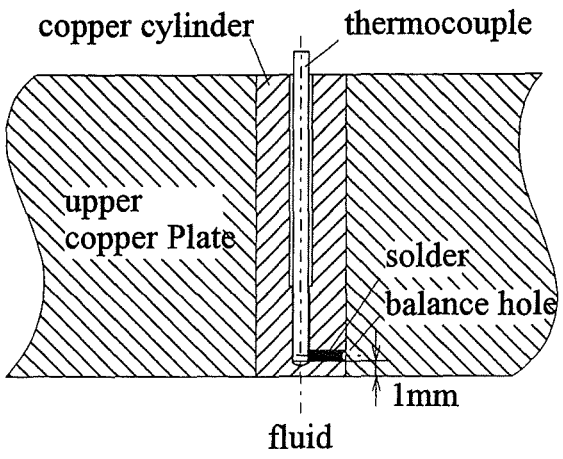

Figure 11: Fitting of thermocouples in the lower and upper copper plates. Perfect thermal contact of the thermocouple is obtained by soldering it into copper cylinders. The measurement position is about $1mm$ apart from the fluid-wall interface.

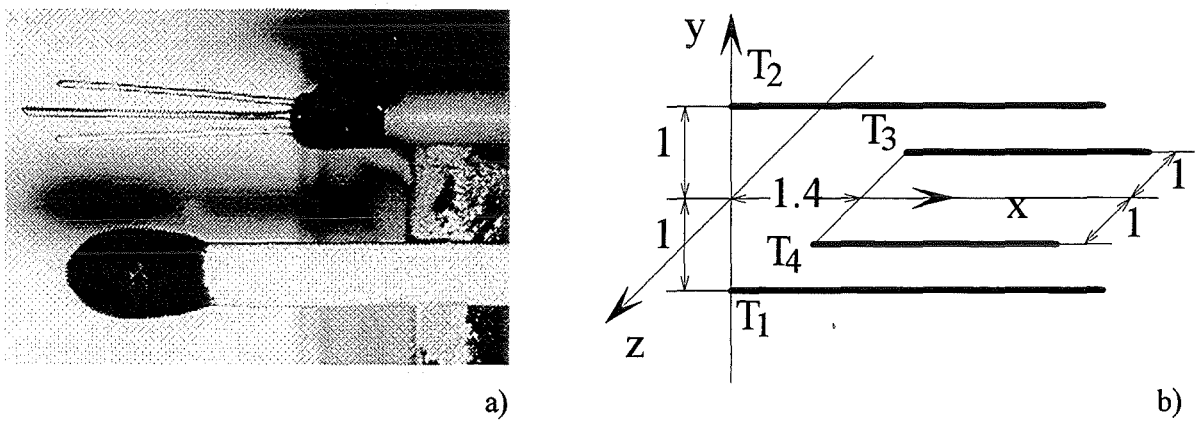

Figure 12: Four-element temperature probe. a) Sensing tip in comparison with a match. b) Geometry of the sensing tip and coordinates.

From these individual time series the temporal mean values are calculated. As we are not interested in the temporal variations of characteristic numbers or the temperature difference across the layer the averaging procedure is not indicated in the presentation of results e.g. by $Ra = \overline{Ra}$.

The time dependent thermo-voltages of the four-element-thermocouple probe are recorded simultaneously by a data acquisition card fitted into a second Personal Computer. In order to obtain a long time range reference for the thermopotential, the thermocouples are first connected to an ice point before their signals are amplified by standard DC amplifiers with a gain of $G = 500$. The temperature values in $T[°C]$ are calculated from the thermovoltages using the standard polynom for $Ni - CrNi$ thermopairing given in appendix C. With the use of amplifiers the resolution and the signal to noise ratio of the measurement is significantly increased. But it turnes out, that the mean values of temperature were

	$\overline{T'^2}[K^2]$
T_1	$8.69873 \cdot 10^{-3}$
T_2	$9.63485 \cdot 10^{-3}$
T_3	$8.73276 \cdot 10^{-3}$
T_4	$1.10414 \cdot 10^{-2}$

Table 2: ms-values of the probe signals, when the test section is not heated (pure noise)

not obtained with sufficient accuracy due to shifts in the amplifier-offsets. Therefore the probe measurements are limited to temperature fluctuations.

The data acquisition card provides $12bit$ resolution of the range $-5V < U < 5V$, where U is the voltage obtained from the amplifiers. The thermo-voltages are therefore resolved to an accuracy of

$$\delta U = \frac{10V}{2^{12}G} = 4.883 \cdot 10^{-6}V. \tag{13}$$

The resolution of the temperature signals δT is calculated from

$$\delta T = \delta U \cdot \left.\frac{dT}{dU}\right|_{\overline{T_m}} \tag{14}$$

with the sensitivity of the thermocouple dT/dU at the temperature $\overline{T_m}$ defined by equation 47 in appendix C. At $T_m = 120°C$ a resolution of $\delta T = 0.12°C$ is obtained.

For a careful discussion of time dependent data the contribution of random noise to the signal has to be known. Therefore measurements of the probe signals were taken, when the test section was not heated and the signal is therefore subject to pure noise.

The rate of time dependance or the intensity of a signal Φ' is easily quantified by the mean square (ms-) value $\overline{\Phi'^2}$ (see appendix D.1). In table 2 the ms values of all four thermocouples are summarized.

From the power spectra S we can estimate the contributions of fluctuations of distinct frequencies f_n to the ms-values of the signal (see appendix D.3). As power spectra calculated from one time series are influenced by statistical errors we lower these statistical errors by calculating the averaged power spectra $< S >_M$ from M samples. In figure 13, the averaged power spectra $< S >_{64}$ of all four thermocouple signals are plotted. The constant values above $0.1Hz$ are related to random noise. At smaller frequencies, some systematic disturbances are indicated by the increasing values of $< S >_M$. At this point of the discussion we can not interpret the level of noise, but we will use these measurements for the interpretation of the results obtained, when a heat flux is applied to the layer.

If we assume a time dependant signal $\Phi(t)$ to be a superposition of a part caused by the flow $\Phi_r(t)$ and a part caused by some random disturbances $\Phi_s(t)$

$$\Phi(t) = \Phi_r(t) + \Phi_s(t), \tag{15}$$

the ms-values $\overline{\Phi'^2}$ and the contributions of frequency f_n to the energy spectra $< S_r >_{M\to\infty}$ related to the flow can be calculated from the measured values substracting the contribution of noise (see appendix D.4) as follows

$$\overline{\Phi_r'^2} = \overline{\Phi'^2} - \overline{\Phi_s'^2}, \tag{16}$$

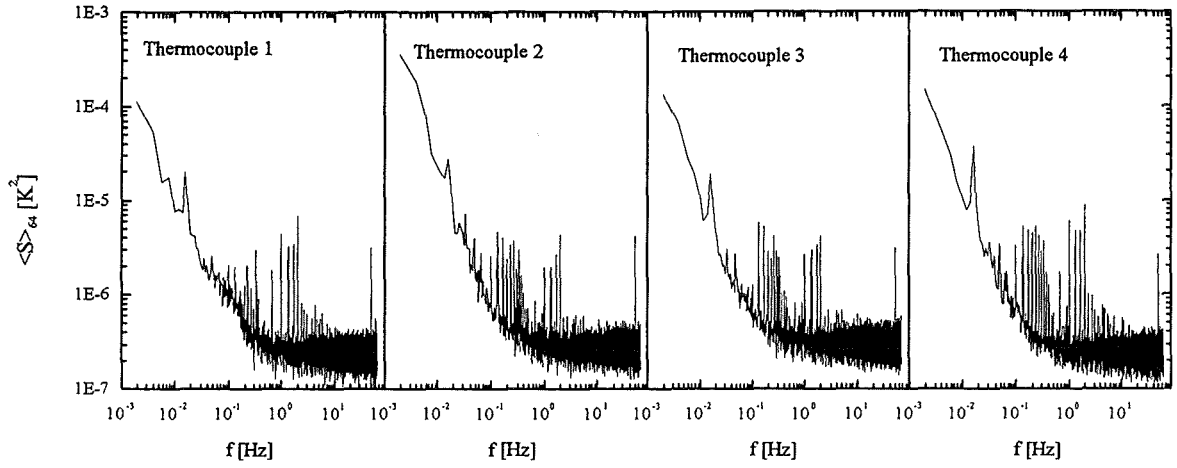

Figure 13: Power spectra $< S >_{64}$ of temperature recorded by the probe in the middplane. The measurements wer taken when the test section was not heated and therefore the power spectra are related purely to noise.

$$< S_r >_{M\to\infty} = < S >_{M\to\infty} - < S_s >_{M\to\infty} . \tag{17}$$

In addition, the signal to noise ratio Γ is given by

$$\Gamma = \frac{\overline{\Phi'^2}}{\overline{\Phi_s'^2}} \tag{18}$$

and for each contribution with frequency f_n to the power spectra by

$$\Gamma_n = \frac{< S >_M}{< S_s >_M}. \tag{19}$$

3 Performing of experiments and evaluation

3.1 Power supply

One general difficulty in performing natural convection experiments is that their temporal dynamics exhibit long time-scales. This requires to maintain constant conditions in an experiment for long time ranges up to several hours in order to obtain good statistics. Especially at low heating power the Nusselt number is very sensitive to variations of the electric power and the range below $2400W$ was therefore covered by controlled power units. Above powers $P > 2400W$ non-controlled units had to be used and variations of the electric power network may therefore influence the measurements. In figure 14 time series of the electric power P are compared with the mean temperature of the fluid T_m and the temperature difference across the layer $\Delta T = T_b - T_t$. In figures 14a and b an electric power of $P = 199.64W$ and $P = 2419.45W$ is supplied by the controlled unit. In figure 14c an equivalent power of $P = 2353.88W$ to the one in figure 14b is supplied by the non-controlled unit. With the controlled unit the variations of the electric power around the mean value are less than 0.03%. The observed variations of the mean temperature and the temperature difference across the layer are not coherent to the ones of the power.

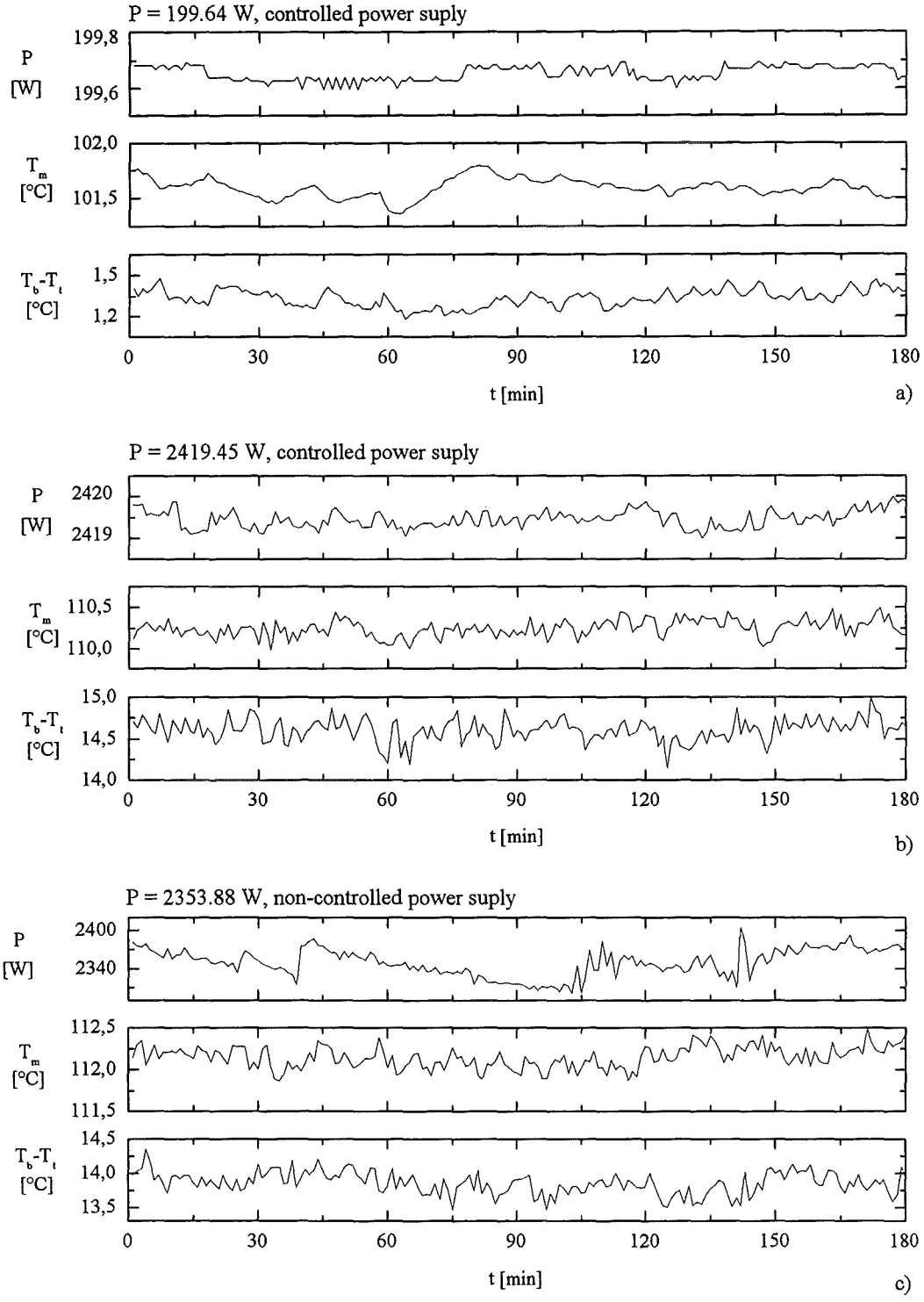

Figure 14: Time series of the electric power P, the mean temperature of the fluid T_m and the temperature difference across the layer $\Delta T = T_b - T_t$. In figures a) and b) the power is suplied by a controled unit. In figure c) the same power like in b) is suplied by a non-controled unit.

From this we can conclude that the variations of the power do not affect the temperatures in the test facility. We conjecture that at this low power the variations of the temperatures may be due to unstable thermodynamic phenomena controlling the heat removal from the facility.

The variation of the electric power of the non-controlled unit around the mean value is significantly higher ($\approx 2\%$) than for the controlled unit. But nevertheless the heat capacity of the copper plates is high enough that these variations are not observable in the time series of the temperatures.

3.2 Heat losses

The electric power supplied to the bottom copper plate is the major control parameter of the test facility. It directly determines the heat flux passing the layer and governs therefore the temperature difference across the layer, respectively the Rayleigh number. As the temperature difference across the layer is measured by thermocouples, the Rayleigh number is calculated independently of the applied heat flux, but the heat flux directly enters the Nusselt number and has therefore to be determined with high accuracy.

The heat flux q can not be calculated directly from the applied electric power P even though it has been measured with high accuracy. The facility is subjected to different sources of heat losses that have to be taken into account.

1. There is heat conduction in the stainless-steel side walls confining the layer. The losses are calculated directly from

$$P_s = A_{SS} \cdot \lambda_{SS} \frac{\Delta T}{h}, \tag{20}$$

   where $A_{SS} = 1.8 \cdot 10^{-3} m^2$ is the cross-section area of the side walls and $\lambda_{SS} = 15 W/mK$ the heat conductivity of stainless-steel.

2. The test section operates at temperatures above $100°C$ in an environment of about $20°C$. Therefore heat conduction from the lower plate through the insulation to the environment occurs. The losses due to this effect are modeled linearly with the temperature difference $T_b - T_e$ between the lower plate (T_b) and the environment (T_e), that is measured for this purpose, and a coefficient C_b. This gives:

$$P_b = C_b (T_b - T_e). \tag{21}$$

3. Ohm's losses P_{el} occur in the wiring of the heater rods. Assuming a constant ratio of the ohmic resistance of the wiring and the heater rods C_{el}, Ohms's losses can be modeled to be proportional to the applied electric power P. This results in

$$P_{el} = C_{el} P. \tag{22}$$

With the unique feature of a sufficiently high magnetic field to suppress any convective motion, the state of pure heat conduction can be generated at any heating power and temperature of the lower copper plate. This well determined conduction state can be

used to determine the influence of the unknown contributions of heat losses 2 and 3 on the total balance of heat at the lower copper plate, where

$$P = P_{lm} + P_s + P_b + P_{el} \tag{23}$$

holds. P_{lm} is the amount of heat per unit time being transfered from the lower copper plate by heat conduction through the liquid-metal-layer. It can be calculated from Fourier's law as

$$P_{lm} = -\lambda A \frac{\Delta T}{h}, \tag{24}$$

using the measured temperature difference and the base area of the liquid metal layer $A = 0.08m^2$. At low heating power the contribution of Ohm's losses can be neglected ($P_{el} \approx 0$) and we can calculate the heat losses to the environment from equation 23 as

$$P_b = P - P_{lm} - P_s. \tag{25}$$

Here $C_b = 0.81078$ is obtained from equation 21 by fitting several subcritical values.

Next we use the contribution of heat losses to the environment calculated by equation 21 to obtain the Ohm's losses from the balance of heat at high heating powers. We get

$$P_{el} = P - P_{lm} - P_s - P_b. \tag{26}$$

In figure 15 the resulting Ohm's losses are plotted versus the applied electric power. According to equation 22 a linear increase of heat losses is expected for increasing power.

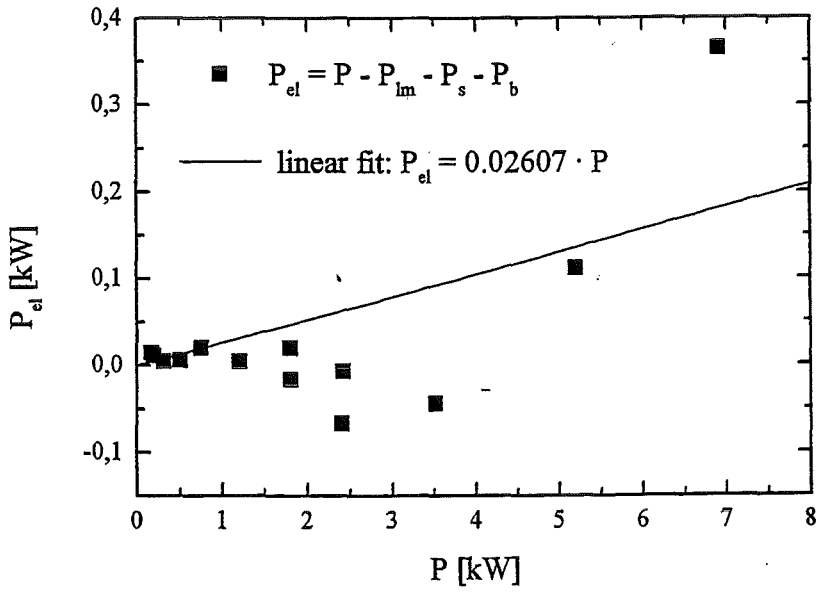

Figure 15: Heat losses in the wiring of the electrical heater rods determined from equation 26. The state of pure heat conduction was achieved by applying a suitable high magnetic field to suppress convective motions.

Instead of this, the Ohmic heat losses are first decreasing before they increase again with the applied electric power. This non-physical behavior can only be explained by an inaccuracy of our knowledge about the temperature dependent thermal conductivity λ,

used for the calculation of the heat passing the layer according to equation 24. However, a linear interpolation of the obtained data leads to a reasonable value of $C_{el} = 0.0261$ for the coefficient of Ohm's losses which practically means, that 2.61% of the electrical power is deposited in the wiring and not in the heated copper plate.

The amount of heat passing the layer per unit time P_{lm}, respectively the heat flux q may now be calculated from

$$P_{lm} = P - P_{el} - P_b - P_s \tag{27}$$

and

$$q = \frac{P_{lm}}{A} \tag{28}$$

no mater wether there is convective heat transport or not.

3.3 The test matrix

In order to get a broad overview of the natural convection phenomena in the test facility, a first test matrix ($M1$) covering the whole range of achievable parameters is provided. The experiments are carried out by applying a defined heat flux and a magnetic field to the layer and waiting for a long enough time to overcome transient effects before the measurements are started. The recording time was chosen such that good statistics are achieved for the mean values of the stationary quantities like Rayleigh and Nusselt numbers as well as for the ms-values of the probe.

A more elaborate evaluation of the temporal behavior of the flow, including power spectra, is performed using longer time-series taken at a constant Rayleigh number of $Ra = 5 \cdot 10^4$ ($M2a$) and at a constant heating power of $P = 2400W$ ($M2b$).

The magnitude of the applied magnetic field is varied between $0.00T < B < 0.09T$ to obtain the Chandrasekhar numbers $Q = 0, 100, 400, 784, 1600, 14400$. In appendix E the parameters of all experiments are summarized.

4 Results

4.1 Integral heat transfer characteristics

4.1.1 Ordinary hydrodynamic (OHD) flow as a reference case

Before we discuss the influence of the magnetic field on the convective motion, the principle effects of increasing the temperature difference across the layer by increasing the applied electric power are illustrated for the OHD flow ($Q = 0$) and the reliability of measured data is checked against known experimental and numerical results.

If we apply a defined heat flux q to the layer, we obtain a temperature difference ΔT related to the heat transfer characteristics of the liquid metal. From the measured temperature difference a conductive heat flux q_0 can be calculated from Fouriers law (equation 5) and compared with the applied heat flux. In figure 16a both heat fluxes are plotted versus the temperature difference. In addition, the mean temperature of the fluid used for the evaluation of physical properties is plotted.

The dots represent measured values evaluated from the test matrix $M1$. As the temperature of the upper copper plate is almost fixed by the boiling temperature of the water

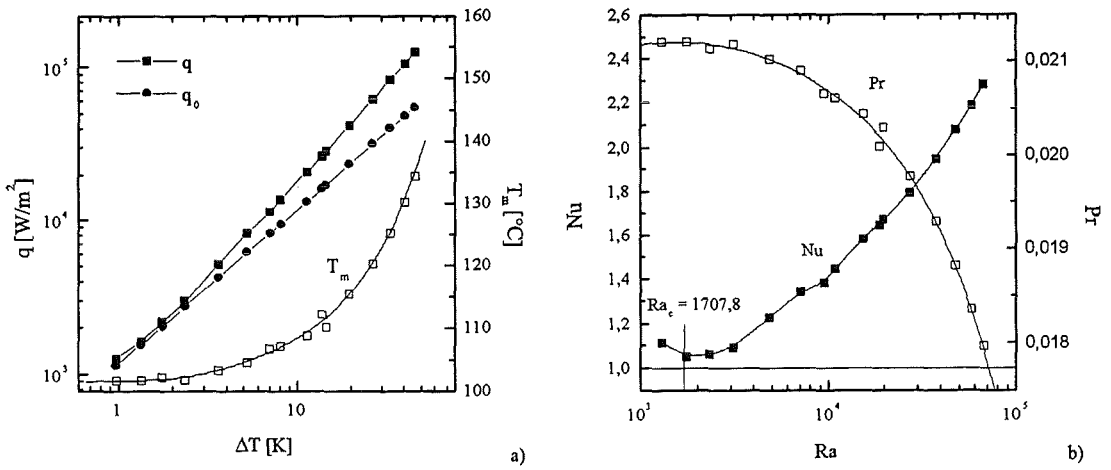

Figure 16: a) Measured applied heatflux q, calculated convductive heat flux q_0 and mean temperature of the fluid versus the measured temperature difference across the layer ΔT. b) Nusselt- and Prandtl numbers, evaluated from the same measurements, versus the Rayleigh-number.

pool, higher temperature differences are related directly to increasing mean temperatures. But as the temperature dependance of the heat conductivity is only weak, the conductive heat flux increases almost linearly with the temperature difference across the layer. At small temperature differences the applied heat flux coincides with the conductive one indicating that heat is transported through the layer by pure heat conduction. Above $\Delta T \approx 2K$ the slope of the applied heat flux is increased and thus values higher than the conductive heat flux are obtained. This indicates that an additional convective transport of heat by a moving fluid has now been established. The temperature difference at which the increase in the slope first occurs is the critical temperature difference for the onset of convection.

In figure 16b the results of figure 16a are presented in non-dimensional form referring to Nusselt , Prandtl and Rayleigh numbers. The increasing temperature difference is now represented by increasing Rayleigh numbers. By the increasing mean temperature of the fluid the physical properties are changed. This results in a decrease of the Prandtl number from Pr ≈ 0.021 to Pr ≈ 0.018.

The contribution of the convective heat transport is characterized by the Nusselt number, the ratio of the applied heat flux to the conductive heat flux respectively, defined by equation 4. When the values of both heat fluxes are the same, we obtain $Nu = 1$ and for higher heat fluxes compared to the conductive one, the occurrence of a convective heat flux is indicated by $Nu > 1$.

Even for conditions where we find in figure 16a the state of pure heat conduction at nearly equal values of the heat fluxes, the Nusselt number is slightly above one. We conjecture that this deviation from the theoretical value one is caused by errors in the determination of heat losses.

Above the theoretical critical value of $Ra_c = 1707.8$ the Nusselt number starts to emerge so slowly from the state of pure heat conduction, that we cannot confirm the critical Rayleigh number with the overall accuracy of the used facility. At $Ra \approx 3000$ a

faster, almost linear, increase of the Nusselt number with Rayleigh number is observed.

As the Prandtl number of NaK is close to the one of mercury ($\mathrm{Pr}_{Hg} \approx 0.025$), we can compare the Nusselt numbers at large supercritical Rayleigh numbers in figure 17 with experimental results by Rossby (1969) and numerical simulations by Bunk and Wörner (1998). The Nusselt numbers obtained in the present experiment are all smaller than

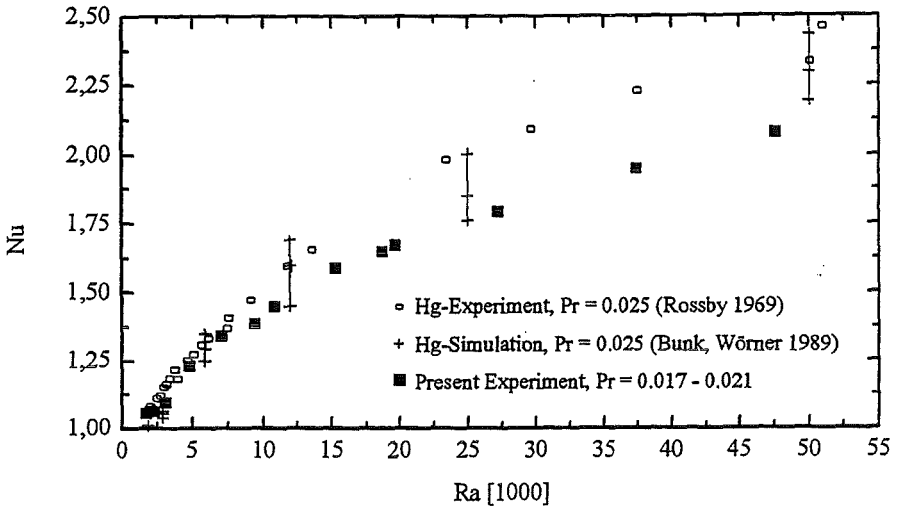

Figure 17: Experimental and numerical Nusselt-numbers obtained for mercury compared with the results of this expreriment for hydrodynamic flow ($Q = 0$).

both the experimental and the numerical values in mercury. Although we did not expect the heat transfer differences between the two different liquid metals to be so high, this result may be explained by the lower Prandtl number of sodium-potassium (see figure 3) compared with the one of mercury.

4.1.2 MHD-convection

The convective flow is generally determined by non-dimensional numbers representing the ratios between the forces acting on the fluid. A clear understanding of the phenomena is facilitated by keeping all but one characteristic number constant and varying the remaining one to evaluate precisely its effect on the flow. If we are for example interested in the influence of the magnetic field on the convective flow we keep the driving force represented by the Rayleigh number constant and vary the Chandrasekhar number. The Nusselt number is such determined as a function of Rayleigh and Chandrasekhar number for fixed Prandtl number determined by the physical properties of the fluid.

In figure 18 Nusselt numbers evaluated from the test matrix $M1$ are plotted versus the Rayleigh number.

The different symbols represent measured points at uniform Chandrasekhar numbers. They are connected by solid polynomial fitting curves with the Chandrasekhar numbers plotted at the right ends of the curves. The critical Rayleigh numbers for the onset of convection at the distinct Chandrasekhar numbers are marked by the vertical lines. The values are obtained from a polynomial fit of the results provided by Chandrasekhar

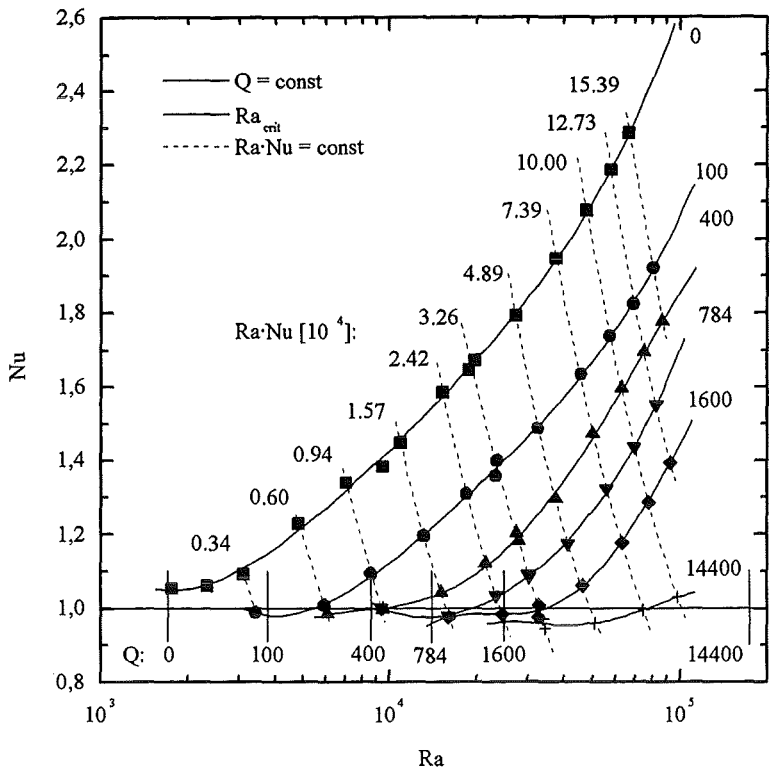

Figure 18: The increase of Nusselt numbers Nu with Rayleigh number Ra for different Chandrasekhar numbers Q. The dots indicate measured points. They are connected by polynominal fitting curves. The critical Rayleigh-numbers known from linear theory are given for each Chandrasekhar number by vertical lines. The dashed lines connect points of uniform heat flux respectively where $Ra \cdot Nu$ is constant.

(1961) (see appendix 40). The limiting state of pure heat conduction is indicated by the horizontal line $Nu = 1$. Although large effort has been made to measure precisely the applied power and the heat losses (see section 3.2), Nusselt numbers of exactly one are not obtained even at subcritical Rayleigh numbers. Especially for the highest Chandrasekhar number of $Q = 14400$ a continuous increase of the Nusselt number is observed even though all measured points are subcritical. This observation supports the conjecture already made in section 3.2 that the temperature dependence of the heat conductivity $\lambda(T)$ follows some other law than given by equation 40 (see appendix A.1). However no other data for the physical properties are available and thus, we have to accept the present situation.

For all Chandrasekhar numbers an increase of the Rayleigh number at supercritical conditions causes a monotonous increase of the Nusselt number. At constant Rayleigh number, respectively constant temperature difference across the layer, the Nusselt numbers decrease with increasing Chandrasekhar numbers. Thus, less heat is transported through the layer due to the damping effect of the magnetic field.

In technical heat transfer problems the discussion of flow properties at constant Rayleigh number is related to situations where the temperatures of the heat source and the heat sink are fixed and a heat flux arises from this driving temperature difference. If convec-

tive transport is efficient the heat flux becomes larger what will be reflected by increasing Nusselt numbers. This situation occurs in problems where heat transfer through a liquid filled cavity are important and any damping effect results in an improvement of thermal insulation.

However, in most, technically relevant cases the driving temperature difference for heat transfer is not fixed. Instead, a given amount of heat has to be transported from a heat source to a heat sink. If convective transport is efficient, the temperature difference becomes small and assuming the temperature of the heat sink is given, the temperature of the heat source becomes smaller. This situation holds for most heat removal problems where the temperature at the cold end of the system is determined by the available cooling water and the temperature at a heat loaded wall has to be limited. For an investigation of this situation we keep the heat flux constant and see the influence of the magnetic field on the temperature difference across the fluid. This will result in different Rayleigh and Nusselt numbers when the Chandrasekhar number is varied.

In figure 18 values obtained at uniform heat flux are connected by dashed lines. The magnitude of the heat fluxes are given in non-dimensional form by the product $Nu \cdot Ra$ plotted at the upper end of the curves.

If we start at some measured point obtained at $Q = 0$ and follow the line of constant heat flux to higher Chandrasekhar numbers, the Rayleigh number increases. From the point of heat removal this is a negative effect of the magnetic field because the temperature of the cold end of a facility has to be decreased in order to obtain the same temperature at the, in most applications critical, hot end.

The obtained values for the Nusselt number can only be discussed with respect to the Prandtl number that is subject to the mean temperature of the fluid reached in the experiment. In figure 19 the Prandtl numbers of all measurements are plotted as a function of the Rayleigh number. From a practical point of view, the Prandtl number depends

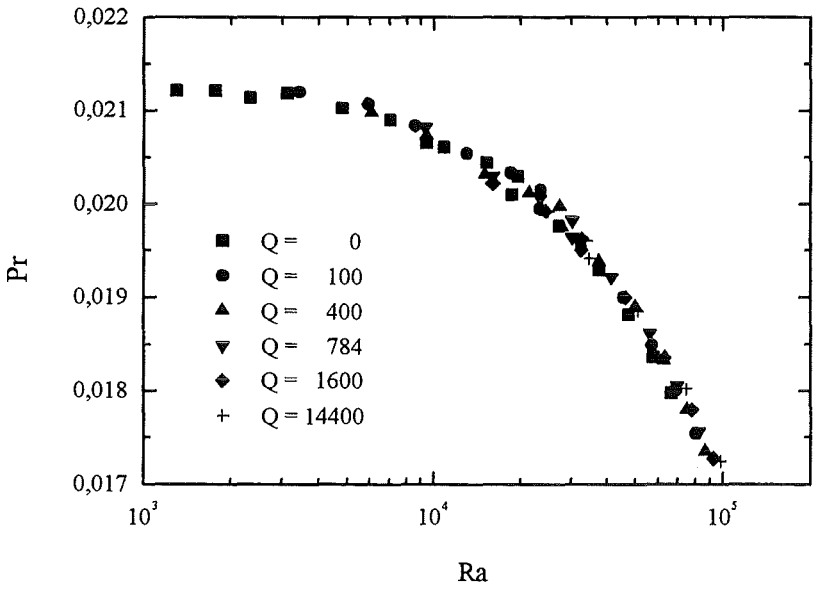

Figure 19: Prandtl numbers Pr obtained in the test section for different Rayleigh and Chandrasekhar numbers.

only on the Rayleigh numbers realized in the experiment. The influence of different Chandrasekhar numbers is not significant.

For studying the characteristics of heat transfer besides the damping effect of the magnetic field, the Nusselt numbers obtained at different Chandrasekhar numbers are plotted in figure 20 as a function of a modified Rayleigh number defined as

$$Ra_m = \frac{Ra}{Ra_{crit}} - 1, \tag{29}$$

The critical Rayleigh number used in this definition is calculated from equation 69 (see appendix 40).

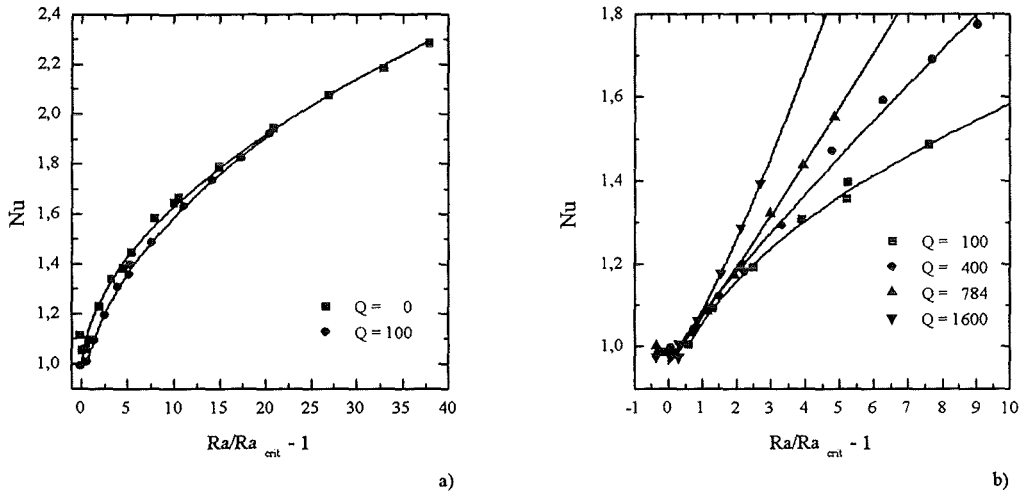

Figure 20: Nusselt numbers Nu versus the modified Rayleigh number $Ra_m = Ra/Ra_{crit} - 1$. a) comparison of hydrodynamic flow at $Q = 0$ with MHD-flow at $Q = 100$. b) the effect of increasing Chandrasekhar number further up to $Q = 1600$.

First, the Nusselt number of hydrodynamic convection at $Q = 0$ is compared with values at $Q = 100$ in figure 20a. At the point of neutral stability ($Ra_m = 0$) the Nusselt number of hydrodynamic flow is determined to be larger than unity, whereas the imposition of a moderate magnetic field results in $Nu = 1$ indicating pure heat conduction. As the mean temperature of the fluid is comparable for both measurements, we interpret this phenomenon to be caused by a large scale convective motion probably induced by non-perfect thermal boundary conditions in the test section which is suppressed by the magnetic field already at $Q = 100$. Besides the differences around the critical point, the Nusselt numbers for $Q = 0$ and $Q = 100$ are similar with a weak tendency of smaller values for magnetohydrodynamic convection.

The effect of increasing Chandrasekhar numbers is illustrated in figure 20b. For all magnetic fields the onset of convection is observed at slightly higher Rayleigh numbers than predicted by theory. This observation is presumably due to the fact, that by searching for Nusselt numbers larger than one, we determine the onset of significant or at least measurable convective heat flux and not the onset of any marginal convective motion that, especially in the case of small Prandtl numbers present here, does not contribute significantly to the heat flux through the layer. Thus by looking for the onset of significant

convective heat flux in an experiment, we determine always Rayleigh numbers beyond the critical point determined theoretically by Chandrasekhar (1961).

The Nusselt numbers for different Chandrasekhar numbers are increasing with the modified Rayleigh number at different rates and generally higher Nusselt numbers are obtained at higher Chandrasekhar numbers. Thus at the same modified Rayleigh number the convective heat transport is more efficient at higher magnetic fields. This can be explained by the higher efficiency of convective rolls with smaller horizontal length-scale that are present at higher Chandrasekhar-numbers (see section 1.2) or it is just due to the applied rescaling of supercritical conditions.

4.2 Temporal characteristics of the flow

Most MHD flows under laboratory conditions are well described by the limiting case $Pm \ll 1$. In this case the non-dimensional conservation equation of momentum

$$\frac{1}{\mathrm{Pr}}\left[\frac{\partial \mathbf{v}}{\partial t} + (\mathbf{v}\cdot\nabla)\,\mathbf{v}\right] = -\nabla p^* + \Delta\mathbf{v} + RaT\mathbf{e}_y + Q\,(\mathbf{j}\times\mathbf{B}) \tag{30}$$

and the temperature equation

$$\frac{\partial T}{\partial t} + (\mathbf{v}\cdot\nabla)\,T = \Delta T \tag{31}$$

are obtained from the Navier Stokes- and the temperature transport equations by introducing the scales h, κ/h, h^2/κ, ΔT, B_0, $\sigma B_0\kappa/h$ and $\kappa B_0 h$ for length, velocity, time, temperature, magnetic field, current density and electric potential (see Burr and Müller (1997)). Here $p^* = h^2(p+\rho g h)/(\rho\nu\kappa)$ is the non dimensional pressure obtained from rescaling the dimensional one p and $\mathbf{e}_y$ the unit vector directed opposite to the direction of gravity.

The non linear inertial forces enter the momentum equation as inversely proportional to the Prandtl number. Thus for liquid metals with small Prandtl numbers a transition to time dependent flow must be expected above a narrow band of stable convection (see section 1.1 and 1.2). With the instrumentation of this experiment it is not possible to sense flow patterns as are predicted by numerical works of Clever and Busse (1989) and Busse and Clever (1996) but we can use the statistical properties of the time dependent signals obtained from the multi-element temperature probe in the center of the liquid metal layer to confirm numerical predictions and to broaden our present understanding of the dynamical phenomena.

With the above scaling flow properties can be presented in non-dimensional form, what will be practiced furtheron if not mentioned otherwise.

4.2.1 The onset of time dependent flow and its influence on the Nusselt-numbers

Clever and Busse (1989) investigated numerically the properties of finite amplitude convection in the transition regime from laminar to time-dependent flow for Prandtl numbers $\mathrm{Pr} = 0.1$ and $\mathrm{Pr} = 0.025$. In figure 21 the increase of the Nusselt number at various Chandrasekhar numbers and a Prandtl number of $\mathrm{Pr} = 0.025$ is plotted versus the difference

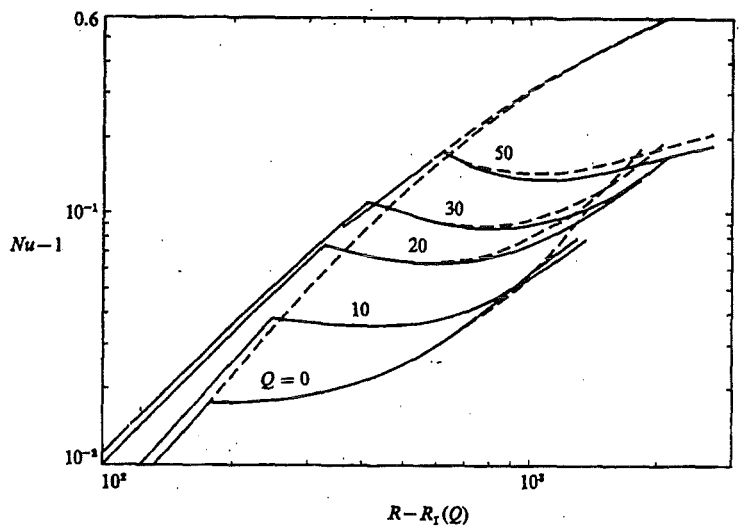

Figure 21: Numerical predictions made by Clever and Busse (1989) for the onset of time-dependent convection and its influence the slope of the Nusselt number. Values at different Chandrasekhar numbers are plotted versus the reduced Rayleigh number $Ra_r = Ra - Ra_c$.

between the actual Rayleigh number and the critical Rayleigh number $Ra - Ra_c$. This difference will further be called the reduced Rayleigh number Ra_r.

Right above the critical reduced Rayleigh numbers ($Ra_r = Ra - Ra_c = 0$) the Nusselt numbers are strongly increasing due to a steady convective motion. Associated with the onset of time dependent travelling wave convection a substantial decrease in the slope of the Nusselt numbers occurs at first but for larger supercritical Rayleigh numbers the slope increases again. When the Chandrasekhar number is increased, the onset of time dependent flow is shifted to higher reduced Rayleigh numbers and the region of reduced slope is enlarged.

In order to detect these phenomena in our measurements we investigate the onset of time dependent flow by plotting the mean-square values of one particular temperature variance signal $\overline{T'^2}$ recorded by the probe versus the Rayleigh number and discuss the slope of Nusselt number around the transition point. In figures 22 (a-f) measured values of $\overline{T'^2}$ (denoted by squares referring to the left axis) are plotted together with the Nusselt number (denoted by dots referring to the right axis) for each Chandrasekhar number.

As measured mean-square values always suffer from noise, the transition point from stable but noise affected flow to real time dependent flow can only be determined when the level of noise is taken precisely into account. Therefore the mean-square values of pure noise (see section 2.3) are plotted as dashed lines in figures 22 (a-f). This level of noise decreases with the Rayleigh number due to the scaling of the temperature fluctuations with the temperature difference across the layer.

In ideal cases the onset of time dependent flow is indicated by the emerging of the measured ms-values from the level of noise. For higher Chandrasekhar numbers the measured ms-values are significantly higher than these of noise even at subcritical conditions. There are additional contributions to the level of noise resulting from operating the power supplies of the facility and the magnet that can not be taken into account. However, stationary flow is indicated by a similar negative slope of the measured values like that of

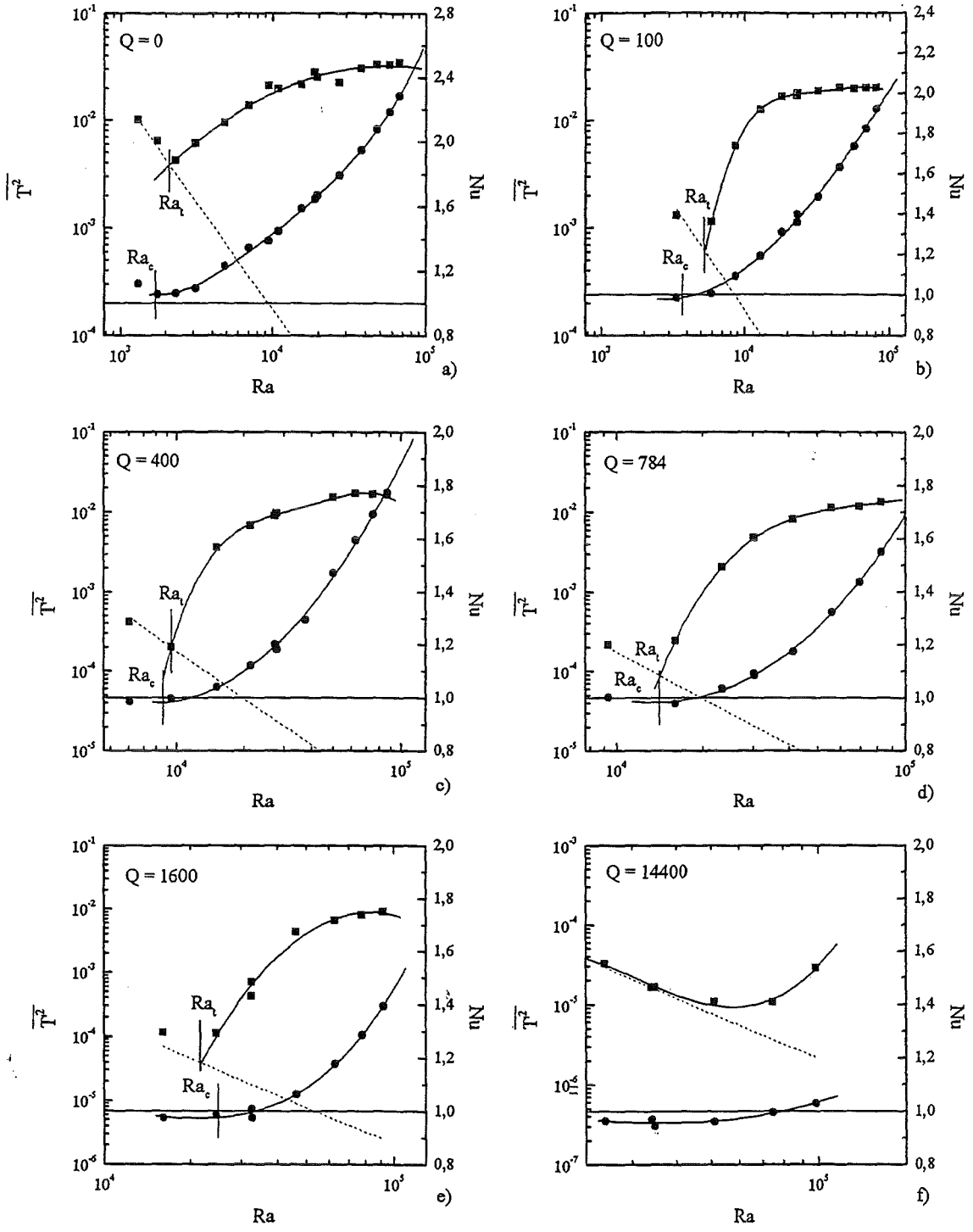

Figure 22: Onset of time-dependent flow and its influence on the heat transfer characteristics at different Chandrasekhar numbers. Squares refering to the left axis are mean-square values of temperature $\overline{T'^2}$ recorded by the probe. The level of noise is indicated by dashed lines with a slope of approximately -2. Circles refering to the right axis are Nusselt numbers. The onset of convection from linear theory is indicated by vertical lines $Nu = 1$.

noise i.e. a decrease as Ra^{-2}. Thus, observed values of $\overline{T'^2}$ may be clearly identified as being related to real time dependent flow. The critical Rayleigh number Ra_t for the onset of time dependent flow is now determined as the point where the polynominal fitting curves of time dependent values curves cross the dashed lines indicating the level of noise. Additionaly, the onset of convection as a stable motion predicted by the linear theory of Chandrasekhar (1961) is indicated in the figures by vertical lines. We have already seen in section 4.1.2 that the onset of convection may not be clearly identified from the measurements due to a lack of accuracy. If we compare the determined critical Rayleigh numbers for the onset of time dependent flow Ra_t with the critical Rayleigh number for the onset of stable convection, we can not observe broad regions of stable convection above critical conditions. However at high Chandrasekhar numbers (e.g. $Q = 784$ and $Q = 1600$) the onset of time dependent flow is even determined at smaller Rayleigh numbers than critical conditions.

In hydrodynamic flow Clever and Busse (1989) detected the onset of oscillations at $Ra_t = Ra_c + Ra_r \approx 1880$ and a region of reduced slope of the Nusselt number up to $Ra \approx 2700$. Although $Ra_t \approx 2000$ is found in the measurements, the resolution of this experiment is too poor to confirm the precise theoretical value. However, a region of reduced slope at marginal supercritical conditions is clearly identified in figure 22a.

The highest Chandrasekhar number investigated by Clever and Busse (1989) is $Q = 50$. If we extrapolate these results to our lowest value $Q = 100$ we obtain the onset of time dependent flow at approximately $Ra \approx 4800$ what is in reasonable agreement with the experimental findings. But at the transition point to time dependent flow we would have expected from the calculations of Clever and Busse (1989) a Nusselt number of about $Nu \approx 1.3$ before the decrease in slope sets in. This value can, all inaccuracies considered not be confirmed by the measurements. However a region of reduced slope is visible but below $Ra \approx 4800$.

When the reduced Rayleigh number is used as abscissa as done by Clever and Busse (1989) in figure 21, the region of laminar flow in the graph is considerably enlarged with increasing Chandrasekhar numbers as well as is the region of reduced slope in Nusselt numbers. In practice, however, the relative distance of a supercritical Rayleigh number to the critical one is of the same order of magnitude and therefore it is hardly resolvable by measurements. It is therefore not surprising that we do not see the effects more clearly at higher Chandrasekhar number.

Although for $Q = 14400$ (figure 22f) all Rayleigh numbers are subcritical according to linear theory, the Nusselt number is slightly increasing with the Rayleigh number. The ms values of the temperature are only increasing slowly with the Rayleigh number and are small compared to the values obtained at smaller magnetic fields. Thus an onset of time dependent flow that was proven to coincide practically with the onset of convection is not clearly indicated. The increase in the Nusselt number is therefore clearly not related to convective heat transport. It occurs, as already suggested before, from errors in the thermophysical data.

At supercritical values of the Rayleigh number the intensities of the temperature are all increasing fast with Rayleigh number towards a saturation level that seems to depend on Chandrasekhar number. In figure 23 the intensities of temperature from figure 22a-e are plotted versus the Rayleigh number in one graph. The level of noise is indicated by a solid line of slope -2. Although the saturation level is not reached especially for high magnetic fields, we can clearly conclude, that the ms-value of the final state at high

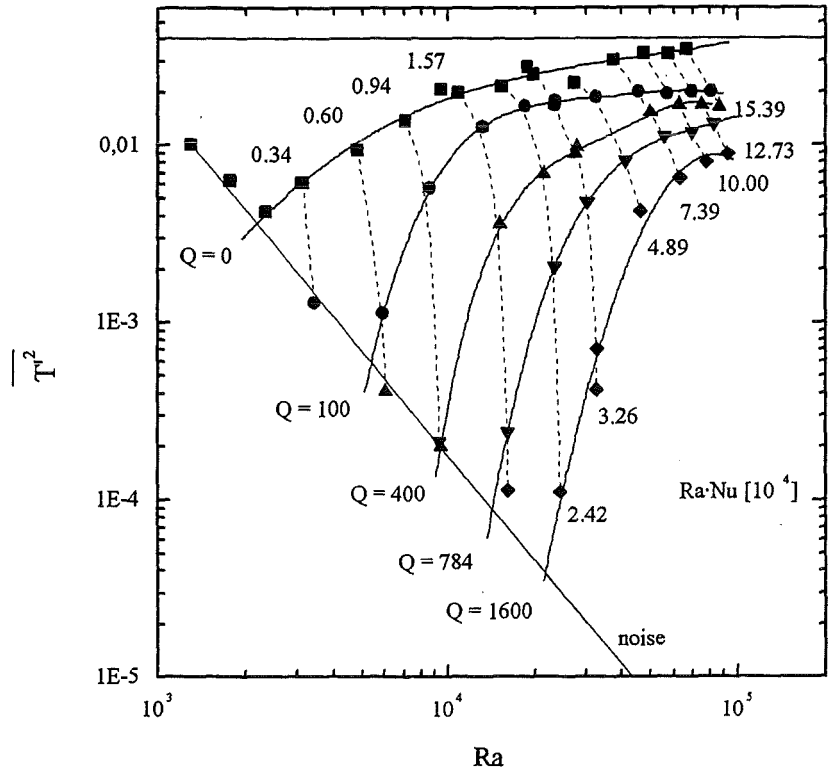

Figure 23: The influence of increasing Chandrasekhar numbers on the mean-square values of temperature $\overline{T'^2}$ recorded by the probe versus the Rayleigh number (dots connected by solid lines). Measurements of uniform heat flux are connected by dashed lines of $NuRa = const.$

Rayleigh numbers decreases with Chandrasekhar number. At hydrodynamic flow ($Q = 0$) a saturation level of about $\overline{T'^2} \approx 0.04$ is reached above $Ra \approx 10^5$. This value is similar to the observations of Kek (1989) (p.82) in sodium but due to the smaller Prandtl number of sodium the saturation level is reached in his experiments already at $Ra \approx 4 \cdot 10^4$.

The damping of fluctuations from Joule's dissipation has on the one hand the major benefit, as the use of magnetic fields in material processing with solidification may result in more homogeneous processing conditions. On the other hand, if we follow the dashed lines of constant heat flux i.e. $NuRa = const$ in figure 23, we observe that under this technically relevant boundary condition, the former benefit is balanced by an increase of the temperature difference across the layer, a fact already discussed in section 4.1.2. It has to be debated in any particular case of application wether the decrease of heat transfer can be accepted for the benefit of a suppression of time dependent flow.

4.2.2 The structure of time dependent flow

Time series: A first impression of the structure of the time dependent flow may be obtained from the fluctuating part of the temperature T' recorded by the probe. In figure 24 the influence of increasing the Rayleigh number from the subcritical value $Ra = 1295$ to supercritical values up to $Ra = 80924$ at hydrodynamic flow ($Q = 0$) is shown.

The temperatures are scaled with the measured temperature difference across the

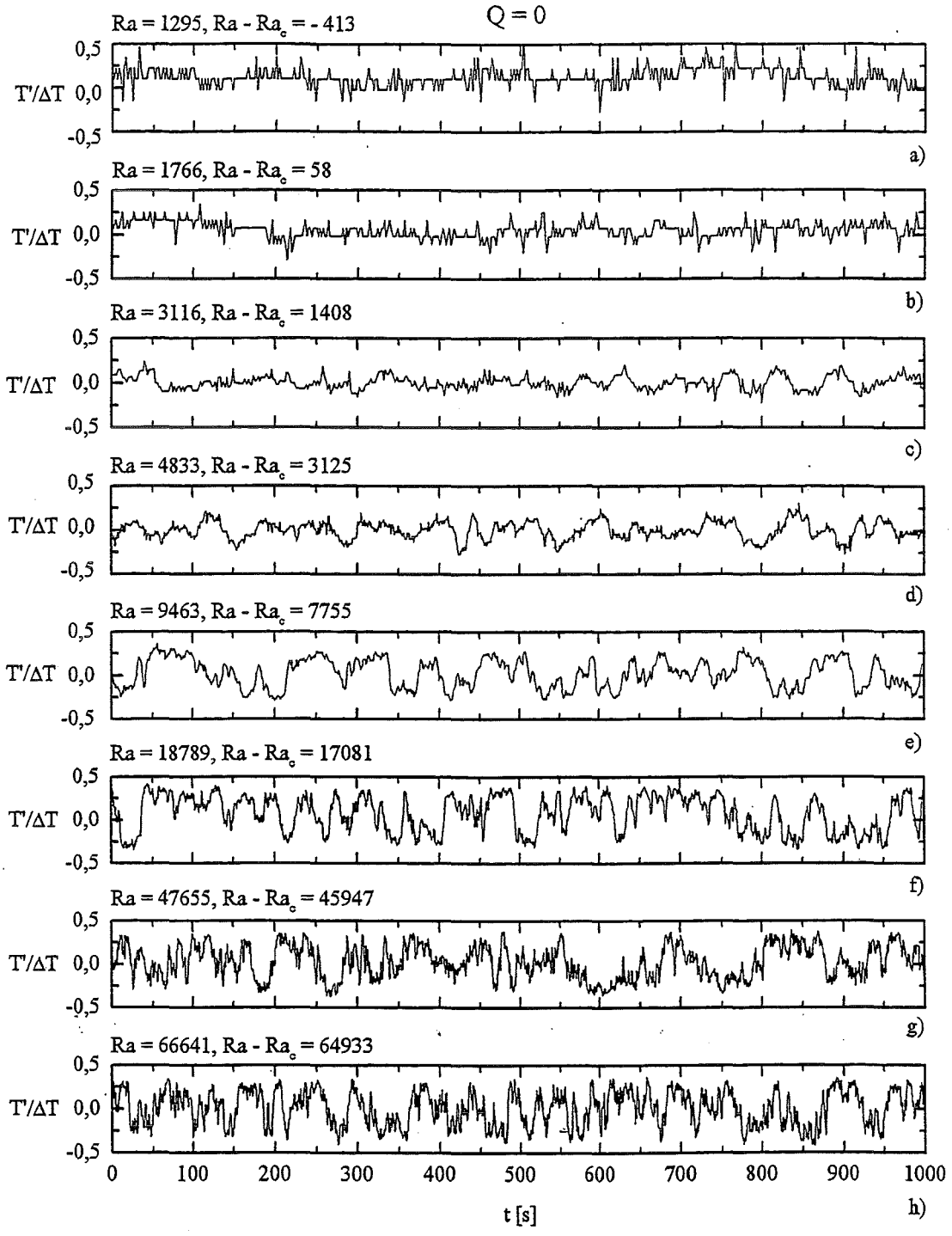

Figure 24: Time series of the fluctuating part of the temperature T' recorded by the probe for ordinary hydrodynamic flow at $Q = 0$. The Rayleigh number is increased from the subcritical value $Ra = 1295$ to supercritical values up to $Ra = 66641$. The temperature fluctuations are scaled with the temperature difference across the layer ΔT.

layer ΔT. For the abscissa we use the real time measured in seconds. At $Ra = 1295$ and $Ra = 1766$ the signals are dominated by the effect of noise. The small fluctuations of the thermopotentials are divided by the, in these cases, small temperature difference across

the layer, which results in large fluctuations without physical meaning. We have already seen this effect in figure 22a where, by comparing the data with the level of noise, the first two points have been determined to be in the regime of stable conditions. When the Rayleigh number is increased, the elevation of real fluctuations above therandom noise level becomes larger and we can observe above $Ra = 3116$ real time dependent flow, similar to the observations in figure 22a. Up to the Rayleigh number $Ra = 9463$ the flow is dominated by variations of the temperature on long time-scales. At higher Rayleigh numbers this time-scale decreases and, additionally, fluctuations on significantly smaller time-scales occur.

In figure 25 the same time-series are plotted for MHD flow at $Q = 100$.

Laminar flow at the subcritical Rayleigh number $Ra = 3415$ can now be identified more clearly. During the transition to strongly time dependent flow the time scale of the fluctuations is continuously decreasing. Moreover, if we compare the time series at $Q = 100$ with the hydrodynamic flow in figure 24 we observe significantly smaller time-scales for the MHD flow. Similar observations can be made at higher Chandrasekhar numbers as may be seen from figures 26, 27 and 28. The increasing intensity of the temperature signal to the noise level enables here to look more precisely to the flow of near critical conditions. In figure 26b we can identify stable convection at a supercritical Rayleigh number of $Ra = 9407$ and demonstrate thereby the existence of a region of stable convection. This observation is in agreement with the observation in figure 22c. At the high Chandrasekhar number $Q = 1600$ there are significant temperature fluctuations even at subcritical Rayleigh numbers (figures 28a and b as corresponding to figure 22e).

Integral time-scales: All time series show a chaotic behavior. Periodic signals corresponding to the computations of Clever and Busse (1989) and Busse and Clever (1996) can not be observed. However, in all time series a dominant leading characteristic time-scale is evident. In order to evaluate this feature objectively we calculate the autocorrelation functions defined by equation 56 (appendix D). As an example the autocorrelation functions at different Chandrasekhar numbers are plotted in figure 29 for a Rayleigh number of $Ra \approx 5 \cdot 10^4$.

From these correlations we obtain an integral time scale τ_I of the flow by integrating the autocorrelaton function (equation 56) from $\underline{t}= 0$ up to the point t_I where $A_k(\underline{t})$ has a first zero and multiplying the result with 2π (see equation 32 figure 29):

$$\tau_I = 2\pi \int_0^{t_I} A(\underline{t}) d\underline{t}. \tag{32}$$

In figure 30 the integral time-scale of all clearly time dependent measurements of series $M1$ are plotted versus the reduced Rayleigh number Ra_r. Here, the values of τ_I are normalized by the characteristic time-scale $t_0 = h^2/\kappa$ of the convective flow. At low reduced Rayleigh numbers $Ra_r < 2000$ the integral time scale of MHD flow is larger than the one of OHD flow. When the reduced Rayleigh number exceeds a value of about $Ra_r \approx 4000$ the values at OHD flow achieve a plateau value of $\tau_I \approx 6$, that is maintained up to $Ra_r \approx 4 \cdot 10^4$. Any further increase of the reduced Rayleigh number for OHD flow causes a significant decrease of the integral time-scale which can be related to much faster dynamics of the flow.

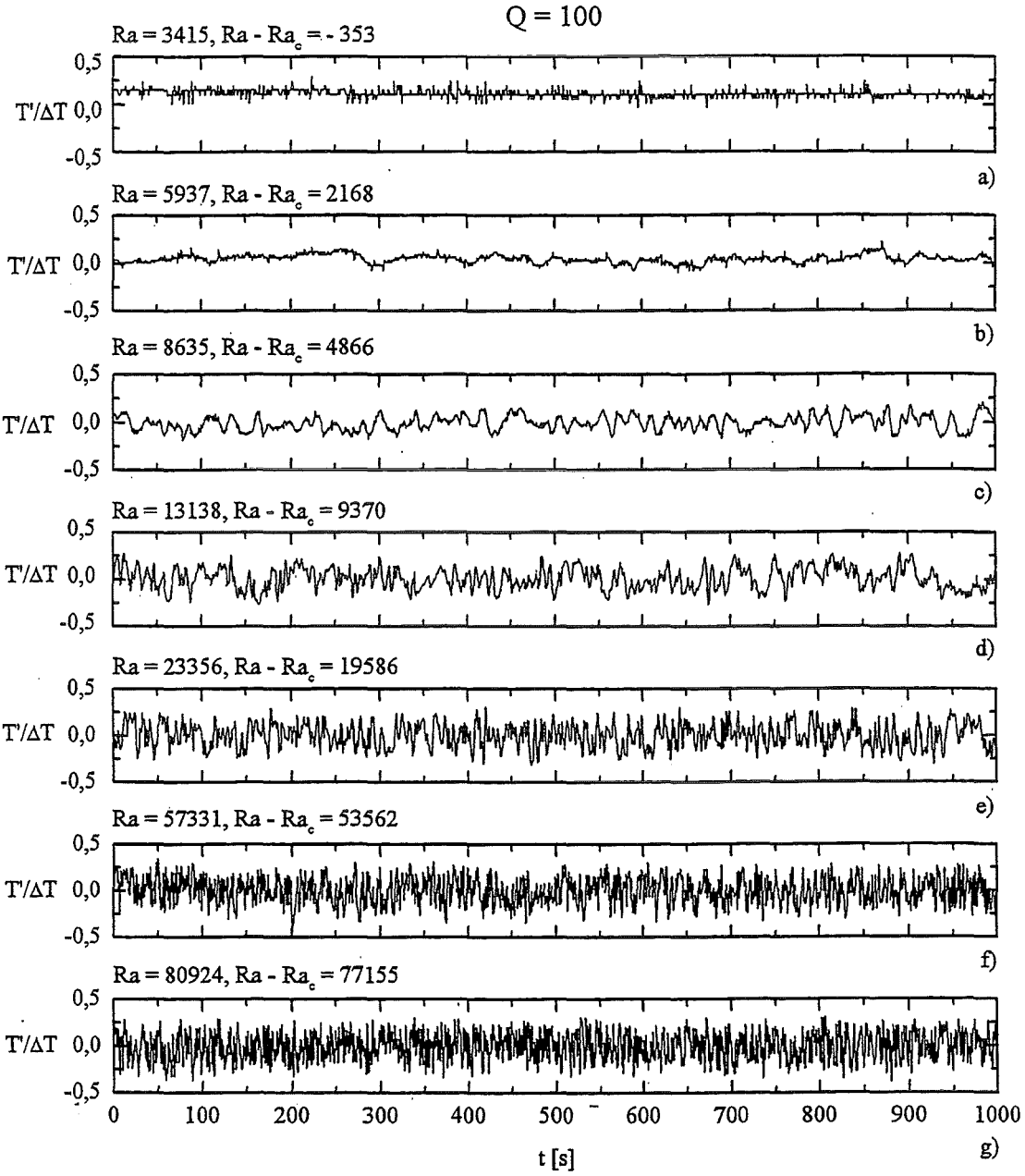

Figure 25: Time series of the fluctuating part of the temperature T' recorded by the probe for magnetohydrodynamic flow at $Q = 100$. The Rayleigh number is increased from the subcritical value $Ra = 3415$ to supercritical values up to $Ra = 80924$. The temperature fluctuations are scaled with the temperature difference across the layer ΔT.

For MHD flow, above $Ra_r \approx 4000$, a continuous decrease of the integral time-scale as Ra_r^{-1} can be observed, that corresponds to significantly faster dynamics compared to OHD flow. By plotting the evaluated time scale versus the reduced Rayleigh number we obtain similar values for all Chandrasekhar numbers investigated. Therefore, we conclude

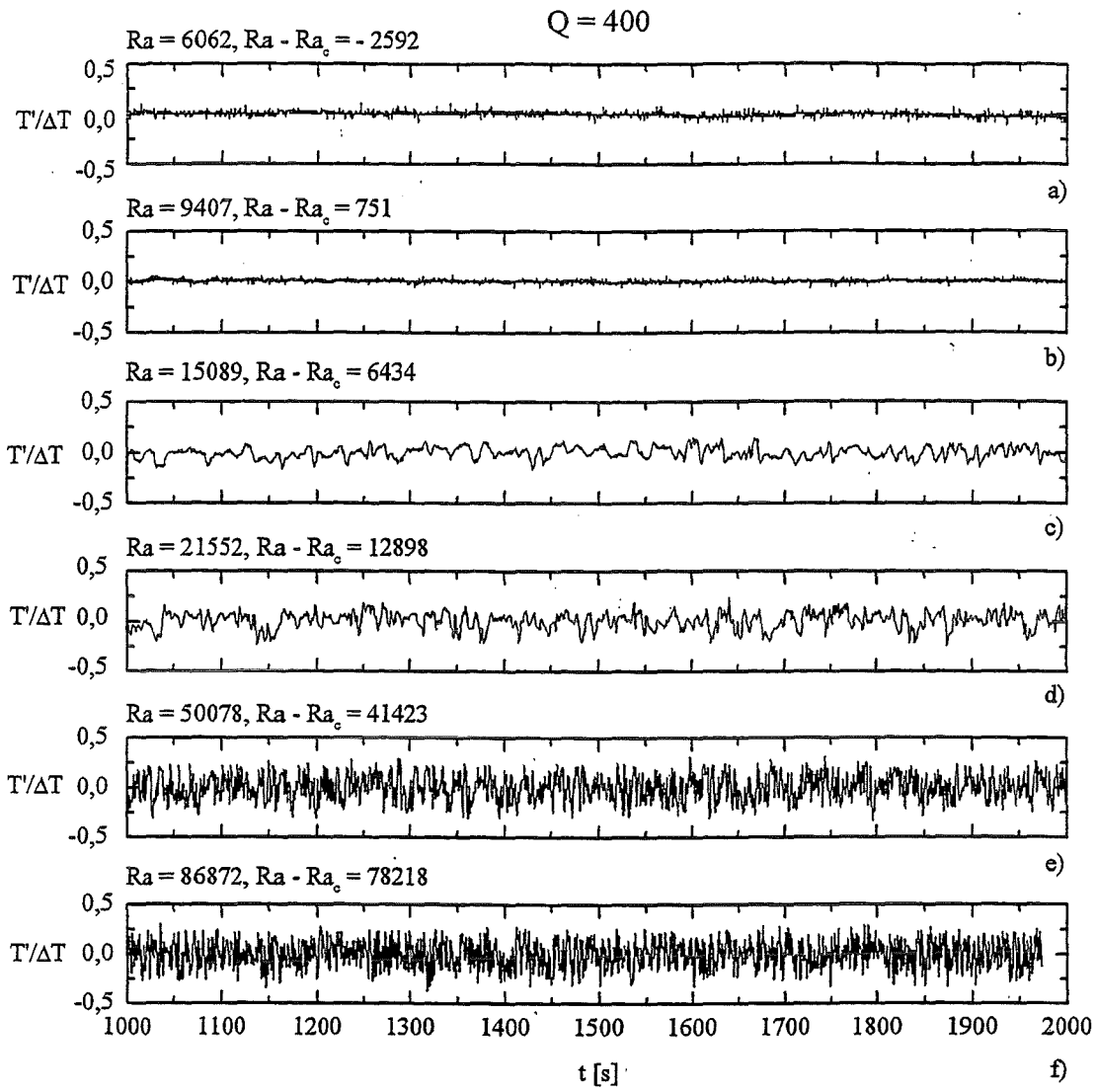

Figure 26: Time series of the fluctuating part of the temperature T' recorded by the probe for magnetohydrodynamic flow at $Q = 400$. The Rayleigh number is increased from the subcritical value $Ra = 6062$ to supercritical values up to $Ra = 86872$. The temperature fluctuations are scaled with the temperature difference across the layer ΔT.

that for MHD flow the dynamics at large supercritical conditions are determined only by the reduced Rayleigh number and not by the Chandrasekhar number.

There is no agreement between the integral time-scale evaluated from this experiment and the time scales evaluated by Clever and Busse (1989) and Busse and Clever (1996) also plotted in figure 30. It has to be mentioned in this context that we used a definition for the integral time scale of the flow which is convenient for the evaluation of time series measurements. Other definitions may lead to different results but the difference between the experimental and the theoretical values are to large as to be closed by some other definition of the integral time scale. In a later work (Busse and Clever (1996)) the same authors evaluated the time scales at higher Chandrasekhar numbers. The results plotted in figure 30 agree better with the time scales obtained in the experiment but only data

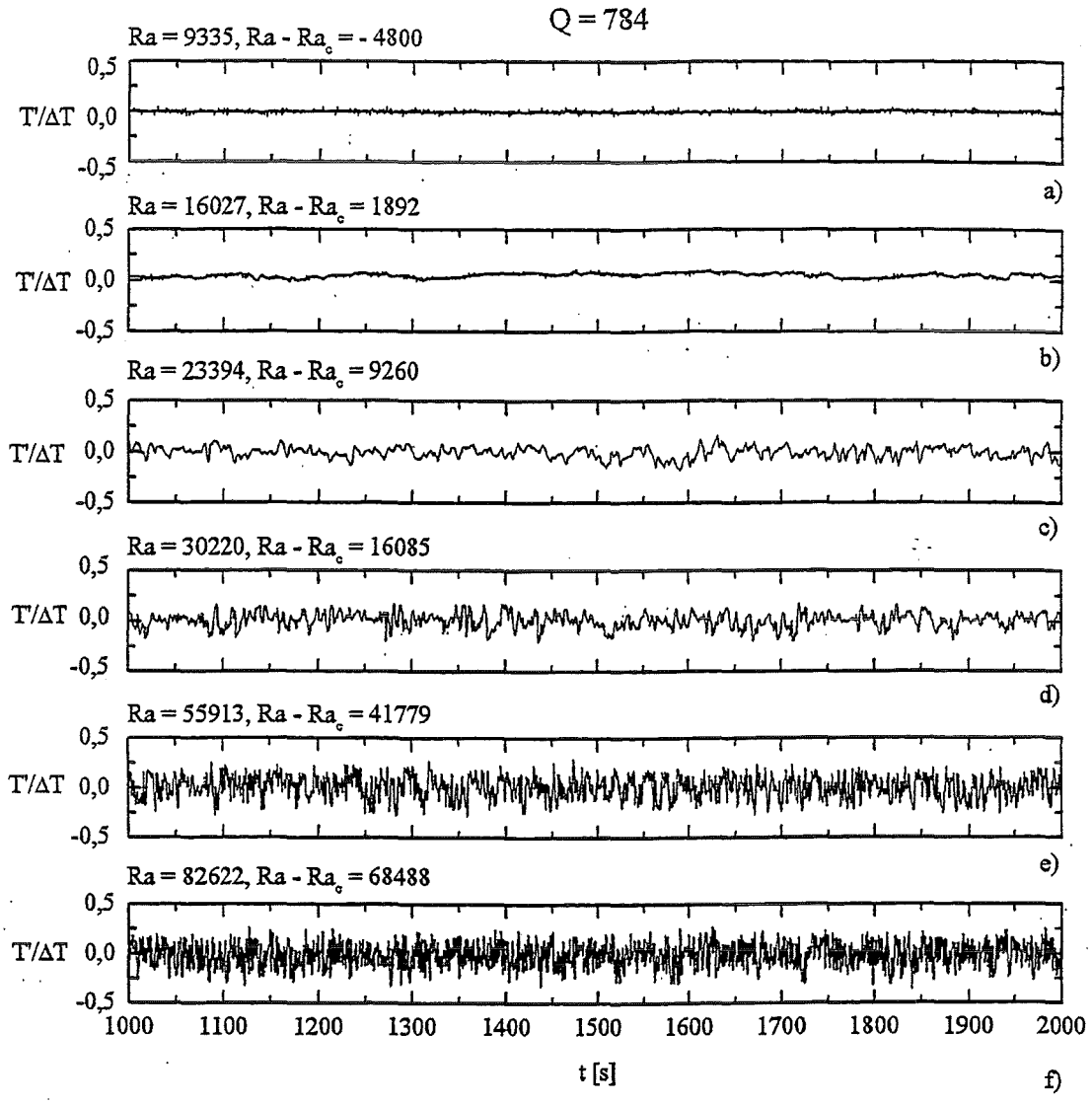

Figure 27: Time series of the fluctuating part of the temperature T' recorded by the probe for magnetohydrodynamic flow at $Q = 7840$. The Rayleigh number is increased from the subcritical value $Ra = 9335$ to supercritical values up to $Ra = 82622$. The temperature fluctuations are scaled with the temperature difference across the layer ΔT.

at small supercritical values are provided by the numerical simulation.

Moreover the numerical data obtained by Busse and Clever (Busse and Clever (1996)) do not follow the trend of those in Clever and Busse (1989).

Spectral distribution of temperature fluctuations: The general damping effect of the magnetic field on time-dependent motions was already outlined in section 4.2.1. It appeared that if such damping is desired, a lower Nusselt number respectively a higher temperature differences has to be accepted. In some applications however this argumentation is too general. Imagine for example a crystal growth process, fluctuations of the flow on long time-scales might cause undesirable disturbances in the crystal structure whereas the additional transport of heat and species by short time-scale fluctuations might be de-

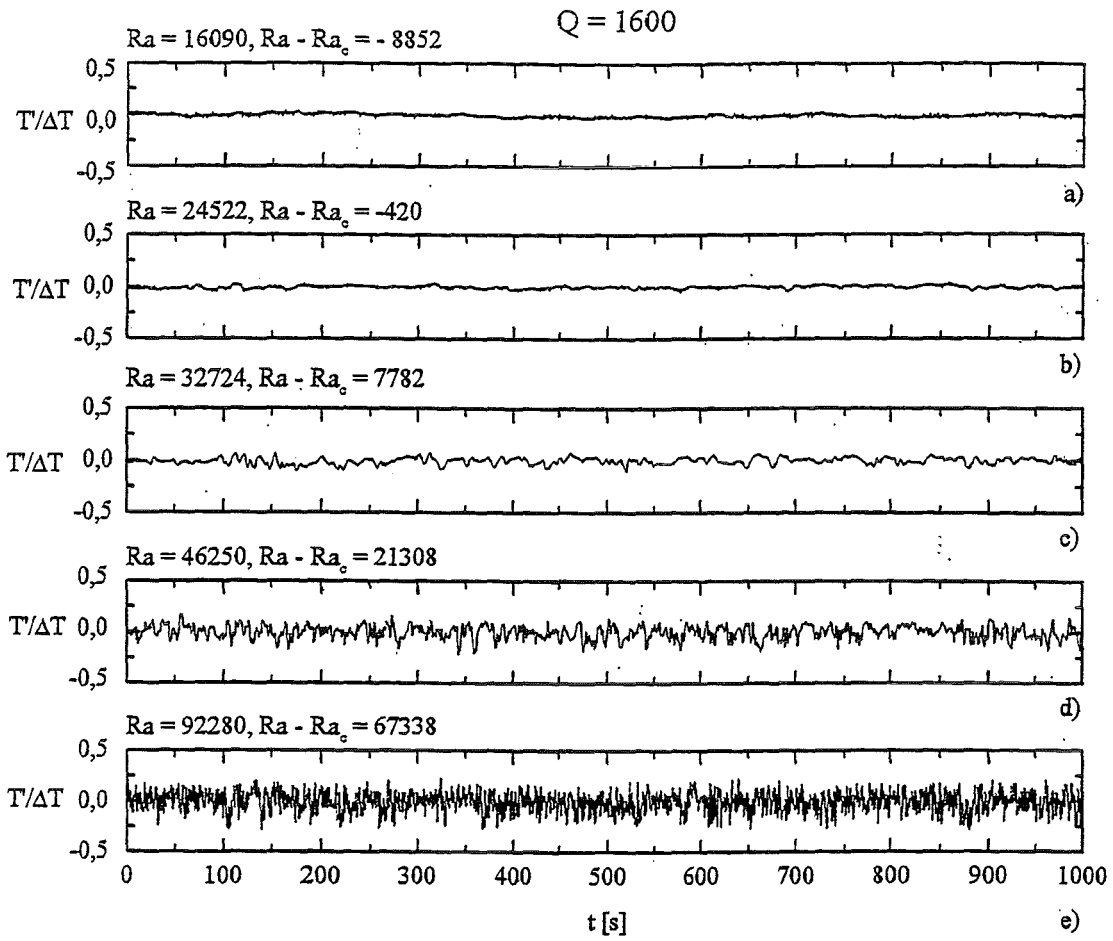

Figure 28: Time series of the fluctuating part of the temperature T' recorded by the probe for magnetohydrodynamic flow at $Q = 1600$. The Rayleigh number is increased from the subcritical value $Ra = 3415$ to supercritical values up to $Ra = 92280$. The temperature fluctuations are scaled with the temperature difference across the layer ΔT.

sired to accelerate the process or to provide homogeneous conditions at the solidification front. Therefore we investigate wether damping by Joule's dissipation at this particular flow problem is selective in respect of frequency and calculate the power spectra (see appendix D.3 for definition) of the temperature signal measured by the probe. In order to lower statistical errors, all power spectra presented below are calculated as an average of 64 successive intervalls taken from the long time-series measurements $M2a$ and $M2b$.

In figure 31 the influence of an increasing magnetic field on the power spectra at a constant Rayleigh number of $Ra = 5 \cdot 10^4$ ($M2a$) is shown. The results are presented in non-dimensional form by scaling temperatures with the temperature difference across the layer ΔT and the non-dimensional frequencies are obtained by using the thermal diffusion time scale to calculate the characteristic scaling frequency $f_0 = \kappa/h^2$ (see section 4.2). The level of noise, also plotted in figure 31, is calculated by scaling the power spectra of noise, as presented in figure 13, with the temperature difference across the layer $\Delta T = 35K$ at this particular Rayleigh number.

Compared with the OHD flow at $Q = 0$ the power spectra of MHD flow at $Q = 400$

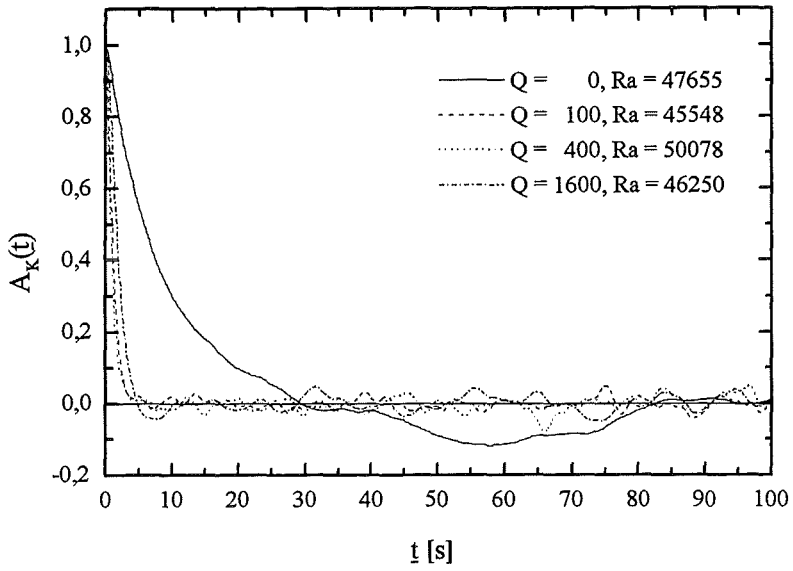

Figure 29: The influence of increasing Chandrasekhar-numbers on the autocorrelation functions of temperature signals recorded by the probe at a Rayleigh-number of $Ra \approx 5 \cdot 10^4$.

show significantly lower values in the low frequency range ($f \lessapprox 1.8$), related to less intense long period fluctuations. Above this frequency the values of MHD flow exceed the ones of OHD flow indicating that short time-scale fluctuations with higher energy can be generated in the presence of external magnetic field.

If the magnetic field is further increased to $Q = 1600$ and higher values, a systematic damping of the fluctuations is observed in the whole frequency range. Although for $Q = 14400$ the layer is supposed to be subcritical according to linear stability theory (see Chandrasekhar (1961)), the power spectra still differs noticeable from the noise. However, these values are orders of magnitude lower than the ones without any or with a week magnetic field. As the Nusselt number approaches unity at this Rayleigh number the layer may be considered as stable from a practical point of view.

In appendix D.3 it is outlined that the total intensity of fluctuations respectively the mean square value may be calculated from the sum of all contributions to the energy spectrum S_n (equation 58). Limiting the summation to a distinct value of n we obtain the contribution of fluctuations at a frequency f_n and frequencies below to the ms-value

$$E_n = \frac{1}{E_{n\to\infty}} \sum_{1}^{n} S_n. \tag{33}$$

Scaling with the overall ms-value $\overline{\Phi'^2} = E_{n\to\infty}$, obtained as n approaches infinity, the values tend to unity when all relevant frequencies of the signal have been taken into account. The functional increase of E_n with frequency is furtheron called the integrated power spectra $E(f)$. In figure 32 integrated power spectra are plotted, evaluated from the power spectra at $Q = 0$, $Q = 400$ and $Q = 1600$ in figure 31. For OHD flow ($Q = 0$) E increases steeply already in the low frequency range. The saturation level, defined as $E \gtrsim 0.98$, is reached for $f \approx 4.5$. Below $f \approx 0.2$ the integrated power spectra of

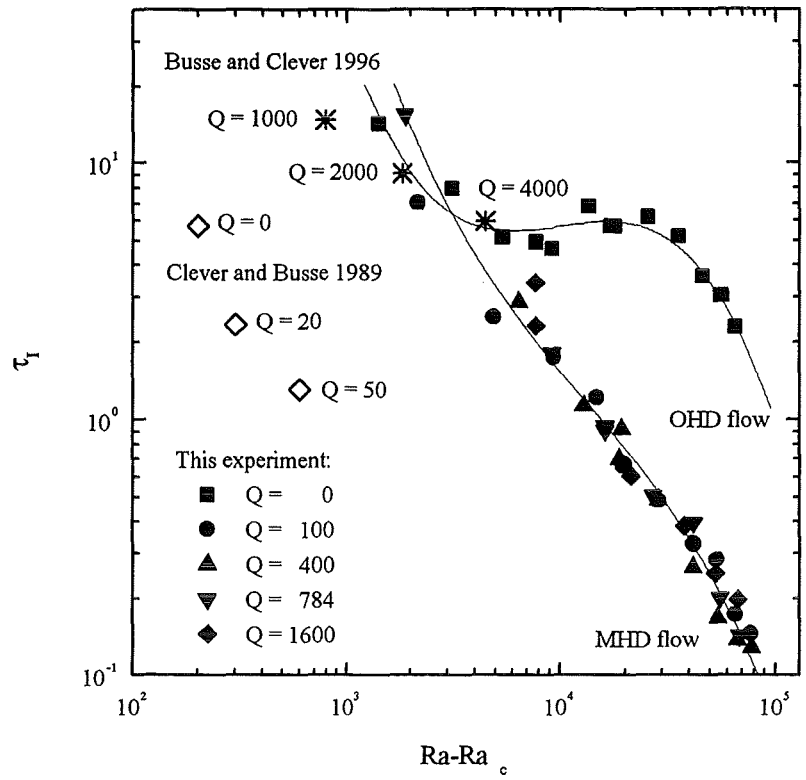

Figure 30: Integral timescales τ_I normalized by the temperature diffusion time-scale $t_0 = h^2/\kappa$. The values represented by solid symbols are obtained from this experiment. The hollow diamonds and stars are values obtained from numerical predictions by Clever and Busse (1989) and Busse and Clever (1996).

both MHD flows are significantly smaller. Thus a much smaller contribution of this low frequency range to the overall intensity becomes obvious. The values of E for $Q = 400$ are increasing steeply at frequencies above $f \approx 1$ and the saturation level at this particular strength of the magnetic field is reached for the noticeably higher frequency $f \approx 14.1$. Thus, the energy containing range of the spectra at MHD flow is shifted to significantly higher frequencies compared with OHD flow. If the magnetic field is further increased to $Q = 1600$ this effect seems to be reversed, because the saturation level is found for $f \approx 6.6$. Nevertheless the delayed increase of the coefficient still indicates greater contribution of higher frequencies to the total energy.

Therefore we conclude that the general damping effect of the magnetic field by Joule's dissipation is selective in respect to frequency. Low frequency fluctuations of the flow are damped more strongly whereas high frequency fluctuations are less damped or may even be enhanced by the magnetic field as it is seen in figure 31 for $Q = 400$.

The dynamics of the convective flow are to some extend characterized by the slopes of the energy spectra in the high frequency range. Therefore the same spectra, as plotted in figure 31 for $Q = 0$, $Q = 400$ and $Q = 1600$, are replotted in figure 33 in separate graphs. Within the range of decay the energy spectra of OHD flow ($Q = 0$) two different regions with distinct slopes are exposed. In the range $1 < f < 10$ the energy decays as $S \sim f^{-2}$, above $f \approx 10$ the spectrum matches a slope of approximately -4. These results

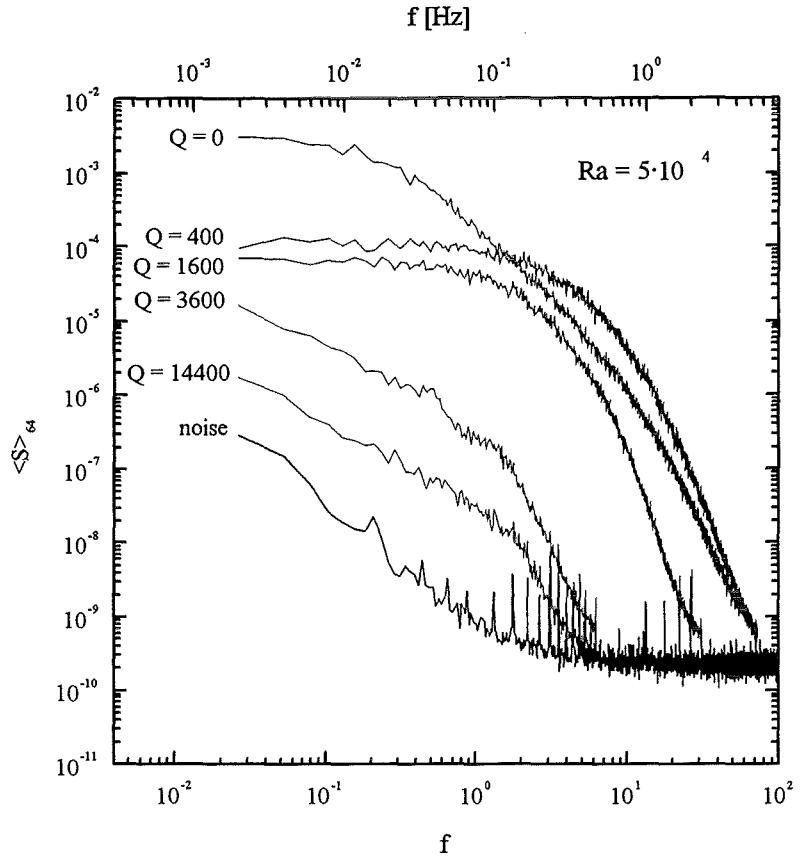

Figure 31: Influence of increasing Chandrasekhar numbers from OHD flow ($Q = 0$) to MHD flow up to $Q = 14400$ on the power spectra $< S >_{64}$ of the temperature signal recorded by the probe in the middplane at a constant Rayleigh number of $Ra = 5 \cdot 10^4$. At Chandrasekhar numbers $Q = 0$, 400, 1600, 3600 and 1400 the Nusselt numbers $Nu = 2.06$, 1.41, 1.07, 0.98 and 0.96 are obtained.

are not consistent with the predictions of the spectral model of Batchelor (1959) which predicts a behavior of $S \sim f^{-17/3}$ for low Prandtl number fluids in the inertial-diffusive sub-range of the thermal energy spectrum. However if we calculate the Reynolds number from $\mathrm{Re} = (Ra/\mathrm{Pr})^{1/2}$ we obtain $\mathrm{Re} \approx 1600$. At this low value, significant energy transfer from the large vortices to eddies of smaller scales can not be expected. There exists no inertial subrange and the temperature fluctuations decay by molecular diffusion only. Hinze (1975) (p.294) outlines that in the case of small convective transport, compared to diffusive, the power spectrum of a passive scalar quantity like temperature S_T scales as

$$S_T(f,t) = H \cdot \kappa^{-3} \cdot S_v(f,t) \cdot f^{-4}, \tag{34}$$

where H is constant and S_v is the energy spectrum of the velocity field. In a non dissipative, purely convective range of the velocity field S_v can be assumed to be constant and the power spectra of the passive scalar quantity decays purely on a diffusion process as $S_T(f,t) \sim f^{-4}$, which is in good agreement with our measurements in the frequency range $f > 10$. Similar findings were reported by Horanyi, Krebs and Müller (1998) from measurements in heated sodium layers. If this argument holds, the less steep decrease of

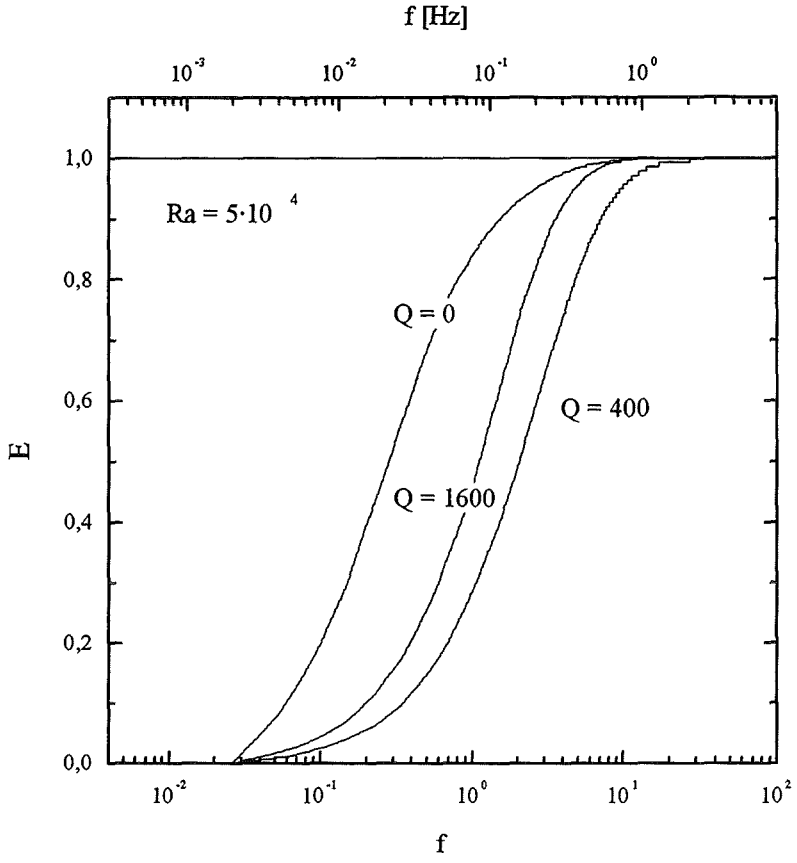

Figure 32: Influence of increasing Chandrasekhar numbers on the integrated power spectra E at constant Rayleigh number $Ra = 5 \cdot 10^4$. These curves are representing the relevance of frequencies below f_n for the over all intensity of temperature fluctuations.

the temperature spectrum in the range $1 < f < 10$ is associated with an increase of the velocity spectrum as f^2, but to confirm this conjecture, additional velocity measurements are necessary.

The power spectra of MHD flows at $Q = 400$ and $Q = 1600$ are plotted in figure 33b. In the frequency range below $f \approx 1$ the Fourier coefficients do not depend on the frequency. In an intermediate frequency range of $1 \lessapprox f \lessapprox 10$, the slopes are decreasing continuously. For $Q = 400$ a constant slope of -5 is obtained above $f \approx 20$. At $Q = 1600$ the decrease is even steeper; above $f \approx 10$ the spectra falls of as f^{-6}. As convective heat transport is even reduced compared to OHD flow equation 34 still holds. The steeper decay of the temperature spectrum is therefore caused by changes in the energy spectrum of the velocity field S_v related to Joules dissipation.

The influence of increasing magnetic fields on the power spectra at a fixed convective heat flux of $q = 3 \cdot 10^5 W/m^2$ is shown in figure 34. The power spectra are evaluated from long time series measurements $M2b$.

At constant heat flux, the temperature difference across the layer is increased by the damping effect of the magnetic field. Therefore the results are plotted here in dimensional form to avoid misleading interpretations from the scaling. However, similar behavior as in case of constant Rayleigh number boundary condition (see figure 31) is observed. Com-

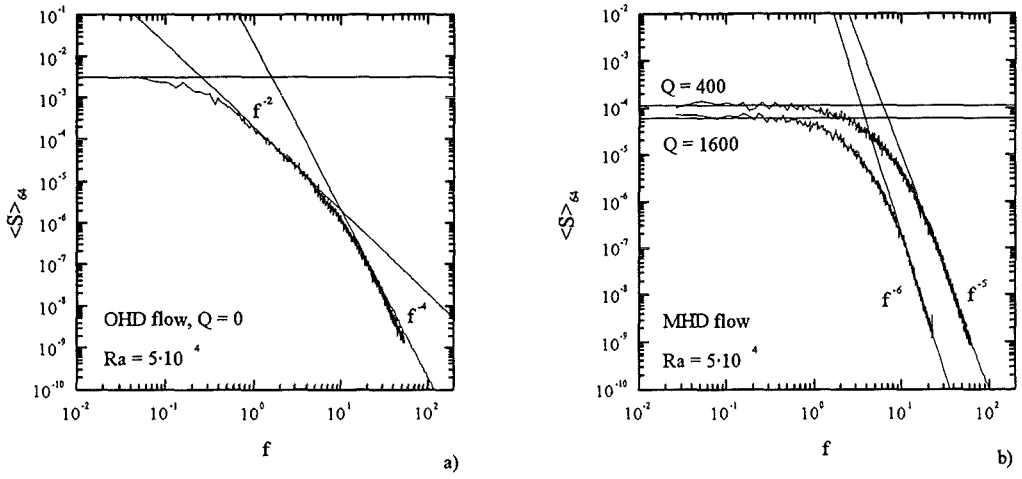

Figure 33: Characteristic slopes in the power spectra of temperature signals recorded by the probe in the midplane at Rayleigh number $Ra = 5.0 \cdot 10^4$. a) hydrodynamic flow ($Q = 0$) and b) MHD flow at $Q = 400$ and $Q = 1600$.

pared to OHD flow the energy spectra of MHD flow are shifted towards higher frequencies and the slopes in the high frequency range are significantly decreased. As we are dealing here with dimensional physical quantities we can conclude that for $Q = 400$ there are much less intense fluctuations at frequencies below $f \approx 1$ compared to the OHD flow. Above this frequency the fluctuations for MHD flow are seen to be significantly stronger. At higher Chandrasekhar numbers the spectral coefficients of MHD flow are all below those of pure hydrodynamic flow and are thus indicating weaker fluctuations in the whole frequency range. Similar to the findings at constant Rayleigh number fluctuations at higher frequencies are more important for the overall energy content of the spectrum than low frequency contributions. This follows clearly from calculating the integrated power spectra from equation 33, as it is shown in figure 35.

4.3 Isotropy characteristics of the time dependent flow

Because of the non-coplanar arrangement of the four thermocouples of the probe (see figure 12) the fluctuating part of the temperature gradient vector $\nabla T'$ can be measured. As $\nabla T'$ is a vector with components in all three spacial directions, the degree of local isotropy of the time dependent flow field can be evaluated. Imagine a two-dimensional flow pattern of time dependent convective rolls which are all aligned in the same direction, e.g. the x-direction. In such a case the flow field and with it the temperature field does not vary in x direction, neither in space nor in time and therefore the mean value $\partial_x \overline{T}$ as well as the fluctuating part $\partial_x T'$ of the temperature gradient in x-direction is zero. Here ∂_x is used to denote the spacial derivative $\partial/\partial x$. However, if the time dependent flow is three-dimensional and has no preferred orientation in the horizontal (x, z)-plane, statistical vector-properties like the ms-value of the temperature gradient become independent of the horizontal direction i.e. $\overline{\partial_x T'^2} = \overline{\partial_z T'^2}$. In such a case the flow field will be called isotropic in respect to the horizontal directions. Furthermore if the intensity of $\nabla T'$ is uniform in all three directions ($\overline{\partial_x T'^2} = \overline{\partial_y T'^2} = \overline{\partial_z T'^2}$) the temperature field and with it

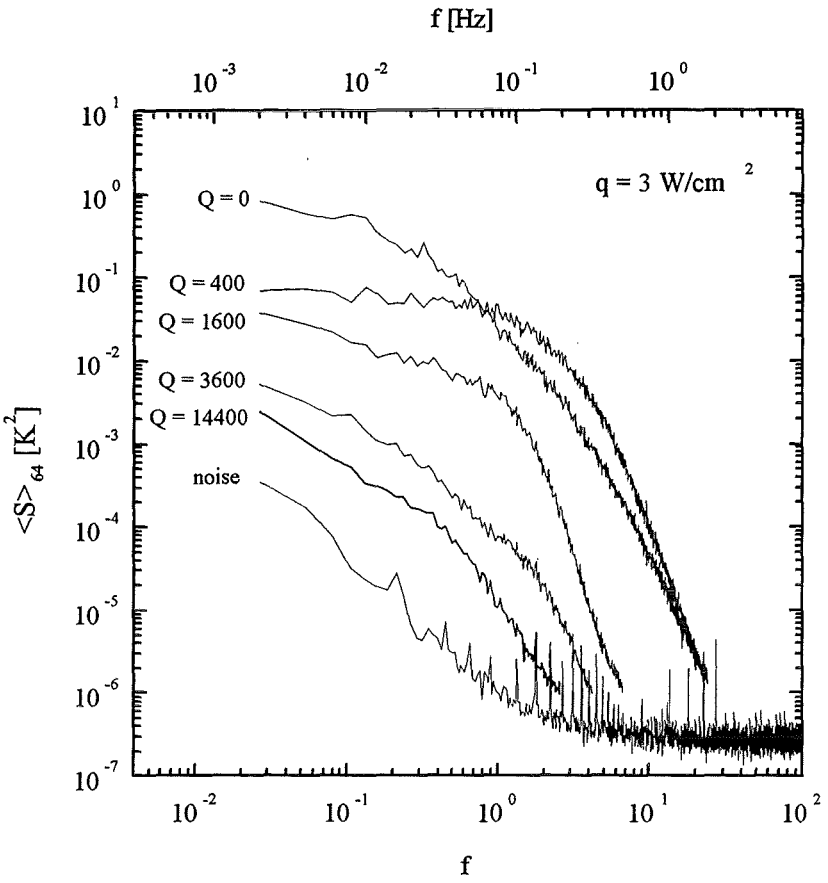

Figure 34: Influence of increasing Chandrasekhar numbers on the power spectra $< S >_{64}$ of the temperature signal recorded by the probe in the middplane at a constant heat flux of $q = 3 \cdot 10^5 W/m^2$. At Chandrasekhar numbers $Q = 0$, 400, 1600, 3600 and 14400 the Nusselt numbers $Nu = 1.67$, 1.20, 1.00, 0.99 and 0.97 respectively the Rayleigh numbers $Ra = 19722$, 27405, 32473, 33158 and 33802 are obtained.

the flow is called isotropic. In order to evaluate the isotropy characteristics of the flow field the isotropy coefficients:

$$A_{yx} = \frac{\overline{\partial_y T'^2}}{\overline{\partial_x T'^2}}, \tag{35}$$

$$A_{yz} = \frac{\overline{\partial_y T'^2}}{\overline{\partial_z T'^2}} \tag{36}$$

and

$$A_{xz} = \frac{\overline{\partial_x T'^2}}{\overline{\partial_z T'^2}} \tag{37}$$

are defined. The two vertical isotropy coefficients A_{yx} and A_{yz} denote the ratio of intensity of fluctuations of the temperature gradient in the vertical y-direction to those in the two horizontal directions (x and z). If both coefficients approach unity ($A_{yx} = A_{yz} = 1$) the time dependent flow field is isotropic. A_{xz} is the horizontal isotropy coefficient respectively the ratio of intensities in the horizontal plane. When A_{xz} becomes unity, the flow is

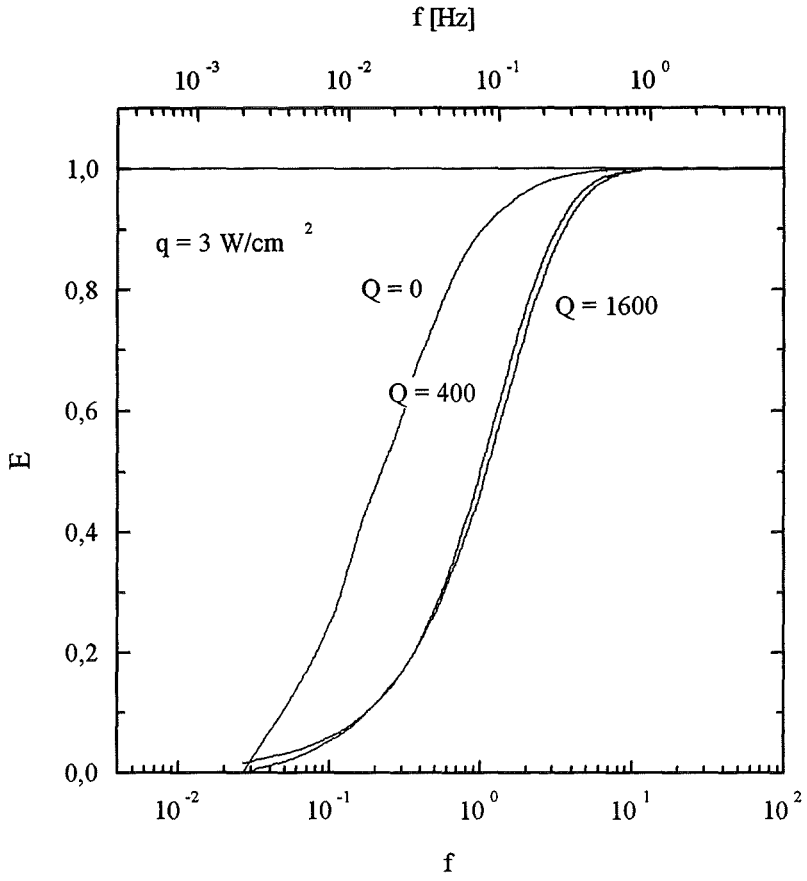

Figure 35: Integrated power spectra E at constant heat flux $q = 3 \cdot 10^5 W/m^2$ at various magnetic fields. The graphs are indicating the relevance of frequencies below f for the power of temperature fluctuations.

isotropic in respect to the horizontal directions. If A_{xz} becomes lower than one, the weaker fluctuations in the x-direction are indicating a predominant orientation of convective structures i.e. roll axis in this particular direction. Larger values than one are associated with a convective flow patter predominantly orientated in z-direction. The limiting cases $A_{xz} \to 0$ and $A_{xz} \to \infty$ are related to purely two-dimensional flow independent of the x- respectively z-direction.

From linear stability theory (see Chandrasekhar (1961)) the horizontal symmetry of Rayleigh-Bénard convection will not be broken by imposing a vertical magnetic field on an infinite liquid metal layer. Thus $A_{xz} \approx 1$ is expected from the measurements of the temperature gradient. Nevertheless, in a finite rectangular box, viscous forces are directing convective rolls parallel to the shorter side at least for marginal supercritical conditions and values $A_{xz} < 1$ are expected in this particular case. At large supercritical conditions viscous forces become less important and we can expect increasing coefficients A_{xz} when the Rayleigh number is increased.

In figure 36 the isotropy coefficients A_{yx}, A_{yz} and A_{xz} for hydrodynamic flow ($Q = 0$) and MHD flow with Chandrasekhar numbers $Q = 400$ and $Q = 1600$, evaluated from the measurements $M1$, are plotted versus the reduced Rayleigh number $Ra_r = Ra - Ra_c$.

For reduced Rayleigh numbers below $Ra_r \lessapprox 2000$ values around unity are found for all three coefficients. In principle this indicates isotropic flow. But, one has to realize that in the absence of real time dependent flow the coefficients are calculated from the intensities related to random noise which if they are more or less of the same magnitude also result in isotropy coefficients around unity. Thus at these marginal supercritical conditions the results are most likely not reliable. In the region $2000 < Ra_r < 2 \cdot 10^4$ the vertical coefficients A_{yx} and A_{yz} are decreasing with the Rayleigh number for both OHD flow and MHD flow. Thus, the intensity of the vertical temperature gradient decreases more strongly than the horizontal intensities. Above $Ra_r \approx 2 \cdot 10^4$ the vertical coefficients are increasing again with Rayleigh number. It is conjectured that this increased isotropy of the flow at higher Rayleigh numbers is caused by small-scale structures that are released from the thermal boundary layers at higher Rayleigh numbers.

At a fixed Rayleigh number both coefficients are clearly decreasing, when the magnetic field is increased. Thus fluctuations of the temperature gradient in the horizontal directions are increased compared to the one in the horizontal direction from the action of the magnetic field. It may be conjectured that this effect is due to the reduced horizontal length-scales at MHD flow, because regions of hot upwards-flow and cold downwards-flow are closer to each other and thus the horizontal gradients are increased and so are also their fluctuating parts.

The results for the horizontal isotropy coefficient A_{xz} show a rather non-systematic behavior. However, the values are generally increasing with the Rayleigh number. This may indicate an increasing predominance of the intensity of the fluctuations in x-direction which may be associated with a convective flow pattern of convective rolls orientated along the z-direction. However all obtained values, for various Chandrasekhar numbers and for OHD flow, are of order one. This indicates horizontal isotropy in the whole range of parameters investigated and these findings demonstrate that the magnetic field does not change the horizontal symmetry of the flow.

The investigation of isotropy properties can be extended to the frequency domain. For this we first calculate the power spectra of the temperature gradient. In figure 37 the influence of increasing the Chandrasekhar number from $Q = 0$ to $Q = 400$ and $Q = 1600$ at a constant Rayleigh number of $Ra = 5.0 \cdot 10^4$ is shown. Again the results are obtained by averaging over 64 time series from the long term record $M2a$. They are assorted according to the three spacial directions x, y and z where x and z are the horizontal directions perpendicular to the magnetic field and y is the vertical direction aligned with gravity and the magnetic field. In the frequency range below $f \approx 1$ the damping of long term fluctuations becomes visible in the power spectra of all three components of the temperature gradient. A simular behaviour is observed already from the power spectra of the temperature signal plotted in figure 31. However, in the vertical direction (figure 37b) the intensities are systematically decreasing with the Chandrasekhar number whereas in the horizontal directions (figure 37a and c) an increase of the magnetic field from $Q = 400$ to $Q = 1600$ does not seem to affect the flow significantly.

In the frequency range above $f \approx 1$ the spectra of the temperature gradients in the two horizontal directions behave similarly to the power spectra of the temperature. Compared to OHD flow ($Q = 0$), the intensity of the temperature gradient at $Q = 400$ exceeds significantly the values obtained for $Q = 0$. In addition, the slope of the spectra in the high frequency range is decreased by the imposition of the magnetic field. At $Q = 1600$ significantly lower intensities are found, but the slope of the spectrum remains

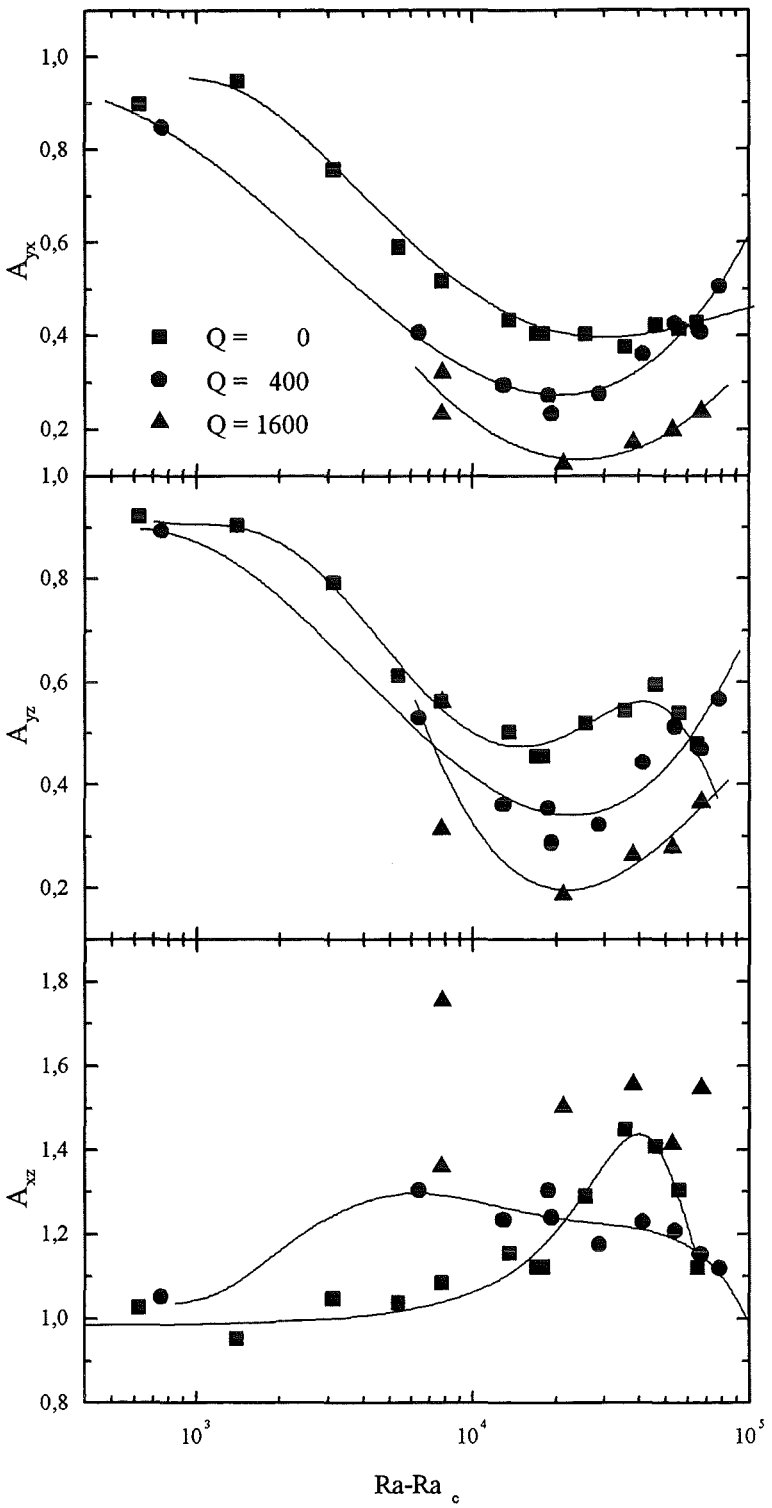

Figure 36: Isotropy coefficients A_{yx}, A_{yz} and A_{xz} evaluated from the fluctuating part of the temperature gradient recorded by the probe. Values for hydrodynamic flow ($Q = 0$) and Chandrasekhar numbers $Q = 400$ and $Q = 1600$ are plotted versus the reduced Rayleigh number $Ra_r = Ra - Ra_c$.

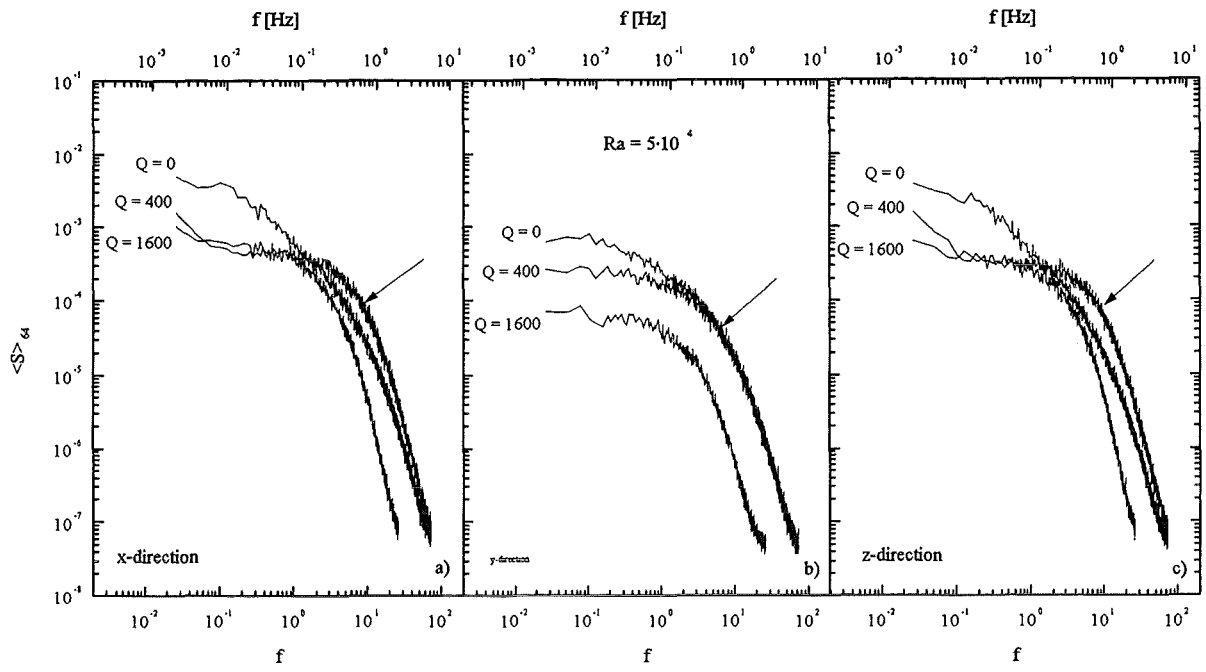

Figure 37: Power spectra of the temperature gradient ∇T recorded by the probe in the midplane. The spectra are asorted acording to the three spacial directions x, y and z where x and z are the horizontal directions, perpendicular to the magnetic flield and y is the vertical direction aligned with gravity and the magnetic field. At a fixed Rayleigh number of $Ra = 5 \cdot 10^4$ the Chandrasekhar number is increased from $Q = 0$ to $Q = 400$ and $Q = 1600$.

unchanged compared to the one with $Q = 400$. Thus, the conjecture of enhanced small scale fluctuations originating from the power spectra of temperature is also supported by the spectra of the horizontal components of the temperature gradient.

The variance with Q of the spectrum of the temperature gradient in vertical direction is different from those in horizontal direction. For $Q = 400$, the intensity in the range above $f \approx 1$ is not affected by the magnetic field. However, as the Chandrasekhar number is further increased to $Q = 1600$, the whole spectrum is shifted to lower intensities. Moreover, the slope in the frequency range above $f \approx 1$ is not affected by the electromagnetic forces.

From this discussion we conclude: The characteristic features of the vertical motion are obviously not affected by the magnetic field in the frequency range $f > 1$. We observe here an overall damping by Joule's dissipation which originates mainly from fluctuations in the horizontal directions. In contrast to this finding the flow structure in the horizontal directions is significantly different what is in agreement with the fact that Lorentz forces act only perpendicular to the magnetic field.

Using the power spectra of the temperature gradient plotted in figure 37 the isotropy coefficients 35, 36 and 37 can be calculated as functional depedencies from the fluctuations frequency. In figure 38 the graphs a and b show the vertical isotropy coefficients A_{yx} and A_{yz} versus frequency; in graph c the horizontal isotropy coefficient A_{xz} is plotted. Both vertical coefficients depend similary on frequency. For OHD flow with $Q = 0$ small values,

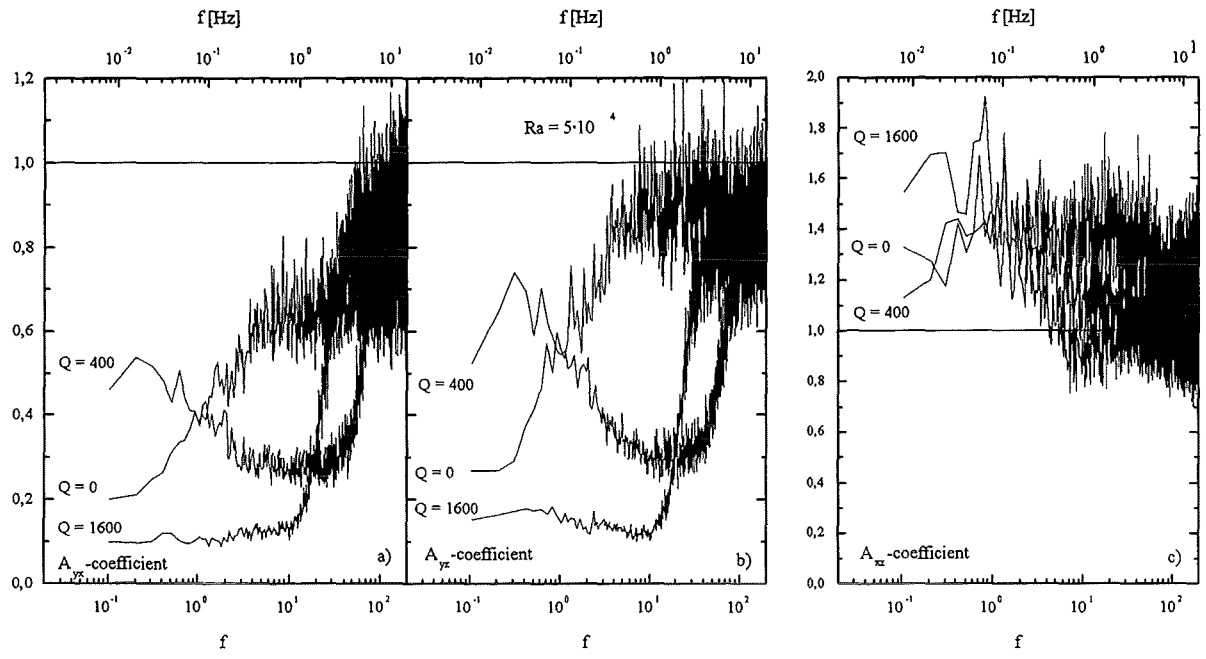

Figure 38: Frequency dependence of isotropy coefficients A_{yx}, A_{yz} and A_{xz}, calculated from the fluctuating part of the temperature gradient measured by the probe. At a fixed Raileigh number of $Ra = 5 \cdot 10^4$ the Chandrasekhar number is increased from $Q = 0$ to $Q = 400$ and $Q = 1600$.

corresponding to lower intensity of the fluctuations in the vertical direction are found at low frequencies. The coefficients are systematically increasing with frequency and reach above $f \approx 10$ a saturation level of approximately unity. Thus a continuous increase of vertical isotropy is indicated by the probe signals. If we try to put this observation into a picture of the spacial structures, we can imagine an isotropic velocity field of small vortices embedded in a large scale non-isotropic time dependent flow. The small structures are created by the buoyant release of lumps of hot fluid from the thermal boundary layers at the lower wall respectively cold fluid from the boundary layer at the upper wall.

It has to be mentioned, that when the effect of noise increases in the power spectra, as it is the case at higher frequencies, the isotropy coefficients tend towards unity and give the impression of isotropic flow. As this effect exhibits the same tendency as the findings in the experiments related to flow phenomena one has to be careful up to what frequency the results are reliable in the sense that they contain information on the flow field.

For the MHD flow at $Q = 400$ the vertical isotropy coefficients are decreasing with frequency until for $f \approx 20$ a minimum is reached. Above this frequency the coefficients increases steeply into the noise dominated region. Thus compared to OHD flow the temperature field is more isotropic at frequencies $f < 1$ whereas above this frequency much lower isotropy is found. The further increase of the Chandrasekhar number to $Q = 1600$ leads to significantly lower vertical isotropy and below $f \approx 10$ the degree of isotropy is almost independent from the frequency. Beyond this point the values increase strongly into the noise dominated region.

From these results it can be conluded, that the convective flow at MHD conditions

is dominated by long term non-isotropic time-dependent motions. Compared with OHD flow there is a lack of short time-scale fluctuations with a high degree of isotropy.

In figure 38c the horizontal isotropy coefficient A_{xz} is plotted versus frequency. Here horizontal symmetry of the flow problem ensures, that whatever the impact of the velocity field on the temperature field is, it is the same in both horizontal directions. Thus a preferred orientation of the time dependent structures related to a distinct frequency may be concluded directly from the obtained value of the coefficient.

At frequencies below $f \approx 10$ values of the horizontal isotropy coefficient larger than one are obtained. They are caused by time dependent convective structures that are preferably orientated along the x-direction. In the frequency range above, horizontal isotropy is indicated by coefficients of approximately one. After all A_{xz} differs only little from the value 1 within the whole frequency range and we can conclude that high degree of horizontal isotropy of the time dependent flow structures exists for all time-scales.

In order to obtain further information about the flow pattern from the vertical isotropy coefficients additional information about the impact of the velocity field on the temperature field and the temperature gradient is required. Nevertheless we have seen from these results, that it is possible to derive some deterministic information on the spacial structure of the flow using a single point measurement of a multipole-temperature probe.

5 Conclusions

This report presents an experimental study of the influence of a vertical magnetic field on liquid metal Rayleigh-Bénard convection. The test section is an electrically heated rectangular box of large aspect ratio 20 : 10 : 1. The emphasis here is put on large heat fluxes as they occur in technical applications such as fusion blankets or material processes. The two mayor control parameters of the flow are the Rayleigh number Ra which expresses in non-dimensional form the temperature difference across the layer and the Chandrasekhar number Q which denotes the magnitude of the applied magnetic field. In this experiment the range of parameters $0 < Ra < 10^5$ and $0 < Q < 14400$ is covered. The physical properties, in respect to natural convection phenomena of the test fluid sodium potassium $Na^{22}K^{78}$ are given by the Prandtl number Pr. In the temperature range, where the experiments are performed, NaK has a very small Prandtl number ($0.017 < \mathrm{Pr} < 0.021$) and therefore nonlinear inertial forces are important in the momentum balance of the flow.

The time averaged temperatures at the upper and the lower boundary are measured by five thermocouples within each wall. From the measured temperature difference across the layer and the known heat flux, the integral heat transfer is characterized by calculating the Nusselt number Nu.

Local, time dependent temperature signals are recorded using a four-element temperature probe placed in the center of the liquid metal layer. The non-coplanar arrangement of the thermocouples enables the evaluation of the local time-dependent temperature gradient which allows to estimate the local isotropy properties of the time dependent flow.

The heat transport through the liquid-metal layer is determined as a function of the measured temperature difference across the layer and the applied magnetic field. The results are pressented in non-dimensional form by the Nusselt number as a function of Rayleigh and Chandrasekhar number. At a constant Rayleigh number the Nusselt num-

bers are decreasing monotonously with increasing Chandrasekhar numbers. Accordingly the Nusselt number decreases at a fixed heat flux under the influence of an increasing magnetic field even though the Rayleigh number in this case is also increased. For pure hydrodynamic flow, reasonable agreement with known experimental and numerical results obtained in mercury with a comparable Prandtl number of $\mathrm{Pr} \approx 0.025$ is found.

From the mean-square values of the temperature fluctuations recorded by the probe, the critical Rayleigh number for the onset of time-dependent convection Ra_t is evaluated. Compared with the critical Rayleigh number Ra_c for the onset of stable convection we find only narrow regimes of stable convection and thus convective heat transport respectively $Nu > 1$ is practically always coupled with time dependent flow. Above the onset of convection the ms-values of the temperature fluctuations are increasing strongly with the Rayleigh number towards a saturation level which seems to decrease with Chandrasekhar numbers. Generally for a fixed Rayleigh number as well as for a fixed heat flux the intensity of fluctuations decreases with increasing magnetic field intensity.

For OHD flow the convective motion below $Ra \approx 10^4$ is dominated by long term fluctuations. Above this value of the Rayleigh number, additional fluctuations on significantly shorter time-scales occur. At MHD flow the governing time-scale of fluctuations gets shorter from increasing Rayleigh numbers.

In the range of investigated parameters, the integral time-scale of MHD flow decreases continuously with Rayleigh number and scales with the reduced Rayleigh number $Ra_r = Ra - Ra_c$. At OHD flow significantly longer integral time-scales are found which below $Ra \approx 4 \cdot 10^4$ are almost constant, but above this value decrease significantly with Rayleigh number. The energy spectra of temperature fluctuations show, that the damping of fluctuations is selective in respect to frequency. Long term fluctuations are damped more strongly, whereas short time-scale fluctuations are less damped and contribute more to the overall intensity of the temperature fluctuations. From the impact of the magnetic field on the velocity fluctuations the slope of the temperature spectra in the high frequency range is decreased with increasing magnetic field.

From the fluctuating part of the temperature gradient within the fluid, the horizontal isotropy coefficient is evaluated for all magnetic fields. No predominant orientation of time dependent flow structures exists. In the vertical direction the fluctuations are strongly non isotropic i.e. the fluctuating part of the temperature derivative in the vertical direction is much weaker than the ones in the horizontal directions. Vertical isotropy decreases with the intensity of the applied magnetic field. From the energy spectra of the temperature gradient it is concluded that the magnetic field changes only the convective motion of the fluid in the horizontal directions. The velocity field in the vertical direction remains qualitatively unchanged i.e. the slopes of the power spectra in the high-frequency range is not changed by the magnetic field. Higher isotropy of short time-scale fluctuations is observed.

The mayor practical benefit that can be taken from the use of magnetic fields e.g. in material processing is the damping of time dependent motions. Utilizing this feature of MHD flow homogeneous conditions can be maintained for example during a solidification process. The magnetic field required for a complete suppression of any motion in this special case of a magnetic field orientated parallel to the acceleration of gravity is relatively weak and may be realized easily in technical facilities.

However, for each individual case of application it has to be taken into account if the decrease of heat transfer that arises from the lack of convective motions can be accepted.

References

Barleon, L., Mack, K.-J. and Stieglitz, R.: 1996, The MEKKA-facility a flexible tool to investigate MHD-flow phenomena, *Wissenschaftlicher Bericht FZKA 5821*, Forschungszentrum Karlsruhe.

Batchelor, G. K.: 1959, Small-scale variation of convected quantities like temperature in turbulent fluid, *J. Fluid Mech.* **5**, 113–139.

Bunk, M. and Wörner, M.: 1998, Direckte numerische Simulation turbulenter Raileigh-Bénard-Konvektion in Quecksilber, *Wissenschaftlicher Bericht FZKA 5915*, Forschungszentrum Karlsruhe.

Burr, U.: 1998, Turbulente Transportvorgänge in magnetohydrodynamischen Kanalströmungen, *Wissenschaftlicher Bericht FZKA 6038*, Forschungszentrum Karlsruhe.

Burr, U. and Müller, U.: 1997, Der Einfluß magnetischer Felder auf eine von unten beheizte Schicht aus elektrisch leitender Flüssigkeit, *Wissenschaftlicher Bericht FZKA 5965*, Forschungszentrum Karlsruhe.

Busse, F.: 1978, Non-linear properties of thermal convection, *Rep. Prog. Phys.* **41**, 1929–1967.

Busse, F. and Clever, R.: 1982, Stability of convection rolls in the presence of a vertical magnetic fiel, *Phys. Fluids* **25(6)**, 931–935.

Busse, F. and Clever, R.: 1996, Three-dimensional convections in the presence of strong vertical magnetic field, *European Journal of Mechanics - Fluid Series* **15(1)**, 1–15.

Chandrasekhar, S.: 1961, *Hydrodynamic and Hydromagnetic Stability*, Dover Publications, Inc. New York.

Chu, T. and Goldstein, R.: 1973, Turbulent convection in a horizontal layer of water, *J. Fluid Mech.* **60**, 141–159.

Clever, R. and Busse, F.: 1974, Transition to time dependent convection, *J. Fluid Mech.* **65**, 625–645.

Clever, R. and Busse, F.: 1989, Nonlinear oscillatory convection in the presence of a vertical magnetic field, *J. Fluid Mech.* **201**, 507–523.

Foust, O.: 1972, *Sodium-NaK Engineering Handbook*, Vol. 1, Gordon and Breach SCIENCE Publishers; ISBN 0677030204.

Giancarli, L., Severy, Y., Baraer, L., Leroy, P., Mercier, J., Proust, E. and Quintric-Bossy, J.: 1992, Water-cooled lithium-lead blanket design studies for DEMO reactor: Definition and recent developments of the box-shaped concept, *Fusion Technology* **21**, 2081–2088.

Gieck, K.: 1981, *Technische Formelsammlung*, Gieck Verlag Heilbronn/N.

Hinze, J. O.: 1975, *Turbulence*, McGraw-Hill, Inc.

Horanyi, S., Krebs, L. and Müller, U.: 1998, Turbulent Rayleigh-Bénard Convection in low Prandtl-number fluids, *Wissenschaftlicher Bericht FZKA 6010*, Forschungszentrum Karlsruhe.

Kek, V.: 1989, Bénardkonvektion in flüssigen Natriumschichten, *Bericht KfK 4611*, Kernforschungszentrum Karlsruhe.

Krishnamurti, R.: 1973, Some further studies on the transition to turbulent convection, *J. Fluid Mech.* **60**, 285–303.

Lyon, N.: 1952, *Liquid metals handbook*, Navexos P-733; Second edition.

Nakagawa, Y.: 1955, An experiment on the inhibition of thermal convection by a magnetic field, *Nature, London* **175**, 417–419.

Nakagawa, Y.: 1956, Experiments on the inhibition of thermal convection by a magnetic field, *J. Sci. Earth* **4**, 108–113.

Nakagawa, Y.: 1959, Experiments on the stability of a layer of mercury heated from below and subject to the simultaneous action of a magnetic field and rotation, *Proc. Roy Soc (London) A* **249**, 138–145.

O'Donnel, J. O., Papanicolaou, P. G. and Reed, C. B.: 1989, The thermophysical and transport properties of eutectic NaK near room temperature, *Technical report*, ANL/FPP/TM-237.

Pellew, A. and Southwell, R.: 1940, On maintained convective motion in a fluid heated from below, *Proc. R. Soc. (London)* **A176**, 312–343.

Reid, W. and Harris, D.: 1958, Some further results on the Bénard problem, *Phys. Fluids* **1**, 102–110.

Rossby, H.: 1969, A study of Bénard convection with and without rotation, *J. Fluid Mech.* **36**, 309–335.

Threlfall, D.: 1975, Free convection in low-temperature gaseous helium, *J. Fluid Mech.* **67**, 17–28.

A Thermophysical data

A.1 Eutectic sodium-potassium alloy $Na^{22}K^{78}$

Temperature dependent thermophysical properties of sodium-potassium $Na^{22}K^{78}$ are obtained from Lyon (1952), O'Donnel, Papanicolaou and Reed (1989), and Foust (1972). The values are fitted by polynominal regression leading to the equations below for:

density

$$\rho(T) = 873.35 - 0.258 \cdot T \quad [kg/m^3]\,; \quad 0°C < T < 204°C \tag{38}$$

kinematic viscosity

$$\nu(T) = 0.89994 - 0.00328 \cdot T + 4.88 \cdot 10^{-6} \cdot T^2 \quad [10^{-6} m^2/s]\,; \quad 0°C < T < 300°C \tag{39}$$

thermal conductivity

$$\lambda(T) = 21.38 + 0.0208 \cdot T - 2.207 \cdot 10^{-5} \cdot T^2 \quad [W/mK]\,; \quad 0°C < T < 400°C \tag{40}$$

specific heat

$$c_p(T) = 990.7 - 0.5133 \cdot T + 5.37 \cdot 10^{-4} \cdot T^2 \quad [J/kgK]\,; \quad 0°C < T < 450°C \tag{41}$$

electrical conductivity

$$\sigma(T) = 2.976 \cdot 10^6 - 5.05 \cdot 10^3 \cdot T + 7.188 \cdot T^2 \quad [10^6 1/\Omega m]\,; \quad 0°C < T < 400°C. \tag{42}$$

B Calculation of temperature gradient ∇T

In figure 39 the sensing tip of the probe consisting of four thermocouples is sketched. The probe coordinate system is parallel to the coordinate system of the test section in

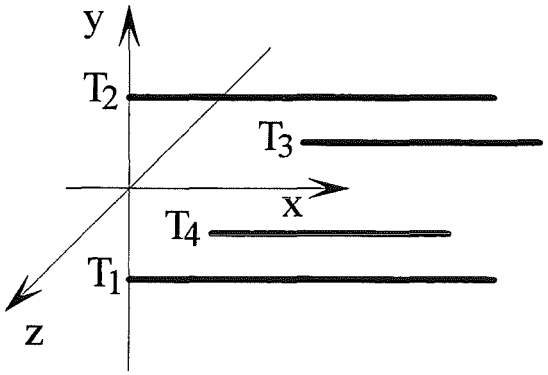

Figure 39: Arrangement of the thermocouples at the sensing tip of the four thermocouples temperature probe. $T_1$and T_2 are laying in the x, y-plane, T_3 and T_4 in the x, z-plane.

figure 10. Before the probe was inserted into the test section, the exact coordinates of the measurement positions x_i, y_i, z_i of the thermocouples T_i have been determined by a

	$x_i[mm]$	$y_i[mm]$	$z_i[mm]$
T_1	0.102	−1.000	0.000
T_2	0.000	1.000	0.000
T_3	1.217	0.000	−1.000
T_4	1.315	−1.000	1.000

Table 3: Coordinates of the probe thermocouples

microscope to an accuracy of $0.001mm$. After glueing the thermocouples into the shaft, their axial position can no longer be adjusted. This leads to small deviations of the values summarized in table 3 from the rated values given in figure 12.

If the temperatures T_{1-4} are all known from a simultaneous measurement, the components of the local temperature gradient $\nabla T = (\partial_x T, \partial_y T, \partial_z T)$ are approximated by finite differences between the thermocouples as:

$$\partial_x T = \frac{T_3 + T_4 - T_1 - T_2}{x_3 + x_4 - x_1 - x_2}, \tag{43}$$

$$\partial_y T = \frac{T_2 - T_1}{y_2 - y_1}, \tag{44}$$

and

$$\partial_z T = \frac{T_3 - T_4}{z_3 - z_4}. \tag{45}$$

C Standard polynomes for thermo-potentials

The temperature $T[°C]$ is calculated from the thermo-voltage $U[V]$ measured in reference to an ice point of exactly $0°C$ using the polynomes below.

For $Cu - CuNi$ thermopairing:

$$T = 0.3705 + 25269.6 \cdot U - 511600 \cdot U^2 + 1.14 \cdot 10^7 \cdot U^3 \tag{46}$$

For $Ni - CrNi$ thermopairing:

$$T = 0.0989 + 25092.6 \cdot U - 273900 \cdot U^2 + 2.67 \cdot 10^7 \cdot U^3 \tag{47}$$

D Statistical properties of time dependent data

Generally any flow quantity is an arbitrary function of space (x, y, z) and time t, so the temporal behavior of a flow quantity Φ at a fixed position may not be described by simple mathematical functions. Thus temporal characteristics of a signal, obtained from a measurement, have to be described by statistic properties. The definitions below are limited to fully developed (non-transient) conditions where no evaluated quantity depends on the moment of its measurement.

It is convenient to split up the present value of a flow quantity $\Phi(t)$ into its temporal mean value $\overline{\Phi}$ denoted by an overbar and its fluctuating part $\Phi'(t)$ denoted by a prime:

$$\Phi(x, y, z, t) = \overline{\Phi(x, y, z)} + \Phi'(x, y, z, t), \tag{48}$$

where the temporal mean value in the time period τ is defined by

$$\overline{\Phi(x,y,z)} = \frac{1}{\tau}\int_0^\tau \Phi(x,y,z,t)\ dt. \tag{49}$$

The time period τ has to be chosen such long that the mean value becomes independent from any further increase of it. With this definition, the mean value of the fluctuating part is always zero:

$$\overline{\Phi'} = 0. \tag{50}$$

D.1 Correlations

The temporal mean values of products of fluctuating parts

$$Q = \overline{\Phi'_1\Phi'_2.....\Phi'_n} = \frac{1}{\tau}\int_0^\tau \Phi'_1 \cdot \Phi'_1 \cdot .... \cdot \Phi'_n\, dt \tag{51}$$

are called correlations. If they are calculated from two ore more identical signals

$$\overline{\Phi'^{\,n}} = \frac{1}{\tau}\int_0^\tau \Phi'^{\,n}\, dt, \tag{52}$$

one obtains the n-th order moments of Φ'.

At $n = 2$ we obtain the mean-square (ms-) value

$$s^2 = \overline{\Phi'^{\,2}}, \tag{53}$$

its square root

$$s = \sqrt{\overline{\Phi'^{\,2}}} \tag{54}$$

is the root-mean-square (rms-) value.

Correlations, normalized by the rms-values

$$K = \frac{\overline{\Phi'_1\Phi'_2.....\Phi'_n}}{\sqrt{\overline{\Phi'^{\,2}_1}} \cdot \sqrt{\overline{\Phi'^{\,2}_1}} \cdot ..... \cdot \sqrt{\overline{\Phi'^{\,2}_n}}}. \tag{55}$$

are called correlation coefficients. They become one for identical signals and zero for statistically independent signals.

D.2 Correlation functions

Any correlation or correlation coefficient may be expressed as a dependency from one ore more parameters e.g. space or time what results in so called correlation functions.

Thus the autocorrelation function is obtained from the correlation coefficient of a time dependent signal with the identical signal at varying time shift $\underline{t}$:

$$A_K(\underline{t}) = \frac{1}{\tau\overline{\Phi'^2}}\int_0^\tau \Phi'(t) \cdot \Phi'(t+\underline{t})dt. \tag{56}$$

D.3 Power spectra

Any time series $\Phi(t)$ that is known in the time period τ can be expressed by a Fourier series:

$$\Phi(t) = \frac{a_0}{2} + \sum_{n=1}^{\infty} A_n \, sin(\omega_n t + \varphi_n) \tag{57}$$

$$A_n = \sqrt{a_n^2 + b_n^2}, \quad tan\,\varphi_n = \frac{a_n}{b_n}, \quad \omega_n = \frac{2\pi \cdot n}{\tau}$$

$$a_n = \frac{2}{\tau} \int_0^{\tau} \phi(t)\, cos(\omega_n\, t)\, dt, \quad n = 0, 1, 2, ...$$

$$b_n = \frac{2}{\tau} \int_0^{\tau} \phi(t)\, sin(\omega_n\, t)\, dt, \quad n = 0, 1, 2, ...$$

Introducing equation 57 in the definition of the ms-value (equation 53) one obtains for $\tau \rightarrow \infty$:

$$\overline{\Phi'^2} = \frac{1}{2} \sum_{n=1}^{\infty} A_n^2 = \sum_{n=1}^{\infty} S_n. \tag{58}$$

The discrete elements S_n are indicating the contribution of fluctuations of the discrete frequency

$$f_n = \frac{\omega_n}{2\pi} = \frac{n}{\tau} \tag{59}$$

to the ms-value. Their functional dependance from f_n is called the power spectra S of the function $\Phi(t)$.

In order to lower the statistic error, the elements of the power spectra S_n can be calculated as an average of M values obtained from M different time series:

$$< S_n >_M = \frac{1}{M} \sum_{i=1}^{M} S_{n,i}. \tag{60}$$

The average value $< S_n >_M$ is denoted by brackets, $S_{n,i}$ is the value of S_n obtained in the i-th time period. The functional dependance from f_n is denoted by $< S >_M$.

D.4 Statistical averaging of data

Suppose a time dependent signal $\Phi(t)$, known in the time period τ, consists of a true part caused by some physical effect $\Phi_r(t)$ we are interested in and a part caused by some random disturbances $\Phi_s(t)$:

$$\Phi(t) = \Phi_r(t) + \Phi_s(t) \tag{61}$$

All three functions can be expressed by Fourier series (equation 57):

$$\Phi(t) = \sum_{n=1}^{\infty} A_n \, sin(\omega_n t + \varphi_n) \tag{62}$$

$$\Phi_r(t) = \sum_{n=1}^{\infty} A_{n,r} \, sin(\omega_n t + \varphi_{n,r}) \tag{63}$$

$$\Phi_s(t) = \sum_{n=1}^{\infty} A_{n,s}\, sin(\omega_n t + \varphi_{n,s}) \tag{64}$$

where the phase of $\Phi_r(t)$ can be defined as zero ($\varphi_{n,r} = 0$) for any angular velocity ω_n. Introducing equations 62 - 64 to 61 and calculating the ms-values (equation 53) of each side we obtain for the Fourier coefficients:

$$A_n^2 = A_{n,r}^2 + A_{n,s}^2 + 2 \cdot A_{n,r} \cdot A_{n,s} \cdot \cos(\varphi_{n,s})$$

If we consider an infinite number of time series ($M >> 1$) the following conditions hold:

- The probability distributions of $A_{n,r}$, $A_{n,s}$ and $\varphi_{n,s}$ are independent from each other.
- $\varphi_{n,s}$ is even distributed:

$$\rho(\varphi_{n,s}) = \frac{1}{2\pi}; 0 \leq \varphi_{n,s} \leq 2\pi$$

And we obtain after averaging over an infinite number of time series:

$$< A_n^2 >=< A_{n,r}^2 > + < A_{n,s}^2 > +2 \cdot \underbrace{< A_{n,r} \cdot A_{n,s} \cdot \cos(\varphi_{n,s}) >}_{=<A_{n,r}> \cdot <A_{n,s}> \cdot \underbrace{< \cos(\varphi_{n,s}) >}_{=0}} \tag{65}$$

Using equation 58 the coefficients of the power spectra

$$< S_n >=< S_{n,r} > + < S_{n,s} > \tag{66}$$

and the ms values

$$< \overline{\Phi'^2} >=< \overline{\Phi_r'^2} > + < \overline{\Phi_s'^2} > \tag{67}$$

can easily be derived.

D.5 Some remarks on data obtained from measurements

From a measurement $\Phi(t)$ is not obtained as a continous function. In a time period τ, discrete values Φ^t are acquired at an acquisition frequency f_{aq}, where the index t runs from $t = 1$ to the number of acquired points $t = N$ calculated from $N = f_{aq} \cdot \tau$. Statistical properties as they are defined in the above sections have therefore to be calculated using reasonable assumptions. For example, the mean value of $\Phi(t)$ (equation 49) is approximated by

$$\overline{\Phi} = \frac{1}{N} \sum_{t=1}^{N} \Phi^t. \tag{68}$$

A Fourier series (see equation 57) calculated from a discrete time series is limited to a finite number of Fourier coefficients A_n, where the index n runs from 1 to $N/2$. In such a discrete Fourier series only contributions between the lowest frequency $f_{\min} = 1/\tau$ and the highest frequency $f_{\max} = f_{aq}/2$ occur. Thus the power spectra defined from equation 58 is not a continuous function but a series of limited elements. In the discussion this point is sometimes neglected but when all relevant frequencies of a signal have been covered in the measurement by a long enough acquisition time and a high enough acquisition frequency the discrete functions are well represented by the series.

E Performed experiments

In the tables below the essential physical parameters and non-dimensional numbers of the experiments are summarized. P is the elctrical power supplied to the test section, H indicates the used power supply (k: controlled, g: non-controlled), B is the magnitude of the applied magnetic field, q the resulting heat flux after taking into account heat losses (see section 3.2), ΔT the measured temperature difference across the layer, T_m the mean temperature of the fluid, Q the Chandrasekhar number, Ra the Rayleigh number, $Ra_r = Ra - Ra_c$ the reduced Rayleigh number, Pr the Prandtl number and Nu the Nusselt number. The critical Rayleigh number Ra_c is calculated from equation 69 based on the linear theory of Chandrasekhar (1961).

E.1 Test matrix $M1$, short time series

E.1.1 Ordinary hydrodynamic flow ($Q = 0$):

$Ra_c \approx 1708$

P	H	B	q	ΔT	T_m	Q	Ra	Ra_r	Pr	Nu
$[W]$		$[T]$	$[W/m^2]$	$[°C]$	$[°C]$					
169.7	k	0	1.26E+03	0.97	101.60	0	1295	-413	0.021	1.12
199.6	k	0	1.62E+03	1.33	101.59	0	1766	58	0.021	1.05
244.3	k	0	2.16E+03	1.75	102.23	0	2330	622	0.021	1.06
311.4	k	0	2.97E+03	2.34	101.81	0	3116	1408	0.021	1.09
496.5	k	0	5.17E+03	3.61	103.30	0	4833	3125	0.021	1.23
754.1	k	0	8.24E+03	5.28	104.49	0	7077	5369	0.021	1.34
1014.5	k	0	1.13E+04	7.01	106.78	0	9463	7755	0.021	1.38
1202.6	k	0	1.36E+04	8.04	107.23	0	10867	9159	0.021	1.45
1808.9	k	0	2.09E+04	11.28	108.85	0	15300	13592	0.020	1.58
2419.4	k	0	2.82E+04	14.45	110.24	0	19677	17970	0.020	1.67
2275.9	g	0	2.65E+04	13.73	112.19	0	18789	17081	0.020	1.65
3526.8	g	0	4.16E+04	19.77	115.38	0	27273	25565	0.020	1.79
5178.7	g	0	6.15E+04	26.80	120.24	0	37452	35744	0.019	1.95
6929.8	g	0	8.26E+04	33.67	125.22	0	47655	45947	0.019	2.08
8746.2	g	0	1.05E+05	40.34	130.19	0	57836	56129	0.018	2.19
10430.0	g	0	1.25E+05	45.97	134.46	0	66641	64933	0.018	2.28

E.1.2 MHD flow at $Q \approx 100$:

$Ra_c = 3768$

P	H	B	q	ΔT	T_m	Q	Ra	Ra_r	Pr	Nu
$[W]$		$[T]$	$[W/m^2]$	$[°C]$	$[°C]$					
310.7	k	7.15E-03	2.95E+03	2.56	101.69	95	3415	-353	0.021	0.99
501.3	k	7.25E-03	5.21E+03	4.44	102.89	98	5937	2168	0.021	1.01
753.5	k	7.21E-03	8.19E+03	6.43	105.05	98	8635	4866	0.021	1.09
1200.0	k	7.28E-03	1.35E+04	9.71	107.84	100	13138	9370	0.021	1.19
1800.5	k	7.31E-03	2.07E+04	13.55	109.87	102	18439	14670	0.020	1.31
2419.5	k	7.32E-03	2.82E+04	17.22	111.64	102	23531	19763	0.020	1.40
2330.4	g	7.37E-03	2.71E+04	17.00	113.63	104	23356	19587	0.020	1.36
3483.5	g	7.35E-03	4.09E+04	23.42	117.32	105	32476	28707	0.020	1.49
5255.0	g	7.17E-03	6.22E+04	32.33	123.36	101	45548	41779	0.019	1.63
6931.5	g	7.15E-03	8.24E+04	40.14	128.74	102	57331	53562	0.018	1.73
8672.3	g	7.12E-03	1.03E+05	47.72	134.17	102	69123	65355	0.018	1.82
10565.6	g	7.15E-03	1.26E+05	55.11	139.47	105	80924	77155	0.018	1.92

E.1.3 MHD flow at $Q \approx 400$:

$Ra_c \approx 8655$

P	H	B	q	ΔT	T_m	Q	Ra	Ra_r	Pr	Nu
$[W]$		$[T]$	$[W/m^2]$	$[°C]$	$[°C]$					
501.4	k	1.44E-02	5.19E+03	4.53	103.79	389	6063	-2592	0.021	0.98
750.5	k	1.45E-02	8.13E+03	6.98	106.06	395	9407	752	0.021	1.00
1202.3	k	1.45E-02	1.35E+04	11.09	110.05	402	15089	6434	0.020	1.04
1801.7	k	1.45E-02	2.07E+04	15.76	112.00	404	21552	12898	0.020	1.12
2422.8	k	1.45E-02	2.81E+04	19.98	113.41	404	27435	18780	0.020	1.20
2421.1	g	1.44E-02	2.81E+04	20.25	115.61	401	27960	19305	0.020	1.18
3482.2	g	1.46E-02	4.08E+04	26.80	119.32	417	37353	28699	0.019	1.29
5209.3	g	1.45E-02	6.16E+04	35.46	124.33	413	50078	41423	0.019	1.47
6973.4	g	1.42E-02	8.28E+04	43.83	130.53	401	62895	54240	0.018	1.59
8735.7	g	1.42E-02	1.04E+05	51.69	136.55	407	75335	66680	0.018	1.69
10438.7	g	1.42E-02	1.25E+05	58.84	141.64	415	86873	78218	0.017	1.77

E.1.4 MHD flow at $Q \approx 784$:

$Ra_c \approx 14135$

P	H	B	q	ΔT	T_m	Q	Ra	Ra_r	Pr	Nu
$[W]$		$[T]$	$[W/m^2]$	$[°C]$	$[°C]$					
749.7	k	2.04E-02	8.11E+03	6.94	105.26	784	9335	-4800	0.021	1.00
1202.1	k	2.01E-02	1.35E+04	11.77	110.32	773	16027	1892	0.020	0.98
1804.6	k	2.01E-02	2.07E+04	17.08	112.51	778	23394	9260	0.020	1.03
2420.8	k	2.02E-02	2.81E+04	21.93	114.92	787	30220	16085	0.020	1.09
2414.6	g	2.02E-02	2.80E+04	21.93	116.68	787	30356	16222	0.020	1.08
3486.5	g	2.00E-02	4.08E+04	29.49	121.02	786	41292	27158	0.019	1.17
5206.1	g	2.00E-02	6.14E+04	39.28	127.41	797	55913	41779	0.019	1.32
6935.7	g	2.00E-02	8.23E+04	48.21	133.59	805	69734	55600	0.018	1.44
8746.4	g	2.00E-02	1.04E+05	56.30	139.25	820	82622	68488	0.018	1.55

E.1.5 MHD flow at $Q \approx 1600$:

$Ra_c \approx 24942$

P	H	B	q	ΔT	T_m	Q	Ra	Ra_r	Pr	Nu
$[W]$		$[T]$	$[W/m^2]$	$[°C]$	$[°C]$					
1202.7	k	2.86E-02	1.35E+04	11.80	110.93	1557	16090	-8852	0.020	0.98
1801.1	k	2.86E-02	2.06E+04	17.84	113.85	1572	24522	-420	0.020	0.98
2419.2	k	2.87E-02	2.80E+04	23.63	116.78	1593	32724	7782	0.020	1.01
2341.5	g	2.89E-02	2.70E+04	23.54	118.04	1617	32700	7758	0.020	0.97
3523.0	g	2.85E-02	4.11E+04	32.84	123.26	1598	46250	21308	0.019	1.06
5208.1	g	2.85E-02	6.13E+04	43.95	130.14	1624	63009	38067	0.018	1.18
6915.2	g	2.84E-02	8.19E+04	53.47	136.44	1643	77905	52963	0.018	1.29
8738.9	g	2.84E-02	1.04E+05	62.36	142.50	1658	92280	67338	0.017	1.39

E.1.6 MHD flow at $Q \approx 14400$:

$Ra_c \approx 174042$

$P[W]$	H	$B[T]$	q	ΔT	T_m	Q	Ra	Ra_r	Pr	Nu
$[W]$		$[T]$	$[W/m^2]$	$[°C]$	$[°C]$					
1804.2	k	8.66E-02	2.06E+04	18.26	113.95	14431	25096	-148946	0.020	0.96
2420.6	k	8.67E-02	2.80E+04	24.52	117.13	14561	33988	-140054	0.020	0.97
2400.2	g	8.75E-02	2.77E+04	24.90	118.96	14900	34683	-139359	0.019	0.94
3516.5	g	8.74E-02	4.10E+04	36.10	124.83	15086	51052	-122990	0.019	0.96
5203.3	g	8.74E-02	6.11E+04	51.63	134.02	15415	74754	-99288	0.018	1.00
6910.6	g	8.73E-02	8.14E+04	66.20	142.89	15713	98063	-75979	0.017	1.03

E.2 Test matrix $M2a$, long time series with $Ra \approx 5 \cdot 10^4$

$\tau = 32768\ s$, $f_{aq} = 128\ Hz$, $N = 4194304$ (for probe only)

P	H	B	q	ΔT	T_m	Q	Ra	Ra_r	Pr	Nu
$[W]$		$[T]$	$[W/m^2]$	$[°C]$						
7073.2	g	0	8.43E+04	34.53	126.76	0	49072	47364	0.019	2.06
4921.7	g	1.47E-02	5.81E+04	34.93	125.10	424	49426	47718	0.019	1.41
3751.0	g	2.87E-02	4.39E+04	34.80	124.14	1624	49117	47409	0.019	1.07
3532.1	g	4.34E-02	4.12E+04	35.42	124.01	3714	49979	48271	0.019	0.99
3521.5	g	8.52E-02	4.10E+04	36.05	124.04	14313	50867	49159	0.019	0.96

E.3 Test matrix $M2b$, long time series with $P = 2400W$

$\tau = 32768\ s$, $f_{aq} = 128\ Hz$, $N = 4194304$ (for probe only)

P	H	B	q	ΔT	T_m	Q	Ra	Ra_r	Pr	Nu
$[W]$		$[T]$	$[W/m^2]$	$[°C]$	$[°C]$					
2423.8	k	0	2.83E+04	14.39	112.61	0	19707	17999	0.020	1.68
2419.8	k	1.49E-02	2.81E+04	19.83	115.66	427	27382	25674	0.020	1.20
2422.9	k	2.04E-02	2.80E+04	21.59	116.61	807	29890	28182	0.020	1.11
2389.0	k	2.90E-02	2.76E+04	23.41	117.49	1627	32474	30766	0.020	1.00
2407.0	k	4.35E-02	2.78E+04	23.89	117.64	3666	33153	31445	0.020	0.99
2408.5	k	8.50E-02	2.78E+04	24.40	116.97	13982	33802	32094	0.020	0.97

F Critical Rayleigh-numbers

The critical Rayleigh number for the onset of convection for an arbitrary Chandrasekhar number is obtained with suitable accuracy from a polynominal fit of the values determined from Chandrasekhar (1961). In figure 40 the values are plotted together with the fit given by equation 69.

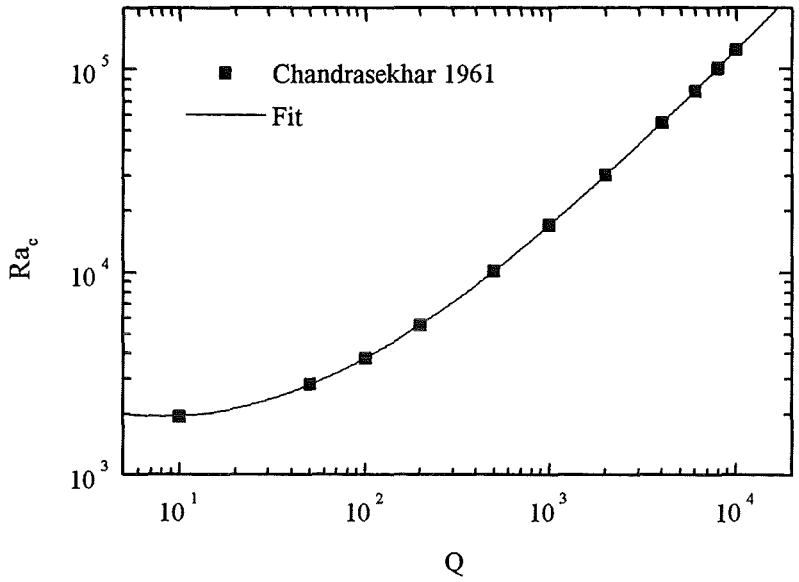

Figure 40: Critical Rayleigh numbers Ra_c obtained from linear stability analysis (Chandrasekhar (1961)). A fitting curve is evaluated from the analytical values (dots) in order to obtain Ra_c at any Chandrasekhar number.

$$\log(Ra_{crit}) = 3,53603 - 0,56638\log(Q) + 0,34739\log^2(Q) - 0,02708\log^3(Q) \qquad (69)$$

G Symbols

Skalar Properties:

a_c	horizontal wave number
A	base area of the liquid metal layer
A_n	Fourier coefficients
$A_k(t)$	autocorrelation function
A_{SS}	cross-section area of side walls
A_{xz}	horizontal isotropy coefficients
A_{yx}, A_{yz}	vertical isotropy coefficients
B_0	magnitude of magnetic induction
C_b	coefficient of heat losses to the environment
C_b	coefficient of heat losses in the wiring of the heater rods
c_p	specific heat capacity
e	distance of thermocouples from fluid-wall interface
$E(f_n)$	integrated power spectra
f	frequency
f_n	discrete frequency n
$f_0 = \kappa/h^2$	characteristic frequency
f_{aq}	aquisition frequency
G	gain of amplifiers
g	magnitude of acceleration of gravity ($g = 9.81m/s^2$)
h	hight of the liquid metal layer
K	correlation coefficient
p	pressure
p^*	non-dimensional pressure
P	Power
P_s	heat losses in the side walls
P_b	heat losses to the environement
P_{el}	heat losses in the wiring of the heater rods
P_{lm}	amount of heat per time passing the liquid metal layer
Q	correlation
q	magnitude of heat flux
q_0	heat flux equivalent to pure heat conduction
q_{co}	convective heat flux
S	power spectra
S	discrete element of power spectra n
S_T	power spectra of temperature fluctuations
S_v	power spectra of velocity fluctuations
s	root-mean-square (rms-) value
s^2	mean-square (ms-) value

t	time; discrete time step when used as upper index
$t_0 = v_0/a$	characteristic time
T	temperature
T_b	temperature of the bottom plate
T_m	mean temperature of the fluid
T_t	temperature of the top plate
T_e	temperature of the environment
ΔT	temperature difference across the layer
$T_{i,,j}$	temperatures in the copper plates
	index $i = M$ (central) or N, S, O, W (four winds)
	index $j = b$ (bottom plate) or t (top plate)
T_{1-4}	temperatures of the probe elements
U	voltage
U_T	thermo-voltage
u	velocity in x-direction
v	velocity in y-direction
w	velocity in z-direction
$v_0 = \kappa/h$	characteristic velocity
x, y, z	cartesian coordinate system
x_i, y_i, z_i	position of probe thermocouple T_i
β	cubic thermal expansion coefficient
Γ	signal to noise ratio
Γ_n	signal to noise ratio at discrete frequency
δU	resolution of voltage
δT	resolution of temperature
κ	thermal diffusivity
λ	thermal conductivity
λ_{Cu}	thermal conductivity of copper
λ_{SS}	thermal conductivity of stainless steel
λ_c	critical wavelength
μ	magnetic permeability
ν	kinematic viscosity
ρ	density
σ	electrical conductivity
τ	time period
τ_I	integral time-scale
Φ	arbitrary Variable
ω_n	discrete angular velocity n

Vectors (bold):

$\mathbf{B} = (b_x, b_y, b_z)$	magnetic field
$\mathbf{E} = (e_x, e_y, e_z)$	electric field
$\mathbf{F}_L$	Lorentz force
$\mathbf{e}_x, \mathbf{e}_y, \mathbf{e}_z$	unit vectors in spacial directions x, y and z
$\mathbf{g}$	acceleration of gravity
$\mathbf{j} = (j_x, j_y, j_z)$	current density
$\mathbf{q} = (q_x, q_y, q_z)$	heat flux
$\mathbf{v} = (u, v, w)$	velocity

Characteristic numbers:

M	Hartmann-Number
Nu	Nusselt number
Pr	Prandtl number
Q	Chandrasekhar number
Ra	Rayleigh number
Ra_c	critical Rayleigh number (for onset of convection)
Ra_r	reduced Rayleigh number ($Ra_r = Ra - Ra_c$)
Ra_m	modified Rayleigh number ($Ra_m = Ra/Ra_c - 1$)
Ra_t	critical Rayleigh number (for onset of time dependent convection)
Re	Reynolds number
Pm	magnetic Prandtl number

Mathematical notation:

∇	gradient
$\nabla\cdot$	divergence
Δ	laplacian
$\nabla\times$	curl
$\frac{\partial}{\partial x_i}\Phi = \partial_{x_i}\Phi$	partial derivative of Φ in x_i-direction
$\overline{\Phi}$	temporal mean value of Φ
Φ'	fluctuatin part of Φ
$< \Phi >_M$	average over M samples